Interactions of Plasmonic Nanoparticles with Photosynthetic Complexes

Dissertation

der Mathematisch-Naturwissenschaftlichen Fakultät

der Eberhard Karls Universität Tübingen

zur Erlangung des Grades eines

Doktors der Naturwissenschaften

(Dr. rer. nat.)

vorgelegt von

M.Sc. Imran Ashraf

aus Gujrat, Pakistan

Tübingen

2017

Gedruckt mit Genehmigung der Mathematisch-Naturwissenschaftlichen Fakultät der Eberhard Karls Universität Tübingen.

Tag der mündlichen Qualifikation:	28.08.2017
Dekan:	Prof. Dr. Wolfgang Rosenstiel
1. Berichterstatter:	Prof. Dr. Marc Brecht
2. Berichterstatter:	Prof. Dr. Alfred J. Meixner

Abstract

Tailored metallic nanoparticles (NPs) coupled to specific proteins (bio-nanohybrids) can provide tunable functional materials at the nanoscale. Malleable characteristics of the NPs and diversity of the protein functions widen the horizons of conceivable applications of such bio-nanohybrids. In the presented work the interplay between Photosystem I (PSI) from Thermosynechococcus elongatus (*T. elongatus*) and different plasmonic NPs was investigated. PSI, an abundant photoactive pigment-protein complex is the essential component of photosynthesis. It binds $\sim$ 300 chlorophyll molecules (Chl *a*) per trimer within its protein scaffolding to facilitate the conversion of solar energy into chemical energy.

PSI complexes were coupled to different mono- and bimetallic NPs and corresponding plasmonic interaction effects on the fluorescence properties of the PSI were investigated using single-molecule spectroscopy (SMS). The used metallic NPs were fabricated by thermal annealing of thin metallic films. Measurements were performed at different temperatures in a range 1.6 - 250 K and variations in the emission properties of isolated and NP-coupled PSI complexes were analyzed comprehensively.

Interactions with bimetallic NPs exhibiting various metallic compositions were studied at cryogenic temperature (1.6 K). The fluorescence emission of the PSI was intensified upon coupling with NPs. Different compositions of the bimetallic NPs resulted in different enhancement factors (EFs). NPs with Au/Au composition led the maximum enhancement followed by the Ag/Au and Au/Ag. On average the fluorescence was enhanced up to 4.4 (Au/Au), 2.3 (Ag/Au), and 1.1 (Au/Ag)-fold. For individual complexes, however, EFs even up to 22.9 (Au/Au), 5.1 (Ag/Au), and 1.7 (Au/Ag)-fold were observed.

The enhancement of the fluorescence demonstrated strong wavelength dependence for all compositions. This was explained considering the largely extended multichromophoric composition of PSI.

To further study the impact of temperature on metal-enhanced fluorescence (MEF) of PSI, monometallic NPs composed of gold only were employed. Measurements were performed at 1.6, 90, 190 and 250 K. A strong temperature dependence of the shape and intensity of the emission spectra was noticed. On average the fluorescence was enhanced 4.3 (1.6 K), 19.4 (90 K), 57.6 (190 K) and 84.0 (250 K)-fold. However, for individual complexes, the EFs up to 230, 250 and even 441-fold were observed. The remarkable increase in EFs at higher temperatures was discussed taking into account the low initial fluorescence yield of PSI, an increase in excitation rate, appearance of new emission channels due to altered excitation energy transfer (EET) pathways and increased spectral overlap between absorption spectrum of gold nanoparticles (AuNPs) and emission spectrum of PSI.

In the last part, photopatterned self-assembled monolayers (SAMs) of the thiols were applied to achieve a precise and controlled attachment of the proteins to the gold substrate. Two thiols, i.e., perfluorinated and carboxylic acid-terminated were applied to prevent the unwanted and encourage the wanted adsorption, respectively. Different surface analysis techniques were used to examine the formation and photopatterning of the SAMs. It was noticed that to ensure the complete photooxidation of the perfluorinated thiol, it is essential to use a specific wavelength of UV light. Perfluorinated thiol did not prove a strong resister against unwanted attachment, as an adequate amount of the PSI was found at nonspecific sites. Carboxylic acid-terminated thiol, however, fulfilled the objective and appeared as a suitable candidate to encourage the desired attachment of the PSI.

Zusammenfassung

Maßgeschneiderte, metallische Nanopartikel (NPs), die an spezielle Proteine gebunden werden (Bio-Nanohybride), stellen durchstimmbare Funktionsmaterialien auf Nanoebene dar. Die anpassbaren Eigenschaften der Nanostrukturen und die Vielfalt der Proteinfunktionen eröffnen für solche Bio-Nanohybride einen breiten Horizont möglicher Anwendungen. In der vorliegenden Arbeit wurde die Wechselwirkung zwischen Photosystem I (PSI) aus Thermosynechococcus elongatus (*T. elongatus*) und plasmonischen Nanopartikeln untersucht. PSI, ist ein photoaktiver essentieller Proteinkomplex der Photosynthese. Dieser bindet ∼300 Chlorophyll-Moleküle (Chl *a*) pro trimer innerhalb des Proteingerüsts, um die Umwandlung von Sonnenenergie in chemische Energie zu ermöglichen.

Unterschiedliche mono- und bimetallische NPs wurden mit PSI-Komplexen gekoppelt und die entsprechenden plasmonischen Wechselwirkungseffekte auf die Fluoreszenzeigenschaften von PSI mittels Einzelmolekülspektroskopie (Single Molecule Spectroscopy: SMS) untersucht. Die verwendeten NPs wurden durch Tempern dünner Metallfilme hergestellt. Die Messungen wurden bei verschiedenen Temperaturen zwischen 1,6 - 250 K durchgeführt und Veränderungen in den Emissionseigenschaften von isolierten und Metall NP-gekoppelten PSI-Komplexen umfassend analysiert.

Wechselwirkungen mit bimetallischen NPs unterschiedlichster Zusammensetzung, wurden unter kryogenen Temperaturen (1,6 K) durchgeführt. Die Fluoreszenzemission von PSI wurde durch die Kopplung verstärkt. Verschiedene Zusammensetzungen der bimetallischen NP resultierten in unterschiedlichen Verstärkungsfaktoren der Emission. NP mit Au/Au Zusammensetzung führten zu maximaler Verstärkung, gefolgt von Ag/Au und

Au/Ag. Im Durchschnitt wurde die Fluoreszenz um das bis zu 4,4-fache bei Au/Au verstärkt, 2,3-fach bei Ag/Ag und 1,1-fach bei Au/Ag. Für einzelne Komplexe wurde jedoch eine bis zu 22,9-fache Emissionsverstärkung bei Au/Au beobachtet, 5,1-fach bei Ag/Au und 1,7-fach bei Au /Ag. Die Verstärkung der Fluoreszenz zeigte für alle Zusammensetzungen eine starke Wellenlängenabhängigkeit. Diese wurde auf die große räumliche Ausdehnung der Multichromophore in PSI zurückgeführt in kombination mit der unspezifischen Anbindung an die NPs.

Um den Einfluss der Temperatur auf die durch Metall verstärkte Fluoreszenz (Metal-Enhanced Fluorescence: MEF) von PSI weitergehend zu untersuchen, wurden nur aus monometallische NP verwendet. Die Messungen wurden bei 1,6, 90, 190 und 250 K durchgeführt, wobei eine starke Temperaturabhängigkeit in Bezug auf Form und Intensität der Emissionsspektren festgestellt wurde. Im Durchschnitt wurde die Emission um das 4,3 (1,6 K)-, 19,4 (90 K)-, 57,6 (190 K)- und 84,0 (250 K)-fache verstärkt. Allerdings wurde für einzelne Komplexe ein Emissionsverstärkung bis zum 230-, 250- und sogar bis zum 441-fachen beobachtet. Die bemerkenswerte Erhöhung der Verstärkungsfaktoren bei höheren Temperaturen kommte unter Beachtung der anfänglich niedrigen Fluoreszenzausbeute von PSI, einer Zunahme der Anregungsrate, dem Auftreten neuer Emissionskanäle durch geänderte Anregungsenergietransferwege und durch stärkere spektrale Überlappung zwischen dem Absorptionsspektrum der Au-Nanopartikel und dem Emissionsspektrum von PSI durch ein Modell erklärt werden.

Im letzten Teil dieser Arbeit wurden photostrukturierte, selbst anordnende Monolagen (Self-Assembled Monolayer; SAMs) verschiedener Thiole verwendet, um eine präzise und kontrollierte Anbindung der Proteine an das Goldsubstrat zu gewährleisten. Zwei Thiole, perfluorierte und carboxylsäureterminierte wurden untersucht, um die unerwünschte Adsorption zu verhindern und die gewünschte zu unterstützen. Unterschiedliche Oberflächenanalysetechniken wurden eingesetzt, um die Bildung der SAMs und die Photostrukturierung der Monolagen zu untersuchen. Darüber hinaus wurde herausgefunden, dass um eine komplette Photooxidation der perfluoierte Thiol

sicherzustellen, eine spezifische Wellenlänge von UV-Lichts benötigt wird. Das Perfluorierte Thiol stellte sich nicht als guter Hemmer für unerwünschte Anbindungen heraus, da eine bestimmte Menge von PSI an den nanospezifischen Stellen nachgewiesen wurde. Das Carboxylsäure-terminiertes Thiol hingegen, erfüllte die Anforderungen und stellte sich als passender Kandidat heraus, die gewünschten Anbindungen von PSI zu erreichen.

Acknowledgements

I would like to express my sincere gratitude to my advisor Prof. Dr. Marc Brecht for his continuous support, encouragement, motivation, and for providing a great environment during my Ph.D. I could not have imagined having a more friendly and kindhearted advisor for my Ph.D. study. I also owe my deepest gratitude to Prof. Dr. Alfred J. Meixner for always being so kind, supportive and encouraging. You people are not only great scientists, but also great human beings. It was an honour to work under the supervision of you both.

I would also like to thank, Kerstin Scherzinger and Regina Jäger for their precious time to translate the abstract of the thesis into the German language. I am very grateful to Andreas Horrer (Prof. Monika Fleischers group, University of Tübingen), Mathias Glaser (Prof. Thomas Chassé group, University of Tübingen) and Dr. York-Dieter Stierhof (ZMBP, University of Tübingen) for assistance with SEM, XPS and fluorescence microscopy techniques, respectively. My sincere thanks also go to my colleagues for all the support and making my time such a great experience on both professional and personal level.

Specially, I would like to thank my family. This work would not have been possible without the continued moral support from my parents, wife, brother and sister. And foremost my cute son, M. Ibrahim Imran, who always was a reason to smile whenever I was down.

Contents

List of Figures

List of Tables

List of Abbreviations

AuNP	Gold Nanoparticle
AgNP	Silver Nanoparticle
BS	Beam Splitter
Chl *a*	Chlorophyll *a*
CLSM	Confocal Laser Scanning Microscopy
CW	Continuous Wave
EET	Excitation Energy Transfer
EF	Enhancement Factor
ETC	Electron Transport Chain
FCS	Fluorescence Correlation Spectroscopy
F_d	Ferredoxin
GFP	Green Fluorescent Protein
He-Ion	Helium Ion
HIM	Helium Ion Microscopy
LHe	Liquid Helium
LHC	Light Harvesting Complex
LSPR	Localised Surface Plasmon Resonance
LN_2	Liquid Nitrogen
MNP	Metallic Nanoparticle
MO	Microscope Objective
NA	Numerical Aperture
NP	Nanoparticle
NSL	Nanosphere Lithography

PC	Plastocyanin
PMT	Photomultiplier
PQ	Plastoquinone
PS	Polystyrene
PSI	Photosystem I
PSII	Photosystem II
QD	Quantum Dot
QY	Quantum Yield
RC	Reaction Centre
SAM	Self-Assembled Monolayer
SBR	Signal to Background Ratio
SE	Secondary Electron
SEM	Scanning Electron Microscopy
SEI	Secondary Electron Imageing
SMS	Single-Molecule Spectroscopy
SNR	Signal to Noise Ratio
SPR	Surface Plasmon Resonance
T. elongatus	Thermosynechococcus elongatus
WDE	Wavelength Dependent Enhancement
XPS	X-ray Photoelectron Spectroscopy

Dedicated to my family...

1 Introduction

1.1 Background

Nature has always been a marvellous source of inspiration for the scientific world. Imitation of the natural processes stimulated many inventions [1–6]. Photosynthesis, in this regard, is particularly of great interest and one of the largely mimicked natural processes. The conversion of solar into chemical energy by photosynthetic organisms underpins virtually all forms of life on earth. A precise and well-defined organization of the chlorophylls (Chl a) as an antenna in the photosynthetic apparatus allows an efficient capture and transfer of solar energy to the reaction centre (RC) where light-induced charge separation occurs. Since the discovery of photosynthesis in 1727 [7], decoding the molecular mechanism(s), which efficiently converts the light energy into chemical energy, has been a hot topic in the scientific community. Studies of the molecular mechanisms led the scientists to invent multiple

inventions utilizing the light-triggered processes [8–17].

The process of photosynthesis is mainly driven by the cooperation of two photosystems termed as, Photosystem I (PSI) and Photosystem II (PSII), located in the thylakoid membrane. They utilize the photo energy to translocate electrons across the membrane and create a transmembrane difference in the concentration of H^+ and electrical potential leading to the synthesis of ATP and reduction of $NADP^+$ to NADPH [18]. The general idea of two photosystems was for the first time briefly interpreted by Rabinowitch [19, 20] in 1956, but it was vastly overlooked without any peculiar recognition. In 1957 -1958, the concept of two light reactions was in air when Emerson *et al.,* observed an enhancement in rate of the photosynthesis if two beams of red and far-red light were given simultaneously compared to the sum of the rates for individual beams alone [21, 22]. This enhancement was later recognized as an Emerson enhancement effect (EEE) and proved a forebear of the concept of two photosystems involvement in photosynthesis. In 1960, Hill *et al.*, and Bendall *et al.*, proposed a detailed, explicit, and testable theoretical "Z-scheme" model of the two photosynthetic light reactions functioning in series [23]. This model was lacking any experimental support, which later in 1961 was provided by the experiments of Duysens *et al.,* and Witt *et al.,* [24–26]. They for the first time proved the existence of the two photosystems with the clear experimental shreds of evidence.

In the following decades, a race initiated in the scientific community to physically separate the two photosystems and to unravel their structures [27–35]. This markedly impacted the research of the oxygenic photosynthesis. The structural information at atomic detail determined by X-ray crystallography provided a comprehensive picture of the interactions between various cofactors, their organization, the role of the protein subunits and individual amino acids in binding these cofactors [18, 36]. This detail offered a basis to understand how photosystems efficiently capture light and transfer an electron.

Establishment of the procedures for efficient and reproducible isolation of the photosystems and profound insight into their functional principles opened

the doors for integration of photosystems into semi-artificial systems. The comprehensive understanding of the PSI at molecular level, its high quantum yield (QY), nanoscale dimensions and ability to generate large voltage offered an excellent blueprint for its usage in biosensors, semi-artificial energy converting, bioelectrochemical, and optoelectronics devices [13, 15, 37–46]. The low absorption of PSI, however, hinders the range of its applications [47]. A rapid progress in nanotechnology helped the utilization of metallic nanoparticles (NPs) as light concentrator and optical antenna in nano-biosensing, thin film optoelectronics, and solar devices [48–52]. Their ability to localize light at nanoscale creates the opportunity to enhance the absorption of thin absorber layers and design the efficient light-absorbing devices. The modifications in the optical properties of fluorophores due to metallic NPs in close vicinity has a long scientific history starting from 1966 when Drexhage *et al.,* first time experimentally demonstrated that the molecules in close proximity to metal surfaces may exhibit different optical properties compared to an isolated molecules [53]. Soon after, in 1974, amplification in the Raman signals established that metallic surfaces can enhance the optical properties of molecules [54], and thus the term surface-enhanced Raman scattering (SERS) was coined [55–57]. During this era, a plethora of literature was published describing the enhancement in molecular fluorescence [58–63], which later was termed as a metal-enhanced fluorescence (MEF) [64]. Both, SERS and MEF phenomena are analogous, but occur under different experimental conditions. In order to achieve optimal SERS signals, the fluorophores are adsorbed to the metal surface [65, 66]. Contrary to that, for MEF, a certain distance between fluorophores and metallic NPs is maintained to avoid the quenching effects due to the direct contact ($d < 5$ nm) with metal [67]. The increased fluorescence intensity of the fluorophores and improved photostability in the vicinity to metallic NPs attracted a huge interest in diverse research fields like nano-biosensing, biotechnology, optical spectroscopy and nanophotonics [49, 50, 68–74]. Studying PSI together with the metallic NPs and understanding the basic processes involved in altering its optical properties can assist to optimize the efficiency of PSI based devices and widen

the horizon for its conceivable applications in molecular optoelectronics and biotechnology.

Although, high-resolution crystal structures have given a profound insight into the proteins, cofactors, and their mutual interactions, but the basic understanding of the energy transfer process and optical properties of PSI still remains unexplained. Since the crystal structures deliver a static image only, while proteins are known to be dynamic systems and are characterized as "screaming and kicking" [75, 76]. They can fluctuate among many states on selected energy landscapes and so are their functions [77]. Thus, high-resolution crystal structures are not enough to monitor the motility and structural changes of the proteins in real time and fully understand their optical properties. Single-molecule spectroscopy (SMS) offers a unique tool to study the dynamical behaviour of molecules. It offers the opportunity to unravel the information hidden in spectra of large ensembles. Further, at cryogenic temperatures large-scale motions of proteins are frozen out, as a result, the temporal averaging over many states of the individual protein is decreased. It is noteworthy that proteins can show dynamic variations even at cryogenic temperatures. In SMS these changes are observed in the form of spectral jumps, which commonly are termed as spectral diffusions [78]. At single molecule level, spectral diffusions allow the observation of even the smallest changes in the environment of the proteins, which makes SMS an excellent tool to investigate the energy transfers in PSI [79]. Therefore, during this Ph.D. project, SMS was used to study the effects of metallic NPs on the optical properties of the PSI at different temperatures. To this aim, different types of mono- and bimetallic NPs were fabricated and characterized by using different techniques. A series of experiments were performed to investigate their interactions with photosynthetic complexes at various temperatures.

1.2 Thesis Structure

The whole thesis consists of seven chapters in total.

- Chapter 1 introduces the background and presents a brief history of the discovery of photosynthesis, the two photosystems, and MEF. Additionally, the significance of conducting this project is outlined.

- Chapter 2 focuses on the theoretical background of all the topics involved. A detailed description of the photosynthesis, PSI, plasmonic interactions, energy transfer mechanisms, MEF, and SMS is presented.

- Chapter 3 reviews the material and methods. All the experimental techniques used during the study are introduced in this section. A detailed explanation of the experimental setup used for SMS at cryogenic temperatures, fabrication of mono- and bimetallic NPs, instruments employed for characterization of substrates and surfaces, and preparation of the samples is given.

- In Chapter 4 the effects of bimetallic NPs on optical properties of PSI at cryogenic temperature are reported. Explanation of the fabrication of bimetallic NPs is given. NPs fabricated with various metallic compositions under different fabrication conditions were coupled to PSI, and SMS was performed at cryogenic temperatures. The resulting effects on optical properties of PSI are discussed.

- Chapter 5 focuses on the temperature dependence of the MEF of PSI. Monometallic NPs fabricated by thermal annealing were employed for investigations at various temperatures. A strong temperature dependence of the intensity and shape of the emission spectra is reported. The plausible mechanism responsible for the temperature dependence of the enhancement factor (EF) is discussed.

- Chapter 6 focuses on site-specific immobilization of PSI. Self-assembled monolayer (SAM) approach was adopted to bind proteins (green fluorescent protein (GFP) and PSI) at specific sites on gold substrates.

Various surface analysis techniques were used to characterize the surfaces and verify the binding of proteins at specific sites. Corresponding results are discussed.

- Chapter 7 summarises all the main accomplishments of the Ph.D. work.

2

Theoretical Background

In the following chapter a brief introduction of photosynthesis, general architecture of PSI, major cofactors involve in energy transfer and charge separation is presented. In the later part, an overview of the plasmonic interactions, mechanisms responsible for fluorescence enhancement and SMS is given. A more detailed discussion can be found in the cited references.

2.1 Photosynthesis

Sunlight reaching the earth's surface serves as a primary source of energy for life on our planet. Conversion of the solar energy into the chemical energy through photosynthesis has established the life on earth [80]. The history of the evolution of photosynthesis goes side by side with the evolution of life on Earth [81]. It is believed that the earliest form of photosynthesis was anoxygenic photosynthesis followed by its transition to oxygenic photosynthesis some 2.5 billion years ago [80]. In oxygenic photosynthesis, a light-driven chemical reaction uses water and CO_2 to produce sugar with oxygen as a by-product. The overall process of oxygenic photosynthesis can be summarized by following chemical equation;

$$12H_2O + 6CO_2 \xrightarrow{\text{Light}} C_6H_{12}O_2 + 6H_2O + 6O_2$$

The photosynthesis in photosynthetic organisms, e.g., algae, plants, and cyanobacteria take place in the specialized thylakoids membrane. In plants and algae, the thylakoids are housed as a cylindrical stacks of discs in the cell organelles called chloroplasts. However, cyanobacteria unlike plants and eukaryotic algae, lack the chloroplast and the thylakoids are found in the cytoplasm in a uniform sheetlike structures [82]. The membrane of these thylakoids is the place where photosynthesis takes place. A schematic representation of thylakoid membrane composed of electron transport complexes, pigments and ATP synthase, etc., is shown in Fig. 2.1. Photosynthesis is divided into two parts (i) light reactions: which needs light to produce organic energy molecules and (ii) dark reactions: which are independent of light and use organic energy molecules to synthesise sugar from CO_2. The dark reactions take place in stroma while the light reactions occur in the thylakoid membrane. To perform a light reaction, the thylakoid membrane rely on four integral membrane protein complexes, that includes PSI, PSII, Cytochrome-b_6f complex, and ATP synthase. Light is absorbed by PSII to trigger the light reaction, which initiates the charge separation at the

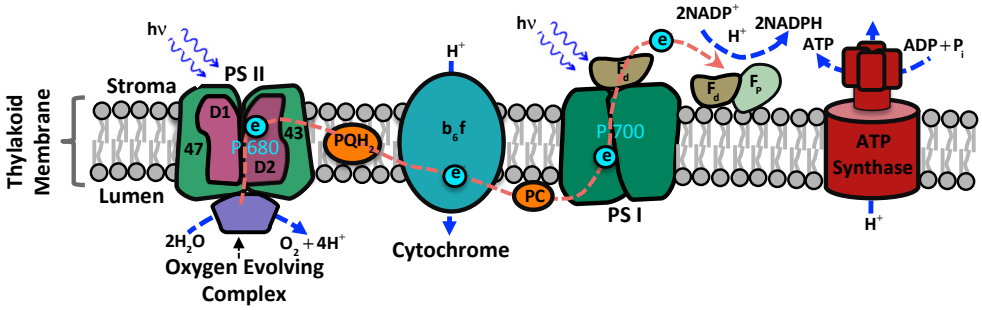

FIGURE 2.1: Schematic depiction of electron transport pathways during oxygenic photosynthesis in thylakoid membrane. The dashed arrow in orange colour reveal the electron transfer pathway. The main complexes involved in electron transport during photosynthesis are PSI, PSII, Cyt b_6f and ATP synthase. e and H^+ indicate the flow of electrons and protons, respectively. *Abbreviations* : PSI : Photosystem I, PSII: Photosystem II, PQ: Plastoquinone, PC: Plastocyanin, Fd: Ferredoxin and Fp: Ferredoxin-NADP Reductase.

RC, P680. The released electron is shuttled through electron carriers, i.e., plastoquinone (PQ), cytochrome b_6f and plastocyanin (PC) to PSI. The light harvesting antenna system of PSI further absorbs the light and funnels this energy to drive the electron translocation from PC to ferredoxin (F_d) [83]. The deficiency of the electron in PSII is restored by oxidation of water, which additionally releases protons into the thylakoid space. This will raise the number of protons in the thylakoid lumen. The higher concentration of protons in the thylakoid lumen compared to stroma will develop a proton gradient across the thylakoid membrane. From F_d the electron is further transferred to ferredoxin-$NADP^+$ reductase. The ferredoxin-$NADP^+$ reductase receives electrons, individually, from two reduced F_d molecules and drives the reduction of $NADP^+$ to NADPH. The reduction of $NADP^+$ further amplifies the proton gradient across the thylakoid membrane. Downflow of protons from higher to low concentration provides energy to the ATP synthase enzyme (a large complex of membrane-bound protein) to drive the synthesis of ATP. The dark reactions, which are also known as a carbon fixation or the Calvin cycle, further use ATP and NADPH for reduction of CO_2 to carbohydrates. The energy and electrons required for the synthesis

of sugar or glucose from water and CO_2, are provided by ATP and NADPH, respectively [84, 85].

2.2 Photosystem I

PSI is a large multi-subunit membrane bound pigment-protein complex, which drives a light-induced electron translocation from PC on the luminal side to F_d on the stromal side of the membrane [86]. Similar to other protein complexes, which are involved in oxygenic photosynthesis, PSI is also found in plants, algae, and cyanobacteria [83]. Considering the organization and composition, the PSI from higher plants and algae differs to the PSI from cyanobacteria. In higher plants and algae, PSI comprises of two moieties, i.e., a core complex and a peripheral light-harvesting complex (LHCI), while, in cyanobacteria, it is comprised of only the core complex lacking the peripheral LHCI. Also, in cyanobacterial membrane the PSI can exist both in trimeric and monomeric form, whereas, in higher plants and algae, it exists only in the monomeric form [87, 88]. The native conformation of PSI in cyanobacteria is not very clear though, but it is strongly believed that preferentially it organizes as a trimer [87, 88]. The transfer of energy and charge separation process is, however, equally efficient in both: monomeric and trimeric forms of PSI from cyanobacteria [89]. The crystal structures of the plant and cyanobacterial PSI shows that the central part of the PSI is formed of two similar large subunits PsaA and PsaB. These intrinsic subunits carry most of the PSI pigments and components of electron transport chain (ETC) including: A_0 (monomer of Chl *a*), A_1 (phylloquinone) and F_x (one of the three Fe_4S_4 clusters), which are involved in electron transfer from RC (P700) to electron acceptor F_x [83, 90]. Most of the cofactors present in PSI mainly participate in capturing the light, transportation of electron and protecting the complex against photodamage by dissipating the excess of energy [87, 90]. The composition, organisation and basic features of PSI complex are discussed in detail below.

2.2.1 PSI Core Antenna System

In higher plants and algae, the monomeric complex of PSI captures the light energy through a membrane integral LHCI which surrounds the core complex. This peripheral LHCI of plants consists of four different light-harvesting Chl *a* containing membrane proteins (Lhca1-Lhca4) which assemble into two dimers organized in a series forming a crescent-shaped strip that surrounds the PsaF side of RC. A crystal structure of the plant PSI at 4.4 Å resolution is shown in Fig. 2.2. The figure is taken from Ref: [83]. The LHCI has a very modular and flexible nature with very loose and fee-

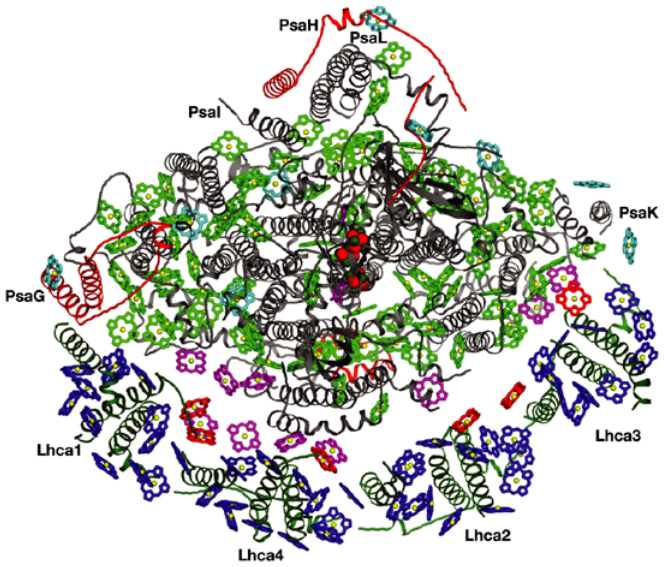

FIGURE 2.2: A view from the stromal side of the plants PSI. The Chl *a* molecules which are common both in cyanobacteria and plants are shown in green, while the novel structure elements which are present only in plants PSI are shown as red ribbons. Different colors are assigned to the Chl *a* molecules based on their specifications. Those indicated in cyan: are unique for plants, red: act as a LHCI linker Chl *a* and magenta: are designated as gap Chl *a* and are positioned within the cleft between reaction centre (RC) and LHCI belt [91]. In blue are the Chl *a* that are bound to the Lhca monomers (Lhca1-Lhca4). The red and green spheres in the centre of the complex are representing the three Fe_4S_4 clusters. This figure is taken from [83].

ble binding between Lhca monomers. The binding between RC and Lhca monomers is also quite weak, except for Lhca1, which shows a tight binding to the RC [91]. The crescent shape of LHCI and fine-tuned interactions

of Lhca with RC and with other Lhca monomers helps in achieving most efficient light harvesting, excitation energy transfer (EET) and coping with the environment which exhibit the dynamic variation in light intensity [36, 91]. The core complex of plant PSI is composed of 13-14 protein subunits, named as, PsaA-PsaL, PsaN and PsaO [83, 91]. The two principal subunits, PsaA and PsaB, forms the central part of PSI, which harbors most of the pigments of PSI and the components of ETC, which are involved in light-induced electron transfer from P700 to F_x. In addition, the core complex of plant PSI also contains ∼100 Chl *a* molecules, which function as an intrinsic light-harvesting antenna [83, 92]. The structural model of plant PSI RC revealed that the position and orientation of the vast majority of cyanobacterial antenna Chl *a* molecules is well-maintained. Out of 96 Chl *a* molecules of cyanobacterial PSI, 93 are found in the plant PSI RC. Only 3 Chl *a* molecules coordinated to the protein subunits PsaM, PsaX and PsaJ in cyanobacterial PSI RC, are missing. From the remaining 93 Chl *a* molecules, only one was altered at a significantly different position while the other 92 Chl *a* molecules were found at the very same position. Therefore, to adapt the plant RC to put to use the energy from the LHCI antenna only needs few additional Chl *a* molecules [93].

Contrary to PSI from higher plants and algae, the PSI from cyanobacteria lacks the additional peripheral LHCI antenna. In *vivo* depending on the environmental conditions, like light intensity and nutrient supply, cyanobacterial PSI exists both in monomeric and trimeric forms [86]. However, the trimeric form is more dominant in cyanobacteria [90]. Fig. 2.3 shows the structure of (a) a trimer from the stromal side and (b) exaggerated view of a monomer embedded in the membrane of PSI at 2.5 Å resolution. The figures are generated from protein data bank file (PDB ID: 1JB0) [18] by using molecular visualization software PyMol. In trimeric form, PSI adopts a clover-leaf-structure with a diameter of 220 Å and extends ∼90 Å into stroma. Each trimer comprises of 3×12 protein subunits (the protein backbones are depicted in light green), which further bounds 3×127 cofactors [86]. In monomeric form, the cyanobacterial PSI is smaller in size than

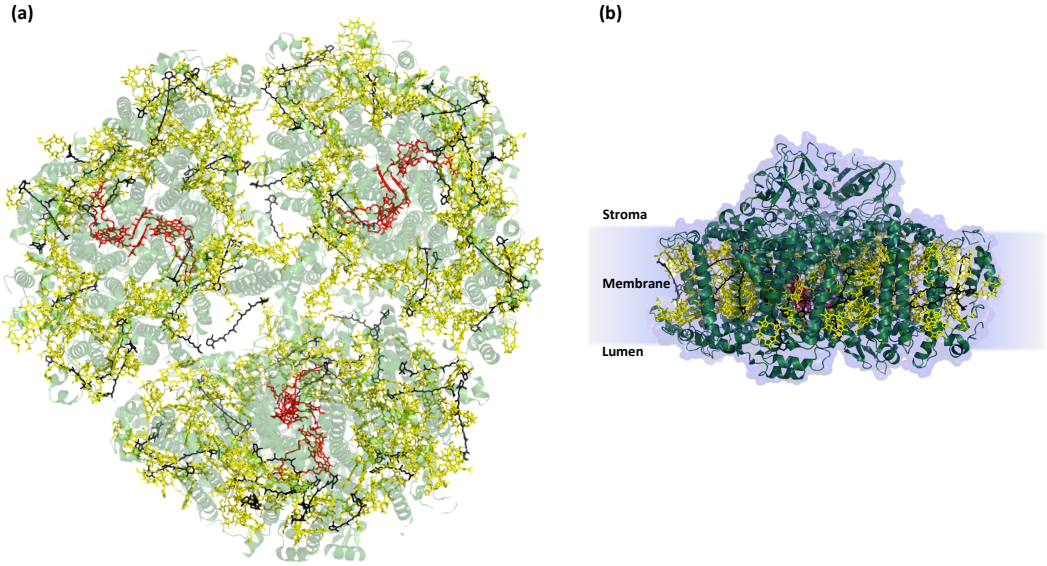

FIGURE 2.3: Structure of PSI from *Thermosynechococcus elongatus* (*T. elongatus*) at 2.5 Å resolution. (a) The view in trimeric form as seen from stromal side of the thylakoid membrane (PDB ID: 1JB0) [18]. Each monomer is composed of 96 Chl *a* molecules out of which 90 are shown in yellow, while those six which are part of ETC are represented in red. The carotenoids (22 per monomer) can be seen in black. The protein backbone is shown in dim green color. (b) a side view of whole monomer parallel to the membrane plane. The stromal side which provides the site for ferredoxin (Fd) docking is on top. Both the figures are generated by using molecular visualization software PyMol.

plant PSI and consists of 12 protein subunits compared to the 13-14 subunits of plant PSI [91]. These subunits, based on their genes, are named from PsaA-PsaX. The core antenna of each monomeric unit of cyanobacterial Thermosynechococcus elongatus (*T. elongatus*) comprises of 96 Chl *a* molecules, 22 carotenoids, three Fe_4S_4 cluster F_X, F_A, F_B, 2 phylloquinone and 4 lipids. Out of 96 Chl *a* molecules, 90 together with 22 carotenoids form the large internal antenna system which captures the light energy and very efficiently guide it to the core of RC [18, 90]. Fig. 2.4 shows the detailed view of PSI monomer where all cofactors (other than lipids) are indicated in different colors (the detail of the color codes is given in the figure caption). Of the remaining six Chl *a* molecules, the two (Chl a/a') which are oriented parallel and located in the centre of the structure forms the primary electron donor P700 while the two pairs positioned in proximity to P700 represent

the primary electron acceptor A and A_0 (see Fig. 2.4 (b)). Light-induced charge separation results in oxidation of the P700 and reduction of A_0. The electron is transferred via phylloquinone (cyan) to Fe_4S_4 clusters F_X, F_A and F_B, respectively [93].

The unit of the primary electron donor, primary electron acceptor and the cofactors those participating in electron transfer is recognized as an RC. In monomeric form all the antenna Chl *a* molecules arrange them almost elliptically in a bowl like structure, encircling the RC [86, 89]. Such a bowl like arrangement is very suitable to support the efficient energy transfer from antenna system to the RC which is prerequisite for an efficient photosystem. The antenna Chl *a* molecules are well parted with any of the RC Chl *a* molecules with a centre-to-centre distance $>$ 20 Å, while for any of two antenna Chl *a* molecules the centre-to-centre distance is in the range from 7-16 Å. The two antenna Chl *a* molecules positioned in close proximity to two Chl *a* molecules of RC at centre-to-centre distance $\sim$ 12.8 Å form a structural bridge between antenna system and RC. The centre-to-centre distance among Chl *a* of antenna system is well in range of Förster type energy transfer favoring the fast energy transfer among Chl *a* molecules [89, 90]. In Fig. 2.5, are displayed the absorption and emission spectra of PSI. The absorption spectrum is composed of several absorption bands. The main bands: in high energy region peaking around $\sim$430 nm (Soret band) and low energy region peaking around $\sim$680 nm (Q_y band) are due to Chl *a* of core antenna system [94–96]. The band around $\sim$450 nm (shown under the blue curve) is due to β-carotenoids. The β-carotenoids also contribute in light harvesting and absorb in the region ca. 400-500 nm. The emission maxima show strong temperature dependence. At room temperature (red), the prominent maxima is positioned at $\sim$690 nm (assigned to the bulk antenna Chl *a* molecules) with a proportionately larger shoulder at wavelength $\sim$720 nm (assigned to red Chls). As the temperature is reduced the yield of the F730 Chl *a* molecules (red Chls) increase and maxima at $\sim$730 nm become prominent (magenta). This is due to the decrease of population in the higher vibrational energy levels of first excited state of F730 Chl *a*

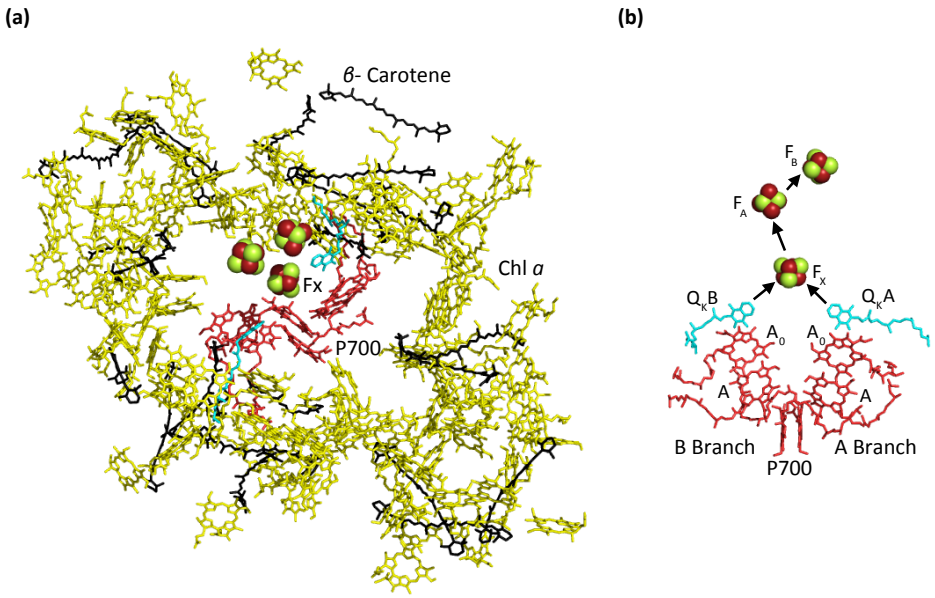

FIGURE 2.4: A view of PSI core antenna system responsible for efficient trapping and transfer of excitation energy. (a) Chl *a* molecules (90 in yellow and 6 in red) with carotenoids (black) and two phylloquinones (cyan) of the electron transfer chain (ETC) are shown as sticks while the three FeS clusters are shown as spheres in arbitrary colors. Sun light is absorbed and excitation energy is transfered by the Chl *a* molecules (yellow) to a few central Chl *a* (red) which belong to ETC in the same monomer that perform charge transfer and facilitates the conversion of the light energy into chemical energy. (b) A view of the light-induced electron transport pathway from P700 to F_B. The cofactors of the ETC of PSI shown from a side parallel to the membrane plane with stromal side on top and the lumen side at the bottom. A pair of the Chl *a* and Chl $a^{'}$ positioned at the lumenal side forms the primary electron donor P700, while the other constituents of the ETC includes two additional pairs of Chl *a* and two phylloquinones ($Q_K A$ and $Q_K B$, cyan) and three FeS clusters (F_X, F_A and F_B, shown as groups of spheres). Figures are generated from PDB ID: 1JB0 by using PyMol software.

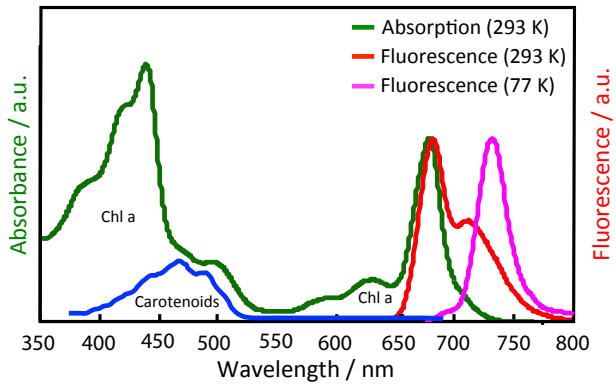

FIGURE 2.5: Absorption and emission spectra of PSI. The green curve is showing the absorption spectra of PSI while the red and magenta curves are showing the emission spectra at 293 and 77 K, respectively.

molecules with the decrease of temperature [97]. Therefore, the probability of EET from excited F730 Chl *a* to P700 diminishes, and the trapped energy is released as fluorescence. The yield of the fluorescence at 690 nm is reported to be independent of temperature [97].

2.2.2 Long Wavelength Chlorophyll (LWC)

In PSI, some of the Chl *a* molecules of the core antenna system which absorb at lower energies (longer wavelength) than primary electron donor P700, are called long-wavelength Chls or red-Chls [88, 90]. The number of these LWCs is different in different organisms and varies in the range between 3-10% of the total number of Chl *a* molecules. For instance, PSI from *T. elongatus* comprises of 9-11 LWC molecules per monomer and PSI of Synechocystis core complexes comprises of 3-5 red Chl *a* molecules [18, 89]. The functions of red Chls in PSI trimers are still a matter of debate. Depending on their position in the antenna system and their distance from primary electron donor P700, the red Chls may have different functions. One of the main roles may lie in increasing the absorption cross section of PSI and promoting the exchange of energy among the monomers of a single trimer [86, 87, 89]. It is also proposed that under extreme environmental conditions the LWCs may help in increasing the efficiency of capturing the light energy by concentrating the energy in the vicinity of P700 [87, 89, 98]. Additionally,

the LWCs may also have their role in protecting PSI complex against photodamage due to an excess of excitation light energy [87]. One school of thought also holds that these LWCs simply are an effect of relatively dense packing of Chl *a* molecules in the core antenna of PSI [89].

At room temperature, the energy absorbed by LWCs is efficiently transferred uphill to bulk Chl *a* molecules and afterwards to P700 where it is utilised to induce charge separation [99]. As a result, the charge separation yield at P700 reaches to above 95%. This uphill energy transfer is enabled by surrounding thermal energy. Therefore, at physiological temperature the LWCs do not affect the quantum efficiency of the photochemistry of PSI and the QY of oxidation of P700 is effectively independent of the excitation wavelength, even at wavelength up to 760 nm. But, at low temperatures the LWCs act as a trap for excitation energy and uphill energy transfer to P700 is blocked. As a result, the quantum efficiency of charge separation at P700 is decreased, and trapped energy at LWCs is released as fluorescence, increasing the fluorescence yield [88, 100].

The theoretical studies made on the bases of the 2.5 Å resolution structure of trimeric PSI from *T. elongatus* helped in identifying many strongly coupled Chl *a* aggregates forming the trimers and dimers of Chl *a* molecules. Most of the studies agreed that out of many Chl *a* aggregates present in PSI from *T. elongatus*, only one trimer on the luminal side of the complex B31/B32/B33 and the linker dimers near the stromal side of membrane A38/A39 and B37/B38 are the candidates of LWCs [18, 86, 99, 101]. Recently, through the fluorescence studies of the ensemble and the single-molecules at low temperatures, Schlodder *et al.*, have made the new assignments for the LWCs of trimeric PSI from *T. elongatus* [88]. They found that in the presence of oxidized $P700^+$ the fluorescence emission of the different LWC pools was quenched differently. Contrary to monomeric PSI, for trimeric PSI from both *T. elongatus* and *A.platensis* the fluorescence emission of LWC pools was quenched strongly ($\sim$ by a factor of 10), which indicates that the corresponding emitter Chl *a* aggregates emerged as a result of trimerization. They concluded that due to the strong quenching by

$P700^+$, the fluorescence emission of the several reddest states of trimeric PSI from *T. elongatus* actually escaped the detection. So they propose that the two chlorophyll trimers A31/A32/B7, A16/A17/A25 and three dimers B18/B19, B24/B25 and A26/A27 can be the additional potential candidates for the LWCs. The similar effects of $P700^+$ on the fluorescence yield of the red states from both: *T. elongatus* and *A.platensis* additionally suggest that the LWCs in both organisms are not so different but have same structural organization or even same structural identity [88].

2.2.3 Carotenoids

In PSI from *T. elongatus*, 22 carotenoids modelled as β-carotene have been identified from the X-ray structure at 2.5 Å resolution [18, 90]. Most of them are located deep in the membrane with only a few lying closer to luminal or stromal side. Besides maintaining the structure of the PSI, the carotenoids carry out two major functions, which include (i) light harvesting and (ii) protection against excessive light [86]. Despite being the part of the large core antenna system [90], the direct role of carotenoids in the electron transfer process has not been identified. The experiments performed on carotenoids deficient strains still showed the activity of charge separation, firmly proving their noninvolvement in the process [102].

Carotenoids absorb the light and transfer their excitation energy efficiently to the neighbouring Chl *a* molecules [98]. The main absorption of carotenoids lies in the gap between Soret and Q_x band in range between 400 - 570 nm, where the absorption of Chl *a* molecules is very weak. Carotenoids also form a direct tight interactions (van der Waals contact < 3.6 Å) with most (60 out of 96) of the Chl *a* molecules [18]. Thus, due to their ability to efficiently absorb the light in the deficient range of Chl *a* and the strong interaction with Chl *a* the carotenoids strongly contribute in light harvesting and energy transfer to the RC.

Preventing the damage against excessive excitation light is the another acute function of carotenoids for the stability of the PSI. The photo protection is carried out via quenching of highly damaging excited Chl *a* triplet states,

which otherwise can produce toxic singlet oxygen [86]. Chl *a* molecules in the triplet state can react very efficiently with oxygen to form extremely poisonous singlet oxygen. But the carotenoids dispersed over the whole antenna system make the numerous tight interactions with the Chl *a* molecules and quench their excited triplet states via a charge transfer mechanism [18].

2.2.4 Energy Transfer and Charge Separation

The process of capturing excitation energy by an antenna system and subsequently transferring it to the primary electron donor through a Förster-type energy transfer is called Light-Harvesting [103]. One of the most appealing features of the PSI is its capability of efficient light harvesting and migration of excitation energy to the RC for light-induced charge separation. EET is so efficient that almost every photon captured by the PSI drives and electron translocation [36]. In contrast to plant, the PSI from cyanobacteria has its own core antenna system for harvesting the excitation energy. The antenna pigments capture the excitation energy and very efficiently pass it Chl by Chl to primary electron donor (P700) through Förster-type energy transfer. Schematic illustration in Fig. 2.6 is an exaggerated representation of the principles of light-harvesting. At ambient temperatures due to the availability of sufficient thermal energy of the surroundings, the excitation energy is transferred to P700 (indicated by brown disc) through uphill energy transfer [88], where it is utilized for charge separation [86]. At cryogenic temperatures, the transfer of energy towards P700 is partially blocked and the red Chl *a* molecules (indicated by red discs) acts as a trap for the excitation. The red Chl *a* states becomes fluorescent and consequently the fluorescence yield of PSI increases while decreasing the quantum efficiency of charge separation (a better descriptive illustration of the process at cryogenic temperature is shown in Fig. 2.16 b).

In the centre of monomeric PSI is located the ETC (Fig. 2.4 b), functionally the most critical part of PSI, which facilitates the transmembrane charge separation and provides the pathway for efficient electron transfer across the membrane [86, 90]. Fig. 2.7 represents the exaggerated arrangement of

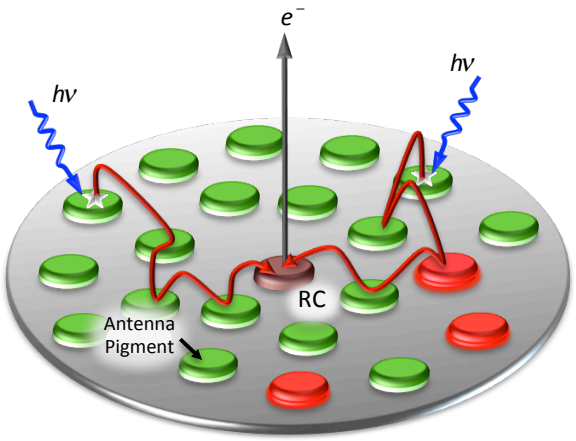

FIGURE 2.6: Illustration of excitation-energy transfer pathways at ambient temperatures. Captured energy is transferred stepwise to the RC P700. Upon excitation of P700 a charge-separated state across the membrane is generated. The red chlorophyll states (indicated by red discs) are also involved in energy transfer.

the cofactors of ETC, which are involved in electron transport. In total 11 cofactors which include: six Chl *a* molecules, two phylloquinone, and three Fe_4S_4 clusters termed as F_X, F_A and F_B are involved in the transfer of an electron in PSI. Six Chl *a* molecules, two phylloquinone and the Fe_4S_4 cluster F_X are bound to subunits PsaA and PsaB while F_A and F_B belong to PsaC [104]. A pair of Chl *a* molecules indicated as eC-A_1 and eC-B_1 constitutes the P700, while other 4 × Chl *a* molecules noted as eC-B_2, eC-A_2, eC-A_3, eC-B_3 and two phylloquinone Q_K-A and Q_K-B are arranged between P700 and F_X in two branches as pairs of molecules. The alphabets A and B are demonstrating whether its PsaA incorporating the axial coordination of Mg^{+2} ions or PsaB. An appealing fact is that the cofactors constituting one branch are not limited to only one subunit of PSI [90]. After absorption of light the primary electron donor, P700, gets excited and an electron is transferred rapidly (within 1-3 ps) to the primary acceptor, A_0, followed by further transfer along a series of secondary electron acceptors i.e., phylloquinone and three Fe_4S_4 clusters. After the docking of soluble protein F_d, the electron from iron-sulfer cluster reaches to F_d, which acts as a soluble electron shuttle [90, 105]. The electron is transferred to the Ferredoxin-$NADP^+$-reductase (FNR), which reduces the $NADP^+$ to NADPH [86]. To

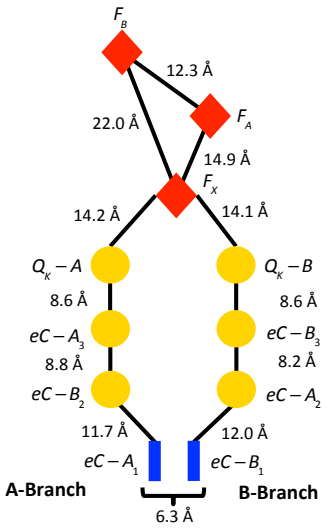

FIGURE 2.7: Schematic model adopted from [90], is representing the arrangement of cofactors those constitute the electron transfer chain (ETC) in PSI. The model is based on crystal structure of cyanobacterial PSI at 2.5 Å resolution [18]. The involved Chl *a* molecules are arranged into two branches, indicated as A and B-Branch. The Chl *a* molecules are denoted by eC-A_i /eC-B_i (i= 1,2,3), with letters A and B indicating the subunits PsaA and PsaB they are bound to. Q_K -A / Q_K-B are indicating the phylloquinone molecules bound to the respective subunits PsaA / PsaB. In Å are indicated the centre-to-centre distances between the corresponding cofactors.

complete the reaction cycle, $P700^+$ is re-reduced by cytochrome c_6 located at the inner (luminal) side of the complex [18, 86].

2.3 Plasmonic Interaction

Prior to the detailed discussion on the effects of plasmonic interactions on the optical properties of fluorophores understanding the origin of optical properties of molecules is essential. Therefore, before going into the deep discussion on MEF, a brief overview of the molecular photophysics is presented at the start of this section.

2.3.1 Absorption and Emission of Light

The excitation of the Chl *a* and carotenoids, present in the photosynthetic antenna complex, occur after the absorption of light of appropriate energy for electronic transition, which promotes the Chl *a* from the ground state (S_0)

to the excited state (S_n). There, different decay pathways e.g., fluorescence, internal conversion, intersystem crossing and non-radiative energy transfer to the RC contribute competitively to de-excite Chl *a* molecules. The energy transfer pathways and fluorescence of the Chl *a* molecules modifies when they interact with plasmonic NPs. Therefore, to understand the effects of plasmonic interactions on PSI it is required to first understand the process of light absorption and fluorescence emission.

The processes of the absorption and emission of light by a sample molecule are illustrated as a Jablonski diagram in Fig. 2.8. S_0, S_1, and S_2 depicts the singlet ground, first and second electronic states, respectively. Each of the electronic energy states is composed of multiple vibronic energy states indicated by black lines. Principally, each of the vibronic energy states can even be further segmented into rotational energy levels. The transition energy between the ground state S_0 and first electronic excited state S_1 is denoted by E_0 and is given by,

$$E_0 = h\nu_0 \tag{2.1}$$

After absorbing an incident photon of energy E_{abs}, the process of photoluminescence initiates and the fluorophore is excited to higher vibronic levels of higher excited states S_1 or S_2 (depending on the energy of the absorbed photon). The angular frequency $\nu_{abs} > \nu_0$.

$$E_{abs} = h\nu_{abs} = \frac{hc}{\lambda_{abs}} \tag{2.2}$$

whereas, h is the Planck constant of value 6.63×10^{-34} J.s, ν_{abs} is the frequency of the absorbed light, c is the velocity and λ is the wavelength of light. The straight arrows (blue) pointing upward are indicating the absorption transitions between the ground, first and second electronic state. The absorption is a very fast transition and takes place on the order of $\sim 10^{-15}$ *s*. At ambient temperature, the transitions generally start from the lowest vibrational level of the S_0. This can be explained considering the Boltzmann

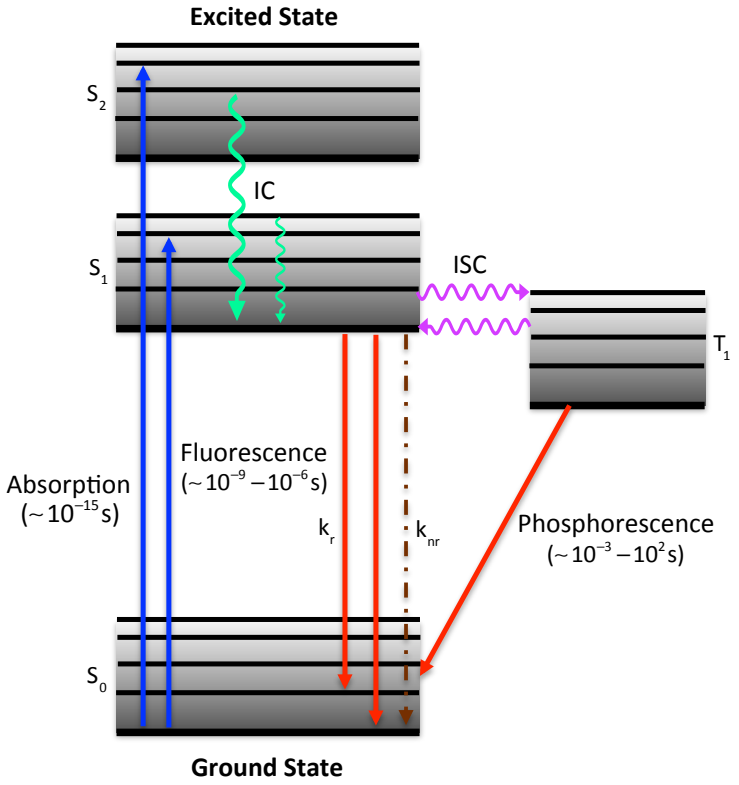

FIGURE 2.8: Jablonski energy diagram illustrating the possible transitions between electronic states of a fluorophore molecule (absorption of light (blue arrows), and involved emission processes i.e., fluorescence and phosphorescence (red arrows)) with respective time periods. The waved arrows are marking the non-radiative transitions named as internal conversion (IC, green arrows) and intersystem crossing (ISC, magenta arrow).

distribution function which measures the population of the energy levels (vibrational states) of molecules.

$$\frac{N_1}{N_0} = e^{\frac{-\triangle E_{vib}}{k_B T}} \tag{2.3}$$

whereas, N_0 and N_1 is the relative population of the lowest vibrational level and first higher vibrational level. $\triangle E_{vib}$ is the energy difference between the two vibrational levels, k_B is the Boltzmann constant and T is the absolute temperature. At room temperature the $\triangle E_{vib}$ (1000 - 3000 cm^{-1}) is much larger than $k_B T$ ($\sim$ 200 cm^{-1}), implying that only the lowest vibrational level is populated.

The interaction of the pigment with the electromagnetic field is the prerequisite for an optical transition. Therefore, it is necessary that the molecule has a dipole which is resonant with the frequency of the incident light. The coupling strength of the electromagnetic field and the electronic transition of a molecule is determined by calculating the transition dipole moment ($\vec{\mu}_{eg}$), which couples the wave functions of the ground (ψ_g) and excited (ψ_e) electronic states:

$$\vec{\mu}_{eg} = \int^{r} \psi_e^*(r) \cdot \vec{\mu} \cdot \psi_g(r) dr \tag{2.4}$$

whereas, μ= -er, with e the charge on an electron. The oscillator strength which often describes the strength of the optical transition is proportional to the magnitude of transition dipole:

$$f \propto |\vec{\mu}_{eg}|^2 \tag{2.5}$$

Once the fluorophore is excited, there are multiple pathways for it to relax and return back to the ground state. At first the vibronic relaxation, which is a non-radiative process where molecule looses the vibrational energy through collision with environment and internal vibration, will take place (as indicated by green wavy arrows) and fluorophore molecules will relax to the lowest vibronic level of first electronic state (S_1). This process is also termed as an internal conversion (IC). This process is very fast and occurs nearly within $\sim 10^{-12}$ s or even less [106, 107]. In the second phase, following the Kasha's rule, the molecule from lowest energy level of S_1 can return to ground state by emitting a photon of higher wavelength (lower energy) in $\sim 10^{-8}$ s through radiative decay process (k_r) named as fluorescence. The excited fluorophore molecule can also relax to the ground state by dissipating the excited state energy through a non-radiative decay (k_{nr}) process due to the internal mechanism or external quenching [108]. In external quenching process the energy is transfered either through Förster resonance process to the neighbouring pigment molecules (with a similar energy gap) or electron transfer to drive the photosynthesis. Yet another path a fluorophore molecule can follow to return to the ground state is intersystem crossing

(ISC) accompanied by spin conversion from an excited singlet state S_1 to so called excited triplet state T_1. Following the similar principle of fluorescence, the excited triplet state can also be de-populated through a process of radiative or non-radiative decay. The emission from T_1 through radiative decay is termed as phosphorescence and is very slow ($\sim 10^{-3} - 10^{2}$ s) process compared to the fluorescence. There is a possibility that a transition back to the excited singlet state from the excited triplet state may take place, consequently, inducing an emission transition to the ground state yielding a delayed fluorescence. Thus, the energy absorbed by the Chl *a* molecules will either: i) re-emit as a fluorescence, or ii) drive the photosynthesis, or iii) dissipate as heat. All of these decay processes contribute competitively to de-excite the Chl *a* molecules [107]. An increase in the rate of one of the de-excitation process will accordingly lower the the contribution of the two others. The process of external quenching is strongly temperature dependent as a result the fluorescence of the Chl *a* molecules and consequently the effects of plasmonic interactions will also be temperature dependent.

Since, the fluorescence always originates from the lowest vibrational level of S_1, thus, the energy of the emitting photons through fluorescence or phosphorescence process is typically less than the energy of the absorbed photons i.e., $E_{em} < E_{abs}$. Consequently, the fluorescence spectrum is shifted to higher wavelength than the corresponding absorption ($\lambda_{em} > \lambda_{abs}$) [109]. This difference between the absorption maxima and emission maxima is named as stokes shift after Sir. G. G. Stokes [110].

The Jablonski diagram is an easy way of understanding the transitions between the electronic states, but it is confined to showing only the energy relationships. The potential energy diagram provides a more useful way to view the properties of molecular excited states. It was approximated by Born-Oppenheimer that the reorganization of electrons which occurs during the excitation process is much faster than the movement of atomic nuclei. If viewed from the perspective of nuclear coordinates, the readjustment of the electrons will appear to occur while the nuclei were fixed. Based on this approximation, James Franck, and R. Condon formulated a principle

that the electronic transition occurs too fast for nuclei to respond. Since the mass of the nuclei is much larger than the mass of electron so, during the electronic transition heavier atomic nuclei will not have time to readjust and most likely their position in the molecular entity will not change. But, after the completion of absorption act, they will readjust. This readjustment will bring them into vibrations. This can be better explained by a potential energy diagram (Fig. 2.9) showing the potential energy of the molecule as a function of the distance of two electronic states.

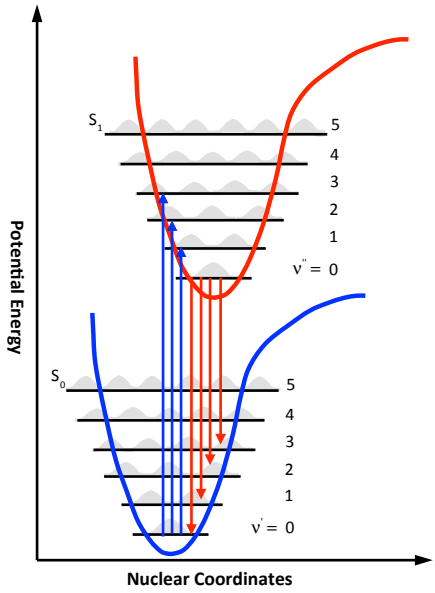

FIGURE 2.9: Frank Condon principle potential energy diagram. Potential curves for ground (S_0) and excited (S_1) states are shown together with few vibrational levels. Only the vertical transitions occur with a probability of the transition to a specific vibrational state described by the overlap integral between of the initial and final vibrational states.

After the absorption of a photon the molecule will jump to higher excited level and find itself in a non-equilibrium state so began to vibrate. This vibration can be understood as the molecule is running down, up, and down again, etc., like a pendulum along the upper potential curve. The periods of these vibrations are of order $\sim 10^{-13}$ s, while the lifetime of the excited electronic state is of the order of $\sim 10^{-9}$ s. Therefore, during the excitation period, there is enough time for thousands of vibrations.

The Franck-Condon principle states that a molecule may undergo a transition to a different, higher vibrational level in an excited state. However, the most intense vibronic transition occurs from a ground vibrational state to an excited vibrational state vertically above it. The probability of the vibrational transition to a specific vibrational state is proportional to the overlap integral between the initial and final vibrational states. Taking into account the Born-Oppenheimer approximation the wavefunctions in Eq: 2.4 can be split into the nuclear coordinates and the electronic coordinates. The transition dipole thus is factored into an electronic and a nuclear part:

$$\vec{\mu}_{eg} = \int \psi_e^*(r)\,\psi_v^*(R)\;\cdot\;\vec{\mu}\;\cdot\;\psi_g(r)\,\psi_v(R)\,dr_{elect}\,dR_{nuc} \tag{2.6}$$

$$\vec{\mu}_{eg} = \int^{r} \psi_e^*(r)\;\cdot\;\vec{\mu}\;\cdot\;\psi_g(r)\,dr_{elect} \int^{R} \psi_v^*(R)\,\psi_v(R)\,dR_{nuc} \tag{2.7}$$

The first integral is referred as electronic transition matrix element while the second term is the overlap integral of vibrational wavefunctions termed as Franck-Condon vibrational overlap. The Franck-Condon overlap determines the strength of the electronic transition.

Fluorescence Lifetimes and Quantum Yields: Fluorescence lifetime and QY are the two essential parameters for describing a fluorophore. The modifications in the fluorescence properties of fluorescent molecules (in our case PSI) due to coupling with metallic NPs can originate from the modification of either absorption or emission process [111, 112]. To define the modifications in the emission process it is essential to have the knowledge of fluorescence lifetime and the QY. Therefore, in this section a brief description of the fluorescence lifetime and QY is given.

The fluorescence lifetime (τ) is defined as the average time a molecule stays in the excited state [109]. After excitation, the fluorophore molecule gets excited and stays in the excited state for a certain time before emitting a photon and returning back to the ground state. This time ranges from 10^{-9} - 10^{-12} s. Fluorescence QY (ϕ_F), on the other hand, is described as the number of the emitted photons relative to the absorbed photons [106]. Both, the

fluorescence lifetime and QY can be explained considering the radiative (k_r) and non-radiative (k_{nr}) decay rates illustrated in the Fig. 2.8. The QY of the fluorescence can be expressed as,

$$\phi_F = \frac{\text{Number of photons emitted}}{\text{Number of photons absorbed}} \tag{2.8}$$

In the form of k_r and k_{nr} it can be described as:

$$\phi_F = \frac{k_r}{k_r + k_{nr}} \tag{2.9}$$

ϕ_F can vary in a range between 0 and 1 depending on k_r and k_{nr}. If k_{nr} is much smaller compared to k_r i.e., $k_{nr}<k_r$, ϕ_F can extend close to unity, but will always be less than unity because of the Stokes losses [106, 108]. The fluorescence lifetime, τ, of a fluorophore takes into account the combined rate of both the k_r and k_{nr} [113] and is stated as:

$$\tau = \frac{1}{k_r + k_{nr}} \tag{2.10}$$

If the non-radiative decay rate is ignored and de-excitation is considered only through radiative decay, the intrinsic lifetime, which is also termed as natural lifetime [106], can be given by:

$$\tau_0 = \frac{1}{k_r} \tag{2.11}$$

The fluorescence QY, thus will be:

$$\phi_F = \frac{k_r}{k_r + k_{nr}} = \frac{\tau}{\tau_0} \tag{2.12}$$

2.3.2 Inter-Pigment Interactions and Energy Transfer

It was established long ago in 1932 by Emerson and Arnold [114] that the photosynthetic complexes are composed of hundreds of pigment molecules.

Later, the structural studies showed that the pigments hold a precise placement and specific orientations with an exceptional degree of the organization [18, 36, 115]. Generally, they are very tightly packed with many of them having a centre-to-centre distance in a range from∼8-14 Å [116]. So the interaction energies between them may vary from strong to weak, giving an indication of strong or weak couplings, respectively [117]. In weak coupling regime, the EET from donor to acceptor only occurs after the complete vibrational relaxation of the excited donor which is also termed as an "incoherent hoping" or "incoherent energy transfer" [118]. The excitations and wavefunctions are essentially localized on the individual pigments only. The absorption spectra of the pigments remains unchanged [119] and the EET proceeds in nanoseconds evidencing the small coupling energy compared to the width of the vibrational energy levels [118]. In strong coupling regime, on the other hand, the interaction energy exceeds the difference of the energy levels of individual molecules and the EET is exceptionally fast even below 1 ps [118, 119]. The transfer of excitation energy in weak coupling regime can be explained by taking into account the Förster [120] or Dexter [121] transfers, while the strong regime case is discussed considering the transfer of an exciton. For instance, for energy transfer between different pigments at longer distances e.g., from a Chl *b* molecule to Chl *a* molecule the transfer of energy follows the resonance energy transfer mechanisms, while for the identical molecules e.g., Chl *a* which are so close that they behave as a single molecule, the transfer of energy takes place through exciton transfer mechanism [119]. During this thesis, the interaction of multi-chlorophyll binding pigment-protein complex PSI with metallic NPs have been studies. This involves all the stated mechanisms. Therefore it is important to understand and describe these mechanisms.

2.3.2.1 Förster Transfer

Förster mechanism leads the transfer of excitation energy (not electron) from an excited donor (D^*) to an acceptor (A) in the ground state, through a non-radiative process of energy transfer. Fig. 2.10 illustrates the schematic

diagram of the process. Generally, the Förster process is based on a dipole-dipole electromagnetic interaction and occurs from the singlet donor to singlet acceptor. Due to an interaction of the D* dipole (excited electron of lowest unoccupied molecular orbital (LUMO)) with the A dipole (unexcited electron of the highest occupied molecular orbital (HOMO)), resonance energy is transported from the D* to A via coulombic interaction. As a result, the donor molecule relaxes back to the ground state and the acceptor molecule gets excited. The key requirements for a highly efficient FRET between two pigments are; (i) the donor and acceptor pigments should be in close proximity to each other and inter-pigment distance should be in the range of 1 - 10 nm; (ii) the emission spectrum of the donor pigment must have a significant overlap with the absorption spectrum of the acceptor pigment; and (iii) the relative orientations of the transition dipoles of the donor and acceptor pigments should be preferably parallel to each other [122]. The rate (k_F) of the FRET between donor and acceptor pigments is

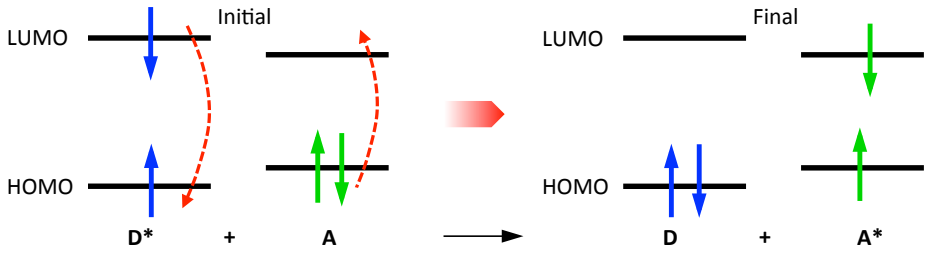

FIGURE 2.10: Schematic diagram for Förster energy transfer process. The asterisk denotes the excited state.

given by eq. 2.13:

$$k_F = \frac{1}{\tau_D}\left(\frac{R_0}{r}\right)^6 \tag{2.13}$$

whereas τ_D denotes the lifetime of the D excited state in the absence of A, r is the D-A separation and R_0 is the critical transfer distance and is defined as the distance at which the probability of the excitation transfer is equal to the spontaneous deactivation of the donor [123]. Typically, R_0 is in the range 20 - 60 Å, however for efficient acceptors it can even extend to 100 Å.

Mathematically it can be described as [106, 122, 124]:

$$R_0^6 = \frac{9000(\ln\ 10)\kappa^2 \Phi_D}{128\pi^5 N n^4} J \tag{2.14}$$

whereas κ is the orientation factor describing the relative orientation of the donor and acceptor dipoles, Φ_D is the fluorescence QY of the donor, N is the Avogadro number, n is the refractive index of the medium and J is the degree of spectral overlap between the donor emission and acceptor absorption integral. The orientation factor κ is specifically is given as:

$$\kappa = \cos(\phi_{DA}) - 3\cos(\phi_D)cos(\phi_A) \tag{2.15}$$

ϕ_{DA} denotes the angle between the transition moment vectors of both the donor and acceptor molecules, while ϕ_D and ϕ_A are the angles between the respective transition moment vectors and the direction from D to A. As can be seen in Fig. 2.11. The spectral overlap integral can be given as:

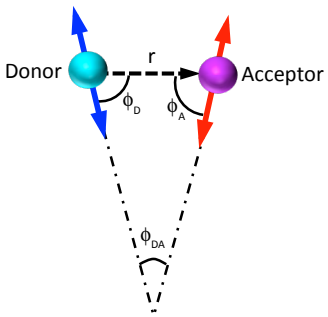

FIGURE 2.11: Illustration of the transition moment vectors of the interacting dipoles and angles between them relevant to the orientation factor. r is the D-A separation. Figure is adopted from [125].

$$J = \int_0^\infty F_D(\bar{\nu})\epsilon_A(\bar{\nu})\frac{d\bar{\nu}}{\bar{\nu}^4} \tag{2.16}$$

where $F_D(\bar{\nu})$ is the fluorescence spectrum of the donor and $\epsilon_A(\bar{\nu})$ is the absorption spectrum of the acceptor [123]. The FRET efficiency is inversely proportional to the sixth power of the D-A separation [106] as described

in eq:

$$E = \frac{R_0^6}{R_0^6 + r^6} \tag{2.17}$$

In LHCs the surrounding mediums maintain the fixed spatial relationships between the key pigment molecules to achieve the high efficiency of the energy transfer process [117].

2.3.2.2 Dexter Transfer

Contrary to FRET, in Dexter mechanism, the electronic energy transfer is accomplished by the actual exchange of an electron between the donor and acceptor pigments [121]. The mechanism is schematically described in Fig. 2.12. Two electron exchange processes, including the transfer of the excited electron of D to the LUMO of A and from the HOMO of A to the corresponding orbital of D occurs simultaneously. Unlike the sixth

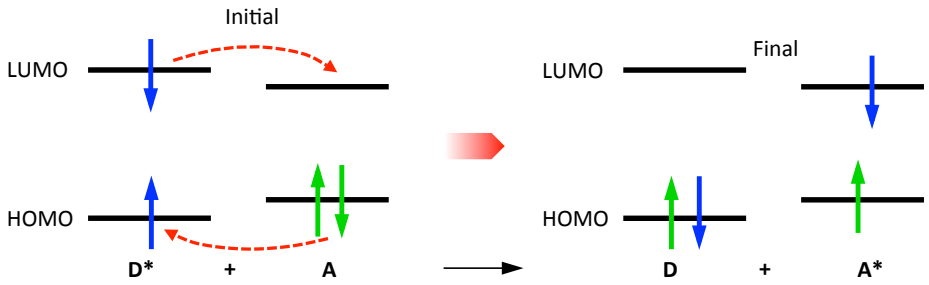

FIGURE 2.12: Dexter energy transfer process. The notions D and A denotes the energy donor and energy acceptor, respectively.

power distance dependence of FRET, the rate of Dexter transfer decreases exponentially with the distance given as [124, 126]:

$$k_F = CJ \exp\left(\frac{-2r}{L}\right) \tag{2.18}$$

whereas, J is spectral overlap integral as given in eq. 2.16, C is experimental constant, r is the D-A separation and L is the sum of van der Waals radii. Usually, both singlet and triplet excitons can be transferred in this process. The necessary condition for this process to take place is a strong overlap between the wave functions of donor and acceptor molecules [121,

124]. Thus, the exchange mechanism typically occurs over shorter distances within 10 Å and is also termed as a short-range energy transfer. The energy transfer processes which involve the long distances follow the Förster mechanisms while those involving the short-range transfers follow the Dexter mechanism.

2.3.2.3 Exciton Transfer

In strong coupling regime, many pigments are closely associated with certain strengths of interaction where the mutual coupling energy is larger than the width of the vibrational levels. The excitations are no longer localized to individual pigments, rather, are simultaneously extended over many coupled pigments (delocalized). The interacting pigments now effectively behave as a one big super-pigment and the state of the system is described by the combination of the wave functions of involved pigments [119]. The spectral and dynamic properties of the pigments are modified. The EET is too fast to resume Förster transfer or Dexter transfer [118, 119]. Therefore, the transfer of excitation energy will proceed following the exciton theory.

In a simple system of two pigment molecules which are in close proximity and interacting through the strong coupling, the excited energy of both will split into two new energy levels, one blue and one redshifted by an energy V_{ij} relative to the original energy level of individual separate pigments. Depending on the relative orientations of the transition dipole moments and separation between the individual pigments the new oscillator strength will arise. The interaction energy between the two pigments i and j is given by the formula [127]:

$$V_{ij} = \frac{\vec{\mu}_i.\vec{\mu}_j}{\vec{r}_{ij}^3} - 3\frac{(\vec{\mu}_i.\vec{r}_{ij}).(\vec{\mu}_j.\vec{r}_{ij})}{\vec{r}_{ij}^5} \tag{2.19}$$

whereas, $\vec{\mu}_i$, $\vec{\mu}_j$ are the transition dipole moments and $\vec{r}_{ij}$ is the distance between the pigments i and j. The interaction energy will decrease with the increase of the distance between the pigments. Due to such interactions, the absorption range of photosynthetic complexes increase and they can cover a vast range of the visible spectrum and efficiency of light collection increases.

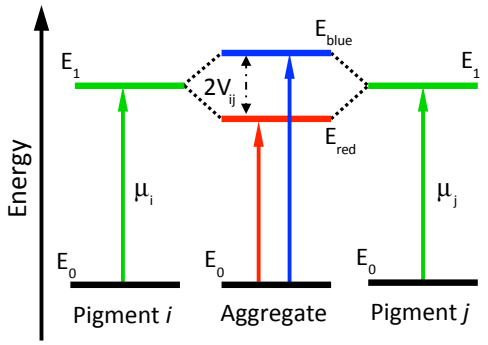

FIGURE 2.13: Excitonic interaction between the two pigments i and j. The excited states of two degenerate exciton-coupled pigments are split into two new energy levels E_{red} and E_{blue} shared by the involved pigments. The new energy levels are separated by $2V_{ij}$.

2.3.3 Interactions with metallic NPs

Metallic NPs, because of their ability to influence the fluorescence of neighbouring fluorophores, have attracted a lot of attention in the last few decades [68, 128–132]. Depending on their size and distance from the fluorophore, metallic NPs have been widely discussed to cause the quenching or an enhancement in the fluorescence emission and modification in the EET in PSI [67, 111, 133–136]. Before discussing the interaction of the PSI with metallic NPs and, thus, the enhancement in fluorescence emission, it is useful to first discuss the fundamental optical property, i.e., surface plasmon resonance (SPR) of the metallic NPs which causes the modifications in the fluorescence emission of the fluorophore.

2.3.3.1 Surface Plasmon Resonance

The NPs of the noble metals such as gold (Au) and silver (Ag) are known to exhibit the unique optical properties, like SPR, which are decidedly different from those of bulk metals. Surface plasmons are the coherent oscillations of the conduction electrons on the surface of the metallic NPs [137, 138]. If a light of the specific frequency, which matches the oscillations of plasmons, is incident the surface plasmons oscillate in resonance with incident light. This phenomenon is termed as an SPR [130, 138].

When a metallic NP with spatial dimensions much smaller than the wavelength of incident light is perturbed by an incoming external resonant light the free conduction electrons are moved away from their equilibrium position with respect to the positive ions, (see Fig. 2.14). This polarization of conduction electrons sets up a restoring force so electrons bounce back and forth resulting a coherent oscillation [68, 139], termed as a surface plasmon oscillation. These surface plasmon oscillations for being resonant with the frequency of incident external light are named as an SPR [140, 141]. The

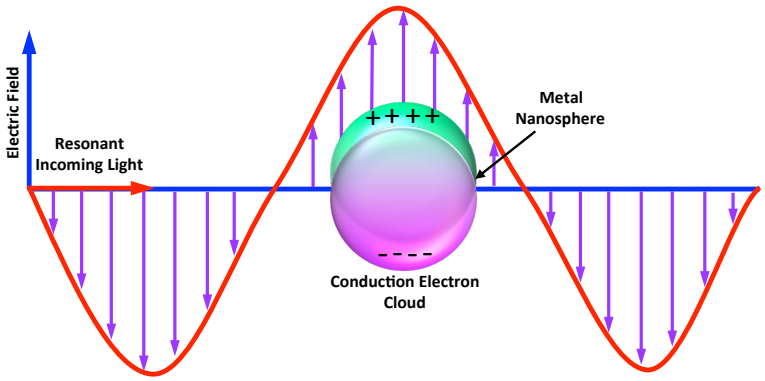

FIGURE 2.14: Schematic representation of surface plasmon resonance (SPR) for a metallic nanosphere. When incident with an external light, the cloud of conduction electrons of the show the oscillations relative to the nuclei.

localized SPR (LSPR) is responsible for enhancing the electromagnetic field which further leads to an enhancement in fluorescence emission [68, 137]. The spectral position of the LSPR can be tuned by controlling the morphology i.e., size and shape of the metallic NPs [130, 142]. This is because the change in the shape and size of the NPs changes the surface geometry and consequently shifts the electric field density on the surface. As a result, the oscillation frequency of the surface electrons changes and different cross-sections are generated for the optical properties, such as, absorption and scattering [137].

Variations in temperature also have a strong impact on the optical properties of the plasmonic nanoparticles. It has been shown by our group Konrad *et al.* [143] and others [144] that with an increase in temperature the linewidth of

the plasmon resonances increases linearly. The major contribution for dephasing of the plasmonic NPs is due to the increase in electron-phonon scattering. The conduction band electrons can interact with the occupied phonon modes of the particles. For temperatures higher than the Debye temperature as all the phonon modes are occupied, therefore, the phonon coupling increases linearly with temperature resulting the dephasing of the plasmon. Other mechanisms including electron–electron scattering, electron–surface scattering and radiative damping are regarded as independent of temperature and do not contribute significantly in dephasing of the plasmonic NPs [143]. In addition, the dielectric constant of the medium also show slight variations from LHe to room temperature. As a result the peak position of SPR also shifts towards red [144]. The effect of temperature on the linewidth and peak position of SPR of the plasmonic NPs can considerably influence the spectral overlap between the SPR and the absorption and (or) emission spectra of fluorophores at different temperatures and consequently the temperature dependent metal enhanced fluorescence (MEF).

2.3.3.2 Metal-Enhanced Fluorescence (MEF)

In this section, we have discussed the interactions between plasmonic NPs and fluorophores, which causes dramatic modifications (enhancement or quenching) in the fluorescence emission of the fluorophores. The metallic NPs (Au or Ag) are usually used to study the enhancement of fluorescence emission. Both of these metals have their own pros and cons. For instance, silver nanoparticles (AgNPs) have reduced optical absorption in the visible region of the electromagnetic spectrum and results in a higher enhancement due to their sharper plasmonic peaks and stronger inter-particle near field coupling effects. However, AgNPs are highly unstable in biological environments and also oxidize rapidly. In contrast, the gold nanoparticles (AuNPs) though have higher optical absorption than AgNPs, but are more stable in biological environments, easier to synthesize uniformly, and highly resistant to oxidation [68, 134, 145, 146]. Therefore, the choice of the particular metal is made depending on the desired application.

2.3.3.2.1 MEF Mechanism for QDs/Dye Molecules: The origin of the modifications in the emission properties of the fluorophore due to interaction with plasmonic NPs is linked to the modifications in both of its absorption and emission processes. The interaction of the metallic NPs can leave three possible effects: (i) an enhancement of the excitation rate; (ii) a modification of the radiative decay rate of the fluorophore; and, (iii) a non-radiative energy transfer from fluorophore to the metallic NP in the vicinity [64, 112, 145]. These possible mechanisms are displayed by exaggerated Jablonski diagram in Fig. 2.15.

The effect of increased excitation rate and subsequent increase in fluorescence emission is based on the metal-induced increase in the local incident field on the fluorophore [64]. As discussed in the previous section, the local electric field near the surface of the metallic NPs strongly increases when the surface plasmons get coupled to the electromagnetic field of incident light. This locally enhanced field causes an enhancement in the excitation rate of neighbouring quantum dots (QDs) or dye molecules and consequently an enhancement in fluorescence emission [130]. Fig. 2.15 (b) shows this effect. After absorbing a photon of energy hν, the fluorophore is excited to S_1 singlet state, where after staying sometimes it returns back to ground state either by releasing a photon with radiative decay rate Γ_r^0 or through non-radiative decay process with rate Γ_{nr}^0. The increased thickness of the blue and red arrows indicates an increase in excitation rate and thus an increase in the fluorescence emission, respectively. This is because of the fact that the power of fluorescence emission is proportional to the photon flux of the excitation, which in turn, is proportional to the square of the electric field [145]. This can be described mathematically as:

$$P_{em} = kn\phi_F^0 \tag{2.20}$$

where P_{em} is the emission power, k is the absorption cross-section, n is the photon flux and ϕ_F^0 is the fluorescence QY of the fluorophore [145] and

$$n \propto |E|^2. \tag{2.21}$$

Thus, with an enhancement in the local electric field, the photon flux of excitation will increase and so will be the fluorescence emission of the fluorophore.

In order to discuss and understand the effect of increasing intrinsic radiative decay rate in a better way, the modified Jablonski diagram is shown in Fig. 2.15 (c). Considering the fluorophore free of quenching, the fluorescence QY in the absence of the metallic NP can be expressed as:

$$\phi_F^0 = \frac{\Gamma_r^0}{\Gamma_r^0 + \Gamma_{nr}^0} \tag{2.22}$$

The QY is a reflection of the competition between radiative and non-radiative rates [64]. The fluorescence lifetime is thus given as:

$$\tau_0 = \frac{1}{\Gamma_r^0 + \Gamma_{nr}^0} \tag{2.23}$$

The natural lifetime (τ_n) is the inverse of Γ_r^0 only with $\Gamma_{nr}^0 = 0$. This leaves the $\phi_F^0 \approx 1$. The presence of the metallic NPs in the vicinity will modify the radiative decay rate, and therefore QY and lifetime of the fluorophore. This modification is assigned to the interactions of the excited state of the fluorophore with the conduction electrons of the metallic NPs [130]. The modified QY can be expressed as:

$$\phi_F^M = \frac{\Gamma_r^0 + \Gamma_r^M}{\Gamma_r^0 + \Gamma_r^M + \Gamma_{nr}^0} \tag{2.24}$$

whereas, ϕ_F^M expresses the QY in the presence of the metallic NPs and Γ_r^M is new additional radiative rate factor. The value of Γ_r^M can vary between

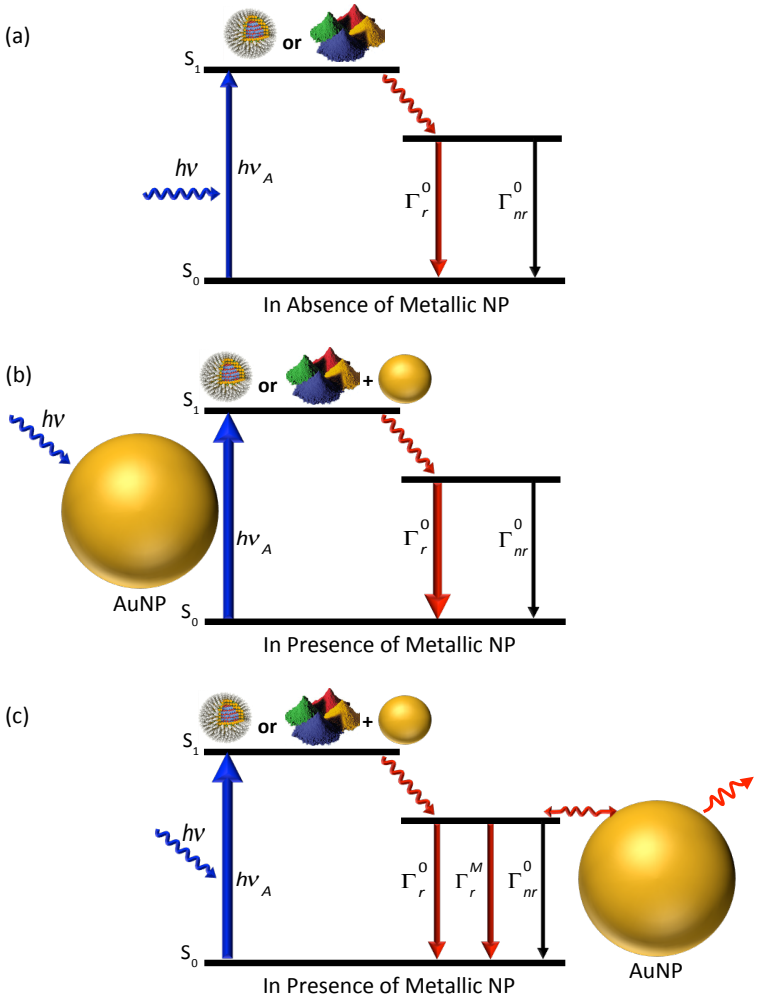

FIGURE 2.15: Plausible mechanisms of MEF for simple emitters e.g. quantum dots and dyes (a) Classical Jablonski diagram in free space. (b) Excitation rate (or absorption) enhancement by locally increased electromagnetic field due to AuNPs in proximity. The increase in excitation rate subsequently increases the emission of the fluorophore. The increased thickness of blue and red arrow indicates the increased rate of excitation and emission. (c) Fluorescence emission enhancement of AuNP-fluorophore unified system due to partial coupling between surface plasmons of AuNP and excited state of fluorophore. Γ_r^0 and Γ_{nr}^0 denotes the radiative and non-radiative decay rate, respectively. The figure is re-produced following Geddes *et al.* [64].

-Γ_r^0 to ∞ [147]. The modified lifetime, thus, can be described as:

$$\tau_0 = \frac{1}{\Gamma_r^0 + \Gamma_r^M + \Gamma_{nr}^0} \tag{2.25}$$

An increase in Γ_r^M leads to an increase of the QY, but the lifetime decreases. From eq. 2.24 it is perceived that the increase in QY will be optimum when Γ_r^M is comparable to Γ_{nr}^0. As the fluorophores with low initial fluorescence QY have $\Gamma_{nr}^0 > \Gamma_r^0$, so they will experience stronger enhancement in Γ_r^M and consequently a stronger enhancement in ϕ_F^M and the EF. However, the ϕ_F^M of a fluorophore with initial QY unity cannot be further increased by an increase in Γ_r^M, but, the lifetime can be decreased [147]. There is also a possibility that energy is transferred from the fluorophore to the metallic NP which may radiate and resultant emission will be from the metallic NP [148].

In the case of non-radiative energy transfer, the neighbouring metallic NPs can cause the damping of the dipole oscillations and an energy transfer from the excited dipole of the emitter to the metallic NP is induced when they are very close, leading to the quenching of the fluorescence [64, 130]. This process is strongly distance dependent [67] with an inverse proportionality to the third power of metal-fluorophore distance [64, 145]. The quenching mechanism has a strong dominance at a distance < 5 nm [67, 149–151].

The EF, which is defined as the relative intensity of the metallic NP coupled fluorophore with respect to the uncoupled fluorophore, hence, can be given as a combination of modification of absorption process (in the form of modification of the local electric field) and emission process (in the form of modifications in the QY) [111]:

$$EF = M_{LF}.\frac{\phi_F^M}{\phi_F^0} \tag{2.26}$$

whereas, M_{LF} denotes the local field intensity enhancement. This combination of modification of excitation rate and QY determines if the fluorescence will be enhanced or quenched as a result of the coupling with metallic NPs.

2.3.3.2.2 MEF Mechanism for PSI: Defining a mechanism for MEF of simple emitters such as a dye or QDs is relatively easy. However, for multi-chromophoric systems, like PSI, featuring multiple energy transfer pathways within the complex, understanding the MEF process and assigning a certain mechanism is highly challenging. Nonetheless, the enhancement in the fluorescence emission of PSI can be discussed considering: (i) the enhanced excitation rate; (ii) modifications in energy transfer pathways due to the electric field of plasmons; (iii) enhanced fluorescence emission channels; and, (iv) initial fluorescence yield of the PSI. An illustration of these possible factors has been displayed in Fig. 2.16.

Under physiological conditions, the light is harvested by the antenna system of PSI and transferred to the RC where light-induced charge separation takes place (Fig. 2.16 (a)). As the temperatures start decreasing, the red Chl *a* starts behaving as a trap for the excitation energy and at very low temperature the transfer of energy from the red Chl *a* molecules to the RC is partially blocked as a result the quantum efficiency of charge separation is reduced and fluorescence yield starts increasing [88]. The increased fluorescence emission from red Chl *a* molecules is indicated by the glowing red discs in Fig. 2.16 (b). The presence of the metallic NPs in vicinity results further increase in fluorescence emission of the PSI. Time-resolved fluorescence measurements have assigned a major contribution of fluorescence emission enhancement to the increased excitation rate [152, 153]. Bringing a metallic NP in the close proximity enhance the local incident field and subsequently the excitation rate and fluorescence emission of the PSI (as discussed in the previous section for simple emitters such as dye molecules or QDs).

In addition, the metallic NPs in the vicinity are capable of altering the FRET among chromophores by altering the Förster interaction distance [100, 154]. The interaction of the metallic NPs with coupled chromophores altered the Förster interaction distance between them from 8.3 to 13 nm [154]. In PSI, to ensure the fast and highly efficient EET to the RC the chromophores have specific orientations, spectral overlaps and spatial separations [89, 155]. Due

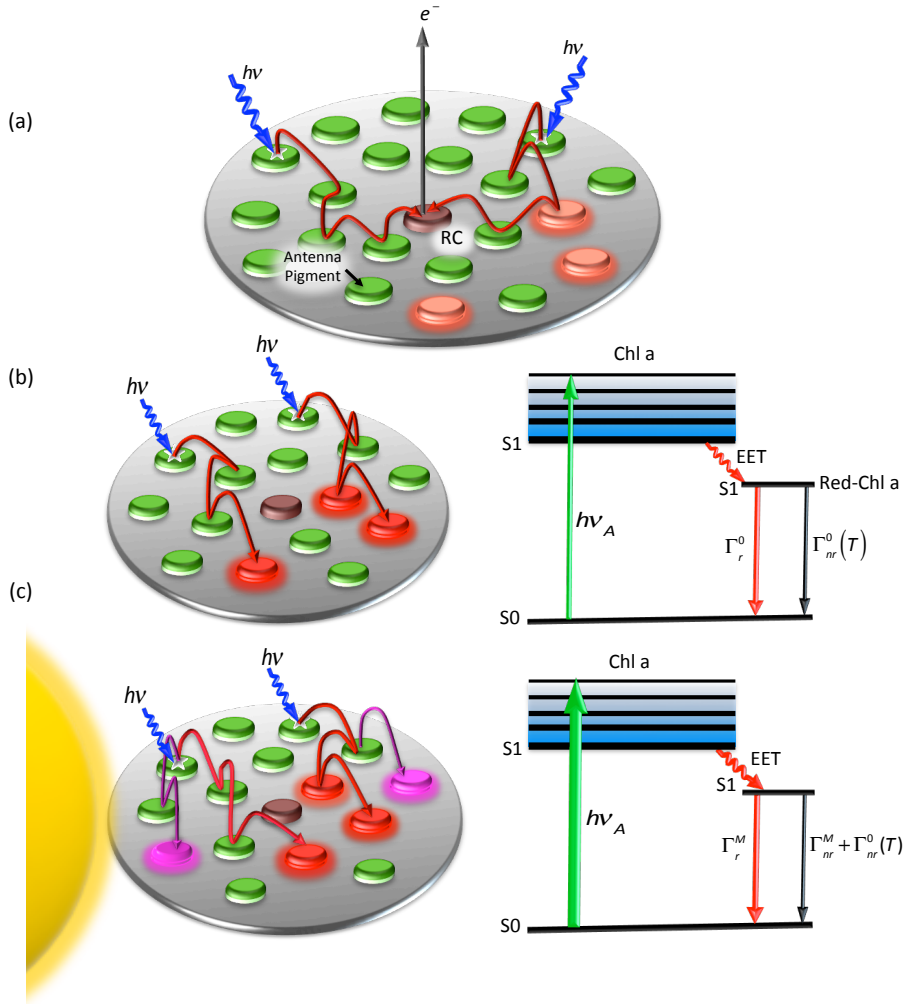

FIGURE 2.16: (a) Illustration of the EET pathways within PSI at ambient temperature. The excitation energy is transferred to reaction centre (RC) P700, resulting in a photo induced charge-separated state. (b) At cryogenic temperatures, the transfer of excitation energy to the RC is partially blocked and the red chlorophyll states become fluorescent. A modified Jablonski diagram for the fluorescence emission of PSI is illustrated on the right side. (c) AuNPs in the close vicinity increases the excitation rate, which causes an increase in fluorescence emission. Additionally, AuNPs alter the Förster-interactions between chromophores resulting in the generation of new EET pathways (purple lines) and emission channels (magenta discs).

to these specific coupling conditions among chromophores, a characteristic set of transition rates and consequently preferred energy transfer pathways exist between the chromophores [155, 156]. Considering a similar effect of the metallic NPs, it is assumed that the Förster distance among the chromophores within PSI will change and the specific coupling will be affected. As a result, new energy transfer pathways among chromophores will generate and resultantly the chromophores which in their native state were inactive will also get activated and participate in fluorescence emission. The magenta arrows and discs in Fig. 2.16 (c) are representing the exaggerated new energy transfer pathways and emission channels, respectively. Generation of new energy transfer pathways and activation of new emission channels will contribute to the enhancement of fluorescence emission of PSI.

The initial fluorescence QY of the PSI should also be considered while discussing the enhancement in fluorescence emission. The fluorescence yield of the PSI is highly temperature dependent [157, 158]. The non-radiative decay rate of PSI gets activated at higher temperatures and yields a low initial fluorescence yield [157]. The equation 2.26 illustrates that the EF is inversely proportional to the initial fluorescence yield. Therefore, the reduced fluorescence QY of the PSI will strongly influence the fluorescence EF at higher temperatures. In contrast, the influence on the fluorescence EF will be weak at cryogenic temperatures. A detailed explaination of the QY effect is given in section 5.4.1.

2.4 Single-Molecule Spectroscopy

The detection of single protein dates back to 1976 when Hirschfeld managed to detect individual immobilized protein molecules labeled with multiple fluorescence labels at room temperature [159]. Later on, in 1989, Moerner and Kador triumphed the first spectral measurement through absorption spectroscopy utilizing doubly modulated absorption techniques at liquid He temperature [160]. In 1990 Michael Orrit and Jacky Bernard were also successful to show the detection of the single molecules from the fluorescence

excitation spectra of a pentacene doped *p*-terphenyl crystal [161]. Since then the SMS approach has achieved tremendous popularity in different natural science fields such as physics, material science, and biology, etc. Utterly new insights into the structure and dynamics of the condensed or living matters have been gained. In this section a brief detail about the challenges needs to meet to performing SMS and the advantages of SMS over ensemble measurements is given.

2.4.1 Challenges in performing SMS

In order to detect a single molecule out of billions to trillions of the solvent or host molecules, a focused optical beam (typically a laser) is used to pump a single molecule and the resultant fluorescence is detected. For successful detection, it must be guaranteed that: (i) only one molecule is in resonance with the optical wavelength in entire laser probed volume, and (ii) for a reasonable averaging time the signal to noise ratio (SNR) from single molecule should be greater than unity [162, 163].

Generally, a molecule is accompanied by neighbouring molecules which also get addressed during the excitation process. So the first challenge is to assure the collection of the fluorescence signals from the molecule of interest only keeping the surrounding matrix undetected. This issue is resolved by using a very low concentration of the molecules of interest and minimising the background signals. A very low temperature and very low linewidth of the laser can also help. The suitable concentration of the target molecules for SMS depends on the technique used for investigation, the sample under investigation, and the temperature of measurements. Therefore, depending on the experimental conditions and requirements a suitable concentration is worked out. For SMS of the photosynthetic pigments, a concentration of $\sim$3 pM was found to meet the required criterion. Avoiding the background signals completely is not possible. The vast multitude of non-fluorescent matrix, unwanted impurities or molecular components of the solvent will still contribute significant background signals. Despite having low fluorescence yield, these impurities can emit a strong residual fluorescence, which

increases rapidly with the energy of incident photons. However, by carefully choosing experimental ingredients like, using ultrapure solvents, nanopure water for sample preparation, and by avoiding working in blue or near UV spectrum part, the background signals can be strongly minimised. The Raman scattering from host and matrix also contribute its part in the background. Since both, the residual fluorescence and Raman scattering, are proportional to the excitation volume of the sample; this contribution can be suppressed by reducing the excitation volume [164]. Various optical designs like a lens or single-mode fiber and microscope objective (MO) are available to minimise the excitation volume to 100 μm^3 and 1 μm^3, respectively. An excitation volume of 10^{-2} μm^3 is possible to reach by the sub-wavelength illumination of a near field optical probe through an aperture [164]. The smaller the detection volume is smaller will be the amount of the background signals [162, 165].

The second challenge is to handle the problem of the weak signals of the target molecule [165]. The issue of the low SNR is dealt by using highly efficient detectors, employing the molecules of large absorption cross section, highest fluorescence quantum efficiency and high photostability, collecting the fluorescence signals over a wide solid angle, minimising the background signals to the lowest possible level, controlling the Raman and Rayleigh scattering at an excitation wavelength (discussed in the previous paragraph), etc., [162, 164]. An absorption cross section of a molecule, which can also be regarded as an "effective area", is an important parameter to characterize its interaction with light. For randomly oriented molecules the absorption cross section is given as [164]:

$$\alpha = 2\pi \left(\frac{\lambda}{2\pi}\right)^2 \left(\frac{\gamma_r}{\Gamma_{tot}}\right) \tag{2.27}$$

whereas, λ, γ_r, and Γ_{tot} are the light wavelength, spontaneous fluorescence rate (radiative) and the total frequency width of absorption [164, 166, 167].

Higher absorption cross section would mean efficient absorption of the incident photons and consequently the maximum emission with minimum background signal.

The emission rate of the molecules also plays a crucial role to achieve strong signals. Higher emission rate will result an easy detection of single molecules. In ideal situation for a two level molecule the emission rate is only limited by the lifetime and is given by $\tau_f^{-1}/2$ [162, 164]. Whereas τ_f is the fluorescence lifetime. For a stronger emitter with $\tau_f \sim 5$ ns the emission rate would be of order 10^8 s^{-1}, which is high enough to have a very intense signal with even a moderate detection efficiency. However, the maximum photon emission rate is often limited by the physical effects like optical saturation of the transition. As the laser power is increased the photon emission rate increases initially until the optical transition is saturated. Once the saturation is reached, the absorption cross section of the molecule will decrease to half. The absorption cross section as a function of the pumping intensity can be given as [162]:

$$\alpha = \frac{\alpha_0}{(1 \ + \ {}^{I}/_{I_s})} \tag{2.28}$$

Where, I is the pumping intensity of the laser and I_s is the characteristic saturation intensity. A further increase in the laser power instead of increasing signal photons will thus increase the background photons. The optical saturation may also arise from the bottleneck effect of the dark states such as triplet state. The intersystem crossing process takes the molecule into a form where both the absorption and emission of the photons ceases leading to a premature saturation. The maximum emission rate reduces to $\tau_f^{-1}/(2 + k_{ISC}\tau_T)$, whereas k_{ISC} is intersystem crossing rate and τ_T is the lifetime of the triplet state [164]. The molecules with strong bottlenecks will experience a strong reduction of their emission rate. Therefore, it is preferred to use the molecules with weak bottleneck effects.

To collect the strong fluorescence signals from the molecules, it is essential to collect as many photons as possible. By applying better collection strategies

like parabolic mirror or MOs with high numerical aperture (NA), the fluorescence over wide solid angles can be collected and resultantly strong single molecule signals are achieved [164]. Additionally, for optical fluorescence spectroscopy the emitted photons are redshifted towards longer wavelengths with respect to the excitation photons. Therefore, a long pass filter is used to suppress the laser. This assists the detection of the signals from single molecules with a reasonable signal to background ratio (SBR) making the fluorescence based technique a method of choice for SMS [164, 165].

2.4.2 Advantages of SMS

The common objective of all the spectroscopy techniques is to acquire information about the molecular structures. The conventional spectroscopic measurements provide only the averaged data obtained from a huge number of molecules, reporting the ensemble features of investigated systems. The ensemble features mask the underlying molecular dynamics and lack the complete detail of molecular properties. The major attraction for SMS lies in the fact that it allows removing the ensemble averaging effects and provides the information of distributions and time trajectories of single observables [168]. Fig. 2.17 shows a comparison of the emission from a single molecule with an ensemble. SMS allows observing an individual molecule of interest concealed deep within a crystal, polymer, or a cell through optical excitation. The individual members of the heterogeneous population are examined one by one and the frequency histogram of the actual distribution values for resultant experimental parameters are constructed. Such distributions provide a wealth of information about molecular heterogeneities and local nanoenvironment of molecule etc. Deep understanding of the behaviours of different molecules because of their inhomogeneities and of same molecules at different times is gained [163, 164].

Another attraction of SMS is its ability to optically sense the internal conformational states of a single molecule and transition between them. At any given time the single molecules exist in the certain solvent environment and conformational states. The measurement of the optical spectra of such

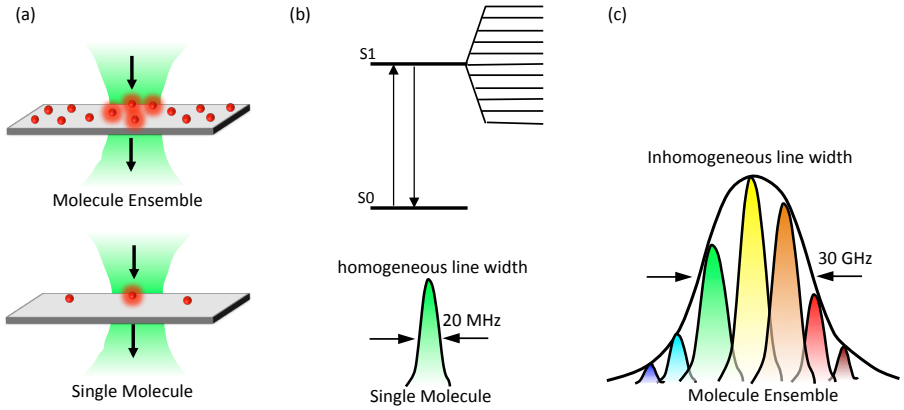

FIGURE 2.17: Schematic representation of the origin of in-homogeneous spectral line broadening at low temperature. (a) A schematic of focused laser beam pumping a single resonant molecule (bottom) and ensemble molecules (top) of the sample. (b) The energy level scheme of single-molecule spectroscopy (SMS) showing electronic ground state, S_0, and the first excited state, S_1. Upon excitation of single resonant molecule, fluorescence is emitted featuring a homogeneously broadened linewidth (shown below the energy level diagram) caused by the excited state lifetime. (c) a situation is sketched when an ensemble of molecules are excited. Since, each of the molecule experiences a slightly different local chemical environment so each molecule will have slightly different molecular transition frequency. As a consequence an in-homogeneously broadened spectral line which is combination of the homogeneous lines of many individual molecules is obtained. The figure is redrawn partly following the Ref: [165].

single molecule helps to learn about the number and identity of the overlapping transitions, together with the underlying conformational heterogeneities which are responsible for the broadening of the spectra in populations of molecules [163]. Additionally, SMS assists the detection of rare fluctuating, flickering or stochastic behaviours of single-molecule systems. Single molecule behaves as a reporter for its immediate local nano-environment [162, 163]. Since the single molecules exist in a particular solvent environment. Any change in local environment or photophysical parameters of the single molecule will lead to a change in the absorption frequency of the molecule. This change in absorption frequency is termed as "spectral diffusion" which may cause the spectral shifts or fluctuations. The data of such fluctuations provide an unusual understanding of the behaviour which is generally masked by ensemble averaging [162]. SMS eradicates the necessity

for synchronization of all subsystems and yields time-resolved information automatically. For standard ensemble measurements where many individual molecules are undergoing a time-dependent process like intersystem crossing events, it is essential to synchronize a large number of molecules to measure the triplet lifetime. At single molecule level, the intersystem crossings which are also termed as "quantum jumps" between electronic states of a single molecule can be observed directly [164, 169], eliminating any demand of synchronization.

Advantages of the Study at Low Temperature: Performing spectroscopy at cryogenic temperatures has a number of advantages over the room temperature. Various mechanisms which are responsible for the broad linewidth and unstructured fluorescence spectra at room temperature can be suppressed by lowering the temperatures. With the increase of temperature the interaction of the exciton (electron) - phonon increases, which leads to a broadening of the fluorescence spectra. In contrast, the spectral lines at cryogenic temperatures become extremely narrow uncoding more information about the molecules themselves, their interactions with light and surrounding matrix, and about the dynamics of the surrounding matrix [164, 170].

The electronic properties of a fluorophore are deduced from its transition energy. The transition energy of each fluorophore is strongly dependent on the local chemical environment of the fluorophore. Based on the matrix wherein the fluorophore is embedded, each individual fluorophore will experience different composition of the environment and accordingly different local chemical environment. As a result, the frequency of the transition for each individual fluorophore will be slightly shifted for both of the excitation and emission. These differences are difficult to distinguish at room temperatures. In contrast, at cryogenic temperatures, it becomes possible to observe separate peaks for individual emitters corresponding to their respective transition frequencies [165].

The linewidth of the fluorescence spectrum at cryogenic temperatures is defined by the lifetime of the excited state. At cryogenic temperatures the inhomogeneous broadening vanishes and the emission spectrum dominates by the sharp lifetime limited spectral lines. Thus, spectroscopy at cryogenic temperatures enables to observe even the discrete vibronic levels of the molecules and offers the opportunity to investigate the individual vibronic levels and subsequently to assign to distinct vibration energies [165, 171]. For better visualization a comparison of the temperature dependent fluorescence spectra of an ensemble of the terylene dye molecules can be found in Ref: [165].

For single molecules in solids, the spectral lines at cryogenic temperatures become extremely narrow. Fig. 2.18 (a) shows the calculated emission profiles of single emitters at different temperatures (figure taken from Ref: [125]). The spectral properties are influenced by the environment which is described by the electron-phonon coupling. The phonons (crystal lattice vibrations) are a part of the wave function of ground state and their population is strongly temperature dependent. At ambient temperature the energy of thermal motion (kT$\sim$ 200 cm^{-1}) is enough to excite an abundance of phonons resulting a strongly increased inhomogeneous line width [172]. By lowering the temperature, the thermal energy and consequently the number of phonons is reduced. As a result, the electronic transition appears to occur without the involvement of the phonons. Such transitions are named as zero-phonon transitions. The resultant emission spectrum of the single emitter, thus, comprises of an intense and narrow line termed as a zero-phonon line (ZPL) and a broad phonon wing (PW) redshifted to ZPL (Fig. 2.18 (b)) [125, 165, 172]. The PW is caused by the interactions of the chromophore with its surrounding [165, 173]. The intensity of the optical band profile can be given as:

$$I(\nu, T) = I_{ZPL}(\nu, T) + I_{PW}(\nu, T) \tag{2.29}$$

By determining the relative intensities of ZPL (I_{ZPL}) and PW (I_{PW}) from the emission profile of single emitter, the Huang-Reys factor S, which gives

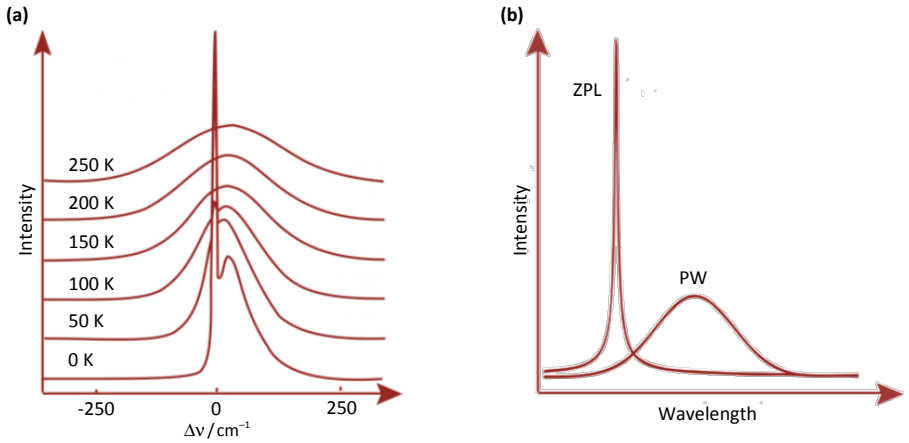

FIGURE 2.18: (a) Temperature dependent emission profile of single molecules calculated for Huang-Rhys factor S = 1 and phonon mode energy ω_{ph}=15 cm^{-1}. With the decrease of temperature the specific substructures arises. (b) Schematic representation of the contributions to emission spectrum of a protein-bound pigment at low temperature. Besides a narrow zero-phonon line a phonon wind (PW) on the low energy side of the ZPL also appears. The figure is taken from Ref: [125].

the microscopic details of the vibrational coupling can be calculated as [165]:

$$\alpha(T) = \frac{I_{ZPL}}{I_{ZPL} + I_{PW}} = e^{-S(T)} \tag{2.30}$$

At higher temperatures, the value of S(T) increases so the intensity of ZPLs decreases. In contrast, at a lower temperature the strength of electron-phonon coupling weakens and therefore the value of S(T) decreases and sharp ZPLs appear. For the values of S $\leq$ 0.7 the electron-phonon coupling is considered weak, which results in needlelike ZPLs in emission spectra [165]. The ZPLs provides the environment defined characteristics of the single molecules [172]. Due to line narrowing even the distinct vibronic levels of the molecules becomes accessible and consequently the vibronic studies become possible using fluorescence spectroscopy [165]. Therefore, by studying the single molecules at cryogenic temperatures a substantial information about molecules, their interaction with light, interaction with the matrix and about the dynamics of the matrix is obtained [164].

Photobleaching, a phenomenon where the fluorescence emission of the fluorophores starts fading during the measurements because of the photochemical modifications, have also been found to be temperature dependent [174–176]. Under ambient conditions, the molecules in their excited singlet or triplet state undergo the photochemical reaction which irreversibly alters their chemical structure [164, 176]. The mechanism of photobleaching phenomena is although poorly understood, but the photodynamic interaction between excited fluorophores and molecular oxygen (O_2) in its triplet ground state is considered the main reason for photobleaching [176]. Protection of dyes from chemical reactant such as molecular oxygen leads to a reduced photobleaching [177, 178] as it happens in GFP naturally [177, 179]. Other than molecular oxygen, water or water like environment, matrix molecules, impurities and excitation power also contribute in photobleaching [175, 176]. Working under ambient conditions significantly increases the efficiency of photobleaching. As more photobleaching pathways and photodecomposition channels become activated [176]. On the contrary, at cryogenic temperature the small reactive molecules like oxygen, water or other impurities are frozen and cannot diffuse. Additionally, the photodecomposition channels are also suppressed. Thus, lowering the temperature will reduce the photobleaching drastically, as fluorescence will only be limited to sudden conformational changes of host-guest system [164, 176]. The Raman scattering by the host matrix or solvent molecules at cryogenic temperatures is also negligible compared to room temperature, where it becomes comparable to the absorption cross section of the single molecule [164]. Weak Raman scattering leaves a reduced background signals, adding another credit in the account of cryogenic temperatures.

Advantages of the Study at Room Temperature: Despite the fact that studies at cryogenic temperatures provided fascinating insights of the molecular world by unraveling the detail of the phenomena which never have been observed before. A number of factors such as high cost of cryogenic measurement and frozen molecular dynamic processes, etc., limit the use

of cryogenic spectroscopy leaving many aspects unexplored [165]. As performing spectroscopy at cryogenic temperatures is highly challenging and it demands highly expensive setups which are not available frequently. Therefore, only a few laboratories have the facility to investigate those scientific inquiries which involve the temperatures of few kelvins. Thus, a limited access to such well-equipped laboratories limits the applications of SMS. Additionally, at cryogenic temperatures the molecular dynamic processes like molecular diffusion or molecular foldings, which are essential for investigations in life science fields gets frozen. As a result, the investigations about conformational states, conformational dynamics, and activities of individual biological molecules are restricted to SMS at ambient temperatures, only [168].

The simplicity of the experiments and a large number of problems of biological sciences, physics, and chemistry, potentially solvable at room temperatures only, were the driving forces which lead Betiz *et al.*, in 1993 to perform first extended observations of single molecules at room temperature [164, 180]. The gains of SMS at ambient conditions allows to solve a range of difficult problems in physical chemistry like adsorption or desorption of molecules, dynamics in complex environments, surface enhanced Raman scatterings etc.

Tons of information also have been achieved for biological systems by carefully analyzing each aspect such as: position, time dependence, polarization and spectral content of the photons emitted from single molecule. By following the motion of single fluorescent molecules with time, the two-dimensional diffusional path of labelled phospholipids in membranes has been analyzed [181]. The study of the polarization response of single molecules provides the information about spectral jumps, the transition to dark states, and orientational effects, which can be used to deduce information about the conformational changes of nearby proteins [182, 183]. The time dependence of the emission provides a bunch of additional information, for example: on nanosecond time scales about the emission lifetime by using time-correlated

single-photon-counting method [184], while on longer time scales about intersystem crossing dynamics, fluctuations in local configurations and environments, chemical changes and last but not the least about diffusions, etc., [164, 185, 186]. Information about the colocalization, folding and conformational dynamics of proteins, interaction among individual biomolecules, sequencing of single DNA molecules and mechanisms of molecular motors [164, 178, 187–189] became accessible at room temperatures which were impassable at cryogenic temperatures.

3

Materials and Methods

This chapter gives a detailed overview of the methods used for fabrication of the NPs, and techniques employed for the characterization and analysis during the thesis. A detailed description of the home-built confocal setup for measurements at different temperatures (1.6 - 250 K) and preparation of the bio-nanohybrids is given. The specificities of the microscope and the working principle are demonstrated.

3.1 Characterization and Analysis Techniques

3.1.1 Single-Molecule Spectroscopy

3.1.1.1 Optical Setup

A home-built setup of the confocal microscope, designed for SMS at cryogenic temperatures (1.4 K) was used for the experiments during this study. The setup was originally built by Dr. Martin Hussels as a part of his Ph.D. project work and is described comprehensively elsewhere [79, 190]. The whole microscope setup, comprised of multiple components together with bath cryostat (SVT-200, Janis) is mounted on a damped optical table (OPTA GmbH, Bensheim, Germany). The detailed scheme of the experimental setup is depicted in Fig. 3.1. A fiber-coupled continuous wave (*cw*) diode laser (iBEAM-660-3v2, TOPTICA Photonics, Gräfelfing (Germany)) of wavelength 665 nm has been used as an excitation light source. At the end of the fiber, it is coupled to an output coupler (60SMS-1-4-A11-02, Schäfter+Kirchhoff GmbH, Hamburg (Germany)) which consists of the internal lens focusing mechanism and results in a collimated laser beam. To suppress the side bands of the laser, the collimated laser beam is passed through a band pass cleanup filter (single band, FF01-660/13-25, $T_{ave} > 93$ %, Semrock), which only permits to pass the light in a specific range (653.5 - 666.5 nm). The cleaned laser beam is further redirected by a beam splitter, BS (ZQ 670 RDC, AHF Analysentechnik) and two fixed, adjustable mirrors (Max Mirror (F29-001), $\lambda/10$, R (350-1100 nm) >98 %, AHF Analysentechnik) towards the MO mounted inside the bath cryostat. The fixed, adjustable mirror in front of bath cryostat guide the collimated laser beam into the back aperture of the MO (60X, N.A. = 0.85 (unless otherwise noted), Mikrothek GmbH, Hamburg (Germany)) through the windows of the cryostat. The diameter of the laser beam is assured to fill the back aperture of the MO. The sample is mounted on the sample holder and is transferred to the mounting element on the scanning stage with the help of transfer line. The sample holder gets attached to the scanning stage through

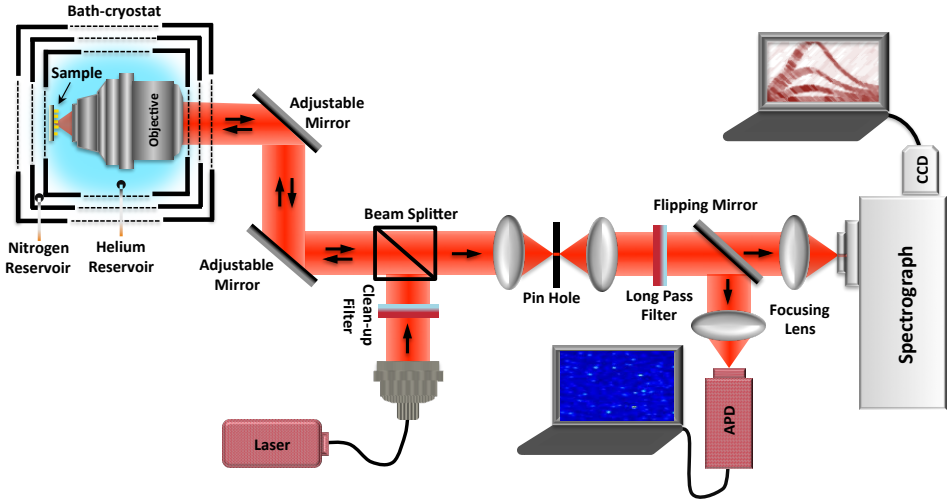

FIGURE 3.1: Sketch of the experimental home-built confocal single-molecule setup, designed for the measurements at cryogenic temperature (1.4 K) with description about the optical components. Detailed explanation of the setup is given in the text. Briefly, a collimated laser beam after passing through multipal optical components is deflected into the MO. The fluorescence signals emitting from the sample are collected back from the same MO, pass the pinhole to reach either of the detectors (APD or CCD camera) and the fluorescence images and spectral data are acquired. The whole setup is controlled by self written LabView program.

the magnets (NdFeB, Magnets4you GmbH, Germany) in such a ways that the sample is directly in front of MO. A detailed description of the sample transfer mechanism can be found in Ref: [190]. During the measurements, both the MO and the sample are situated inside the bath cryostat filled with liquid helium. To perform the measurements, a sample scanning approach instead of laser scanning was adopted to escape any complications in retaining the alignment and throughput, which may arise due to scanning the laser. The sample is positioned and scanned in a fixed range of xy-plane by using linear stage and scanners (Attocube Systems, Germany) keeping the MO static. The fluorescence emission was collected back from the same MO and guided to the BS following the path of the excitation beam. After transmitting through the BS, the fluorescence emission is imaged by a lens onto the pinhole (ϕ = 30 μM, Thor Lab), where only the fluorescence emission light coming from the focal volume of the laser is passed through

while all the out-of-focus light gets blocked. The size of the pinhole is chosen very carefully to maximise the accumulation from illuminated region and simultaneously eliminating the unwanted background light. The light coming from the laser focal volume is then collimated by a lens positioned after the pinhole before it passes through a long pass filter (HQ680LP or HQ695LP, AHF analysentechnik) which allows only the precise fluorescent emission to pass through while filtering out any stray signals. A computer controlled flip mirror lying in the beam path offers the choice to switch between the avalanche photodiode, APD (COUNT-100C, Laser Components GmbH, Olching, Germany) and spectrograph (Shamrock 500i, A-SR-500i-B2-SIL, L.O.T. Oriel GmbH, Darmstadt, Germany) combined with a CCD camera (SR-500i-B2-SIL, CCD12126, Andor Technology) at the output slit. When the mirror is flipped in the beam path, it redirects the detected fluorescence signals onto the focusing lens to focus it on the detection spot in the centre of single photon sensitive APD detector. The whole setup is controlled by self-written LabView program developed by Dr. Alexander Konrad as a part of his Ph.D. project. The lens is chosen with precise focal length to fit the size of their focus to the APD chip. Through raster scan of the sample a fluorescence image is collected. By flipping the mirror out of the beam path, the fluorescence signal is focused with the help of a lens to the entrance slit of the spectrograph. The spectrograph is equipped with two reflection gratings of 200 and 400 lines/mm, respectively, providing different spectral resolution. The fluorescence signals get split into its component wavelengths by the spectrograph and subsequently are focused on the CCD camera for spectral data acquisition.

3.1.1.2 Cryogenic Setup

The simplified drawing of the interior of bath cryostat with a brief detail about the major associated parts is shown in Fig. 3.2. The bath cryostat from the Janis research company (Model: SVT-200-5, USA) was used to perform the experiments during the presented project work in the temperature range 1.6 to 250 K. The major parts include: liquid helium (LHe) and

liquid nitrogen (LN_2) reservoirs, surrounded by multilayer super insulation, evacuation valves, helium/N_2 fill and vent tubes and safety pressure relief valves etc. The MO, piezo modules, linear stages, temperature sensor and mounting plate etc., all are housed at the bottom of the sample tube in a stainless steel cage.

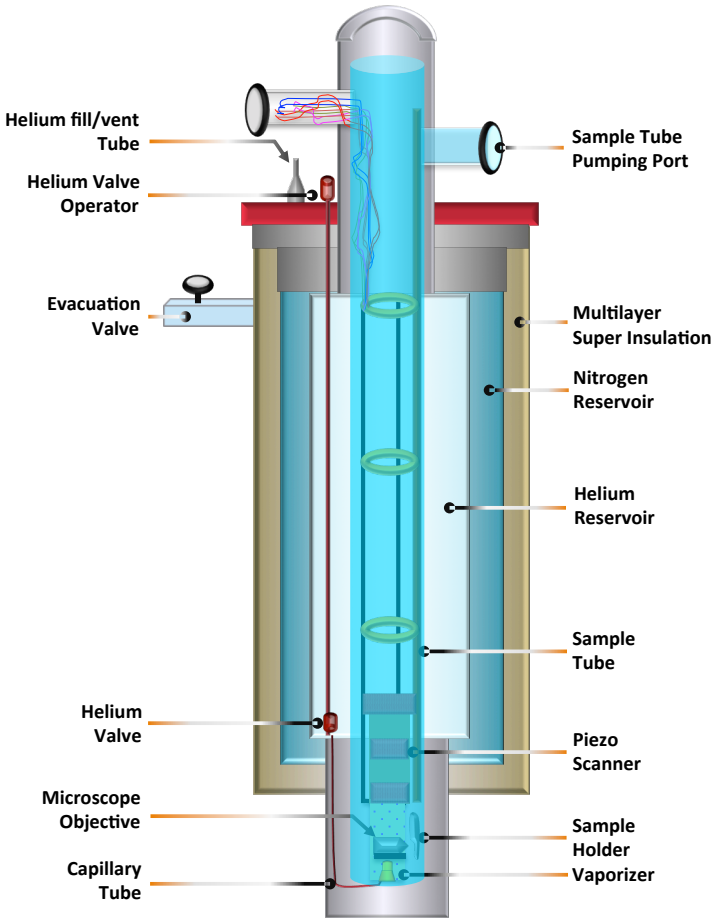

FIGURE 3.2: Simplified drawing of the interior of bath cryostat with major parts labeled.

The vacuum jacket surrounding the LHe and LN_2 reservoirs to reduce the cryogen consumption rate is pumped out by using an oil pump (Leroy Somer, France) and a turbomolecular pump (PFEIFFER Vacuum) to reach the vacuum level 5×10^{-5} mbar. The cryostat is pre-cooled to ~100 K by filling the liquid nitrogen reservoir with liquid nitrogen (LN_2) a night before the measurements. When it's ready, the LHe from the pressurized LHe container is transferred to the LHe reservoir. Helium valve at the bottom of the reservoir allows the LHe by passing through a small capillary tube and vaporizer to

reach the sample area. The LHe collects inside the sample area and under normal conditions cool it down to 4.2 K. At this temperature the LHe keeps on bubbling in the beam path which makes it impossible to perform optical measurements. Therefore, the temperature must be reduced below 2.2 K, to reach the superfluid state of helium where stable measurement becomes conceivable. This is achieved by reducing the pressure in the sample tube. The gases helium from the sample tube is pumped out by using a rotary vane pump and a temperature of typically about 1.6 K is reached. During pumping process, the LHe from reservoir keeps on flowing continuously into the sample chamber through the capillary. The actual temperature close to the sample is monitored by a temperature controller (Model 336, LakeShore) equipped with a Cernox sensor (CX-1030-SD-HT 0.3L).

3.1.1.3 Sample Preparation

The main steps involved for PSI sample preparation to perform SMS are illustrated in Fig. 3.3. A highly concentrated sample (Chl concentration∼3 mM) of purified PSI trimers from *T. elongatus* (procedure described in Ref: [191]), provided by the PD Dr. Eberhard Schlodder (Technical University of Berlin, Germany) was stepwise diluted in a pH 7.5 Tricine buffer solution to reach the required concentration for SMS. The buffer solution contains 20 mM

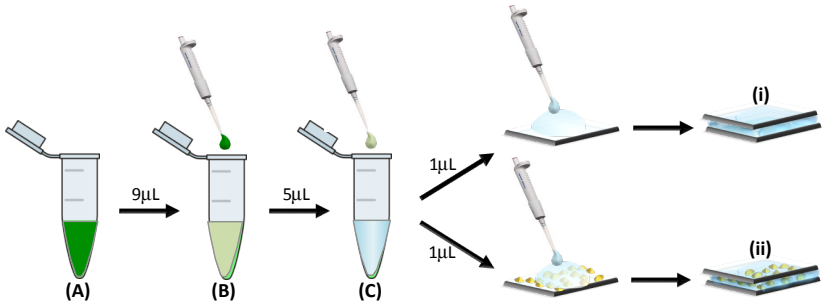

FIGURE 3.3: Steps involved in the preparation of sample for SMS. Purified PSI trimers sample is diluted to a concentration of 3 pM through multiple dilution steps in a Tricine buffer solution (detail is given in description). 1μl of this highly diluted sample solution is sandwiched between (i) two glass coverslips to prepare control PSI sample and (ii) between nanostructure substrate and glass coverslip to prepare a hybrid sample. Subsequently the samples are transferred to pre-cooled cryostat to perform SMS, respectively.

Tricine, 25 mM $MgCl_2$, 4 mM ß-DM and 5 mM sodium ascorbate (Na-ascorbate). The ß-DM helps to avoid PSI aggregation while Na-ascorbate is used for the pre-reduction of P700. In the first step, 250 μL of the Tricine buffer solution was added in each of the three 1.5 mL Eppendorf tubes (named A, B, C in Fig. 3.3). 1 μL of the purified and concentrated PSI solution was added to first buffer filled Eppendorf tube (A). In the following step, 9 μL of this diluted solution from Eppendorf tube (A) was added to Eppendorf tube (B) which further diluted the concentration of PSI trimers in solution. To finally achieve the desired concentration for SMS (approximately 3 pM), 5 μL of the diluted PSI solution from Eppendorf tube (B) was added to Eppendorf tube (C). Lastly, 1 μL of this highly diluted solution was sandwiched between (i) two glass coverslips of dimensions 4.0×4.0×0.2 mm to prepare control PSI samples and (ii) bare glass coverslip and the metallic nanostructured substrate to prepare a bio-nanohybrid. Subsequently, to perform SMS measurements the samples were transferred into a pre-cooled cryostat (T= 4.2 K). For bio-nanohybrid, the glass coverslip faces the incident beam while the nanostructured substrate was on the backside with respect to the excitation beam.

3.1.2 Scanning Electron Microscopy

Scanning electron microscopy (SEM) is a powerful tool used for the observation, characterization, imaging and dimensional measurements of the micro- and nanoparticles [192]. Due to their diffraction limited resolution (∼200 nm), the light microscopes are not very useful at the nanoscale. Electron microscopes, on the other hand, use highly energetic electron beam instead of light, allowing the observation and characterization at a resolution down to $<$ 10 nm [193]. The working principle of SEM is displayed in Fig. 3.4. A high intensity and finely focused electron beam is directed toward the sample. The electron beam can either be scanned in a raster scan pattern across the surface of the sample to form an image or static to analyse at one position. When the incident electrons which are also known as a primary electrons interact with the surface of the sample, it emits the

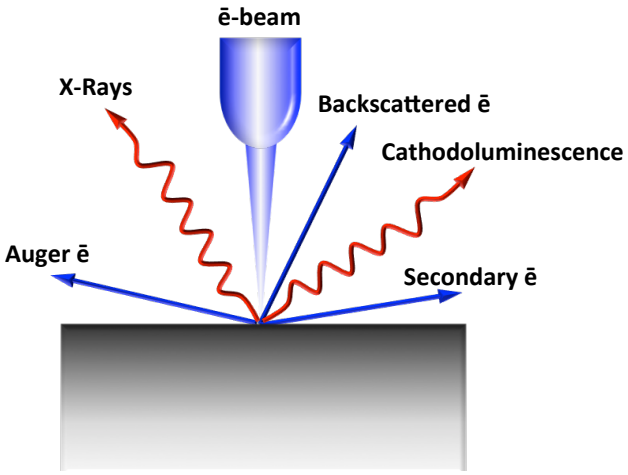

FIGURE 3.4: Schematic representation of mechanism of SEM. A highly focused electron beam is scanned over the surface of the sample and the emitted electron on incident side are used to deduce the information about the accurate size of the NPs and exterior morphology of the surfaces.

secondary electrons (SE), backscattered electrons, Auger electrons, characteristic X-rays and cathodoluminescence from the interaction volume [193, 194]. Various detectors are used to detect these emitted electrons or photons to deduce information about the topography and composition of the surface of the sample. For imaging purposes, secondary and backscattered electrons are of greatest interest because their emission is highly dependent on surface topography. Secondary electron imaging (SEI) is the standard mode of imaging in the SEM, where SEs are detected and images are constructed by mapping the detected signals. The emission of SEs is confined to a very small volume emitting from very close to the surface of the sample, therefore, they yield high-resolution images [193]. Backscattered electrons, on the contrary, originate from a deeper location within the sample, yielding the images of relatively poor resolution than SEI. The analysis of characteristic X-rays, however, provides the qualitative and quantitative analysis of elemental composition in the irradiated region of sample [193, 194]. During this study, a conventional SEM (Philips XL 30) facility available at Prof. Dr. Monika Fleischer group (University of Tübingen) was used to inspect the accurate sizes of the NPs and the morphology of the surfaces.

3.1.3 Helium Ion Microscopy

SEM has been historically the technique of choice to acquire ultrahigh resolution images in the field of nano-materials and nano-biology [195]. It has long been used as a fundamental tool to study samples exterior morphology, structure, composition and other properties like electrical conductivity etc., [194, 196]. However, SEM suffers from several challenges, e.g., limited image resolution, diffraction and chromatic aberration limited probe size, loosing minute surface details due to heavy metal coating and the charging effects of insulating samples etc., which limit its performance [196–198]. Helium ion (He-Ion) microscopy presents a tool which not only unites many of the advantages of SEM but also overcomes some of its deficiencies. The working principle and applications of He-Ion microscope are nearly similar to traditional SEM with distinctly different source technology, contrast mechanism and the sample interaction [198]. A three-sided pyramidal tip with only three atoms at the apex acts as a He-Ion source [196, 197]. When a high voltage (30 kV) is applied to the cryogenically cooled pyramidal tip, an electric field strength of few V/Å is achieved at those apex atoms [196, 198]. When Helium gas is admitted in the vicinity of the tip, it gets ionized by the electron tunnelling process. As a result, each of the three apex atoms appears to generate ion emission, of which one is chosen for imaging [196, 198]. The schematic illustration of the He-Ion microscope is shown in Fig. 3.5. Inset is displayed the ionisation process. The extracted ions in the same way as in SEM, are accelerated, collimated, focused and scanned in raster scan pattern across the surface of the sample. Due to the ultra high source brightness and very small de Broglie wavelength of He-Ions the spherical, chromatic and diffraction aberrations become insignificant and the ion beam can be focused to a smaller probe size on the sample [196, 198, 200]. As a result, the ultimate resolution of He-Ion microscope improves substantially to ∼0.25 nm [195]. Also, the yield of SE generated by He-Ions increases largely. Compared to one SE produced in SEM by each incoming primary electron, each incoming He-Ion typically generates 2 to 8 SEs [196,

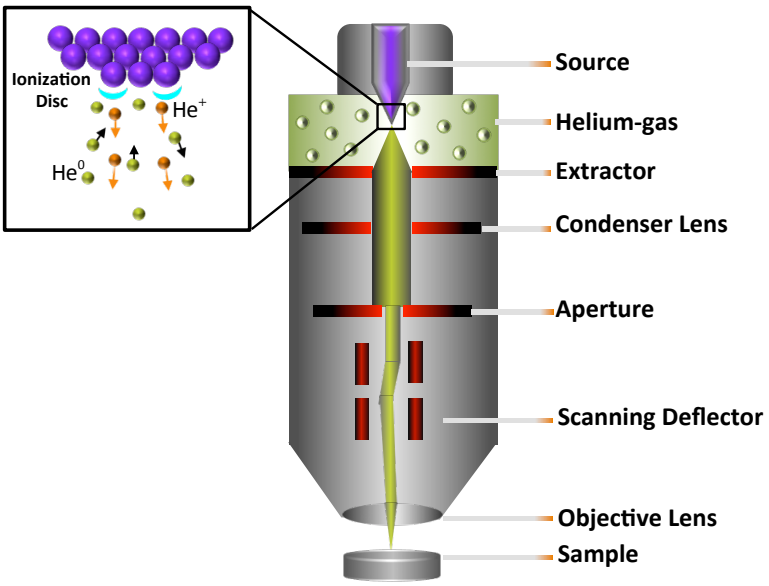

FIGURE 3.5: Schematic illustration of the scanning He-ion microscope column, showing the ion source, ion-beam path, condenser lens and aperture etc. Top inset shows an image of He-Ion source shaped to a three sided pyramidal tip with only three atoms at the apex. Due to the polarisation effect, neutral helium atoms (He^0) are drawn toward the apex and after ionisation the extracted ions are accelerated in the form of a beam and raster scanned on the sample. The figure is adapted from the Ref: [197, 199]

.

201]. This abundance of SEs yields a very high contrast image. Another advantage of helium ion microscopy (HIM) includes minimizing beam induced surface damage. As the forward scattered ions penetrate deeper into the sample, therefore, the propensity for beam induced surface damage reduces [196]. HIM images of SAMs were recorded in cooperation with Carl Zeiss AG, USA.

3.1.4 X-Ray Photoelectron Spectroscopy

X-ray photoelectron spectroscopy (XPS) is a surface analysis technique used to identify and quantify the elemental composition of the material under analysis [202]. This technique has been increasingly used for the quantitative investigation of the surface films formed by self-assembly of alkanethiols on gold [203, 204]. An overview of the working principle of XPS based on the photoelectric effect redrawn from the Ref: [205] is displayed schematically in

Fig. 3.6. An incident X-ray photon of energy hν penetrates the surface of the material, resulting in the ejection of a core-level electron from its bound state. The process of photo-ionisation takes place in four steps: (i) absorption of incident photon, (ii) ejection of a core-level electron, (iii) displacement of the ejected electron inside the material, and (iv) emission of electron out of the surface into the vacuum of the spectrometer [206]. The energy and intensity of the photoelectrons are analysed to identify and quantify the elements present in the sample. The electron spectrometer measures the

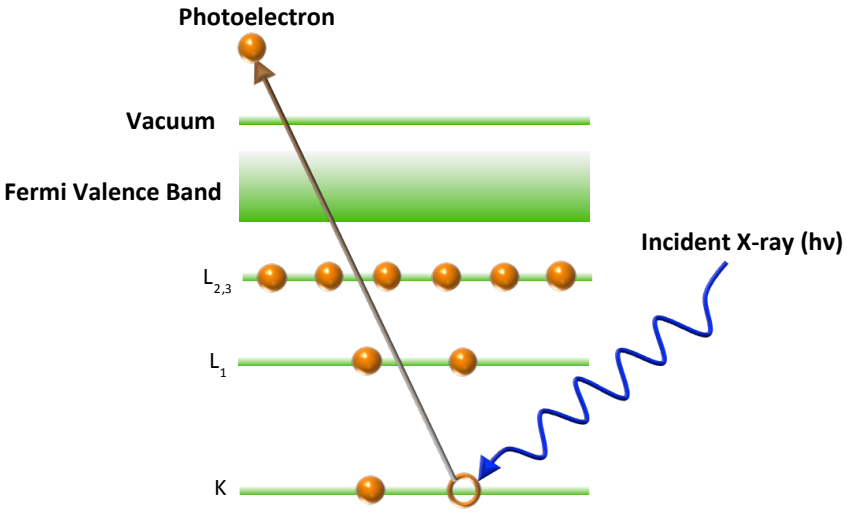

FIGURE 3.6: Simplified schematic of the working principle of XPS. Photoionization of an atom results the emission of a core electron to produce a photoelectron. The energy of the emitted photoelectrons is analysed by electron spectrometer to identify the elements and quantify the chemical composition.

kinetic energy (E_K) of the emitted photoelectrons which is not an intrinsic material property as it is dependent on the incident photon energy [205]. The binding energy (E_B) of the characteristic core electrons of each element is therefore used as a reference parameter to identify the electron, specifically in term of atomic energy level and parent element [205, 206]. Therefore, the E_B of the photoelectrons is determined by using the equation 3.1:

$$E_B = h\nu - E_K - \phi \tag{3.1}$$

whereas hν is the energy of the incident X-ray photon, E_K is the measured kinetic energy of the emitted electron and ϕ is work function of the spectrometer. E_B is then used for identification and quantification of the surface elements. The XPS measurements were performed using a standard source with twin anodes (Al Kα and Mg Kα excitation 1486.6 eV and 1253.6 eV) in a multi-chamber ultra-high vacuum (UHV) system (base pressure $\sim 1 \times 10^{-10}$ mbar) equipped with a Phoibos 100 hemispherical analyzer (SPECS). The measurements were performed together with Ph.D. student Mathias Glaser at Prof. Dr. Thomas Chasse group (University of Tübingen).

3.1.5 Contact Angle Measurements

Contact angle measurement is a useful tool used for the characterisation of SAMs. It renders an excellent way to spot the presence of respective thiol monolayer on the surface of the substrate by providing information about wettability of the surface [207]. The monolayers of different thiols have different wettability and, therefore, different contact angles [208, 209]. Contact angle depends on the liquid of choice used for the investigation [208]. For water, if the contact angle is $0° < \theta < 90°$, the liquid will wet the surface which may also be termed as a hydrophilic, while, for $\theta > 90°$ the surface will be non-wettable termed as hydrophobic [207, 210]. The contact angle is

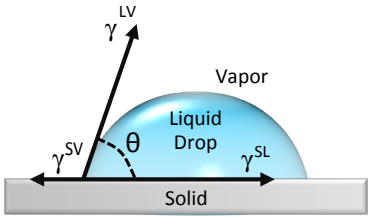

FIGURE 3.7: A liquid droplet on the surface of metalized substrate.

the angle formed between the liquid/vapor interface (tangent line) and the solid/liquid interface (solid surface) measured by placing a drop of water on the surface of the substrate, as shown in Fig. 3.7. When a droplet of pure liquid is placed on the solid surface, it experiences intermolecular adhesion and cohesion forces. The adhesion forces, i.e., the attractive forces between

dissimilar molecules, acts between liquid and solid surface, promoting the spreading of the water droplet. The cohesion forces, on the other hand, exist between like molecules of the same substance and resists the spread. The balance between these cohesion and adhesion forces described by the Young's equation determines the contact angle (θ) [207].

$$\gamma^{SV} - \gamma^{SL} = \gamma^{LV} \cos\theta \tag{3.2}$$

The Young's equation relates the contact angle to the three surface tensions, including: at the interface of the liquid and vapor phases (γ^{LV}), solid and liquid phases (γ^{SL}) and solid and vapor phase (γ^{SV}) as depicted by Eq. 3.2. The contact angle was measured by using the simple experimental apparatus including a digital camera and drop analysis application of imageJ software. The main steps involved in the measurement of contact angle are as explained. The metalized substrate with SAM of thiol is first cleaned thoroughly with methanol and dried with the stream of N_2. The substrate is then laid down on the plane platform and a drop of deionized water is deposited on it. Focusing a high precision digital camera (Olympus E-420) the image of the neatest drop is collected. The image file is transferred to a computer and by using drop analysis plugin of imageJ software the contact angle is measured.

3.1.6 Confocal Laser Scanning Microscopy

Confocal laser scanning microscopy (CLSM) has become an essential tool for research in biology, biophysics, materials and biomedical science etc. [211–213]. It has added benefits of better contrast and resolution over conventional wide-field fluorescence microscopy [214]. In a conventional fluorescence microscope, the entire specimen is evenly illuminated by an excitation source and resulting fluorescence emission, not only from the objective focal plane but also from points above and below the focal plane is detected by the photodetector [215]. The image of the specimen ,therefore, is occupied by $\sim 90\%$ out-of-focus fluorescence obscuring the in-focus detail [214]. As a

result, the image appears blurry with poor contrast. CLSM on the contrary, provides a powerful mean to create a high contrast and very sharp fluorescence images of a specimen by eliminating the background signals caused by out- of-focus light [216]. The working principle of the CLSM has been displayed in Fig. 3.8. The excitation light is reflected by the dichroic mirror

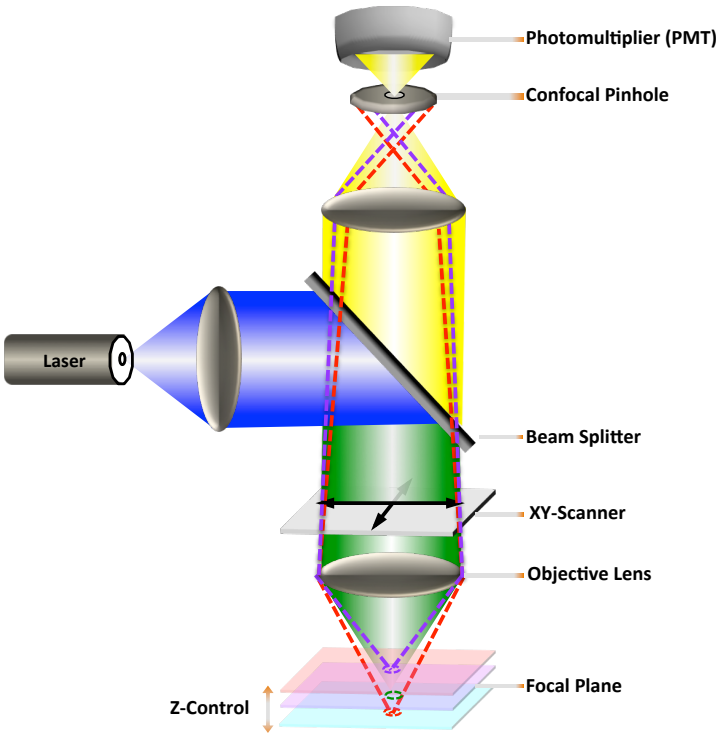

FIGURE 3.8: Illustration of the principle of confocal laser scanning microscope. After reflection from BS (dichroic mirror), the laser light is focused on the sample through objective. The fluorescence is collected with same objective and detected by photomultiplier. The out of focus light is blocked by the confocal pinhole. Only the light from the image plane is detected by the photomultiplier. Figure is re-drawn from Ref: [217].

to evenly illuminates the back focal plane of the microscope objective, which then focuses it into the specimen. Both, the focal spot as well as the areas of specimen above and below are illuminated. However, the illumination is most intense at the focal spot [215, 216]. The fluorescence light emitted from the illuminated spot is collected by the same objective and is focused on the pinhole by a lens placed between dichroic mirror and pinhole. The light coming only from the focal spot passes through the pinhole and all the out-of-focus light (coming from the areas above and below the focus) gets

blocked. In this way, the contribution of all unwanted light is removed. Just in-focus light comes to the detector which yields a high contrast, sharp image with more detail of the specimen, which otherwise is not possible due to out-of-focus light [217]. Excluding most of the out-of-focus light by using a properly adjusted pinhole is the principle advantage of confocal microscopy [215]. Apart from achieving high contrast images with fine detail, it is possible to reconstruct a 3D image by assembling a series of images acquired at several depths in XY-plane, by using an image analysis software [212, 216]. Another advantage of CLSM over conventional microscopy is its ability to improve the resolving power of a microscope. By carefully adjusting the pinhole size, it is possible to improve marginally both the axial and lateral optical resolutions at the cost of significantly reduced signals [211, 214, 215]. A confocal fluorescent microscopy (CLSM Leica SP2 AOBS) facility available at Dr. York-Dieter Stierhof group (Centre for Molecular Biology of Plants, University of Tübingen) was used for imaging the patterned surfaces with site-specific protein bindings.

3.2 Nano-fabrication Techniques

In this section, the nano-fabrication techniques used for the fabrication of the metallic NPs investigated during the studies have been discussed. It consists of two parts: (i) thermal annealing process and (ii) nanosphere lithography.

3.2.1 Thermal Annealing Process

During this thesis, we have investigated different mono and bimetallic NPs of different metallic compositions. Monometallic NPs were composed of Au only, while bimetallic NPs had different composition and order of the Ag or Au layers. Multiple protocols have been introduced over last decades to fabricate the metallic NPs of controlled sizes and shapes, etc., [218–220]. The thermal annealing approach is one of the easiest ways to produce relatively cost and time effective, reproducible and potentially large scale substrates [146, 221, 222]. Additionally, this approach also provides an opportunity to

control the surface morphology i.e., particle size, shape and inter-particle spacing by controlling the key experimental parameters, such as nominative film thickness, evaporation rate, pressure, annealing temperature and time etc., [221]. The steps of the process involved in the fabrication of monometallic NPs are outlined in Fig. 3.9. Thin commercial glass coverslips

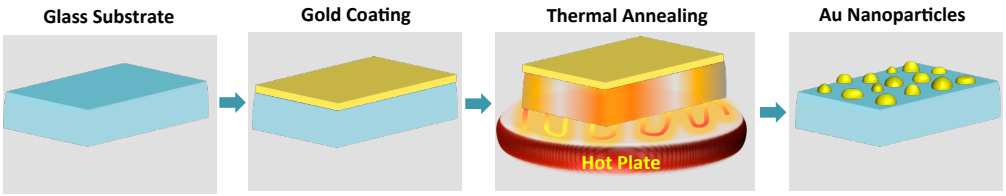

FIGURE 3.9: Schematic of the process steps involved in the fabrication of AuNPs by using thermal annealing technique. After coating a thin gold film by physical vapour deposition method, the thermal treatment is carried out which results NPs of different shapes and sizes.

of the dimensions 22 x 22 mm with a thickness of 0.13 mm were used as substrates for gold film deposition. Prior to gold evaporation, the coverslips were precleaned in an ultrasonication water bath with a mixture of detergent (decon90) and double-distilled water (1:9, v/v ratio) for 20 minutes at 50 °C. To ensure the removal of any detergent residues the coverslips were again rinsed twice with double-distilled water and dried under an N_2 stream.

In the second step, the cleaned coverslips were transferred to the vacuum evaporator (Plassys MEB 400, France) where the metal evaporation process was conducted using the Joule effect mode. The evaporation rate was adjusted to 3 $Å \cdot s^{-1}$ and a built-in quartz crystal sensor was used to monitor the film thickness. The metal evaporation was performed at ambient temperature, under a high vacuum pressure 1.0 $\times$ 10^{-6} Torr. Different samples with respective nominated film thicknesses were fabricated. In the final step, the coated glass coverslips were transferred to a hot plate for thermal annealing operation. The thermal treatment for different samples was carried out at different annealing temperatures for different time periods. The specific information about the fabrication parameters (e.g., film thickness, annealing temperature or annealing timing etc.) for a specific sample is given in the respective chapter.

To fabricate the bimetallic NPs, further evaporations of the respective thin metal films with desired film thicknesses were performed after the thermal annealing step. The detailed description about the fabrication of bimetallic NPs is given in sections 4.2.

3.2.2 Nanosphere Lithography

Nanosphere lithography (NSL) offers another promising approach to fabricate inexpensive, homogeneous, well-ordered and periodic arrays of nanostructures with high-throughput [223, 224]. This method allows to tune the size, shape and interparticle spacing by adequate choice of nanosphere diameter or thickness of the deposited metal film [224, 225]. NSL technique consists of several steps displayed in Fig. 3.10. Commercially available (carboxyl modified) polystyrene nanospheres (PS) of diameter 500 nm were purchased from Microparticles GmbH. Prior to use, the concentration of the aqueous suspension was increased to 10 % from the original 2.5 %, by controlled evaporation.

To perform the self-assembly of PS nanosphere, a Petri dish was specially designed with a small hole drilled on one side to facilitate the removal of water without disturbing the monolayer of nanospheres. A glass coverslip and microscope coverslide were pre-treated with a piranha solution to enhance their hydrophilic nature. The Petri dish was filled with water and glass coverslip was placed at the bottom of the Petri dish. The microscope slide was positioned at some angle for smooth dripping of PS nanosphere suspension. By dropping the suspension of the nanospheres drop by drop, a SAM of nanospheres on the surface of the water was formed. The formation of the monolayer can be identified by uniform colors on the surface of the water. The water was then slowly drained through the hole drilled on the side and the monolayer of nanospheres was transferred on the coverslip at the bottom of the Petri dish. The glass coverslip was allowed to dry before coating it with an adhesive titanium layer and a gold layer of required thickness. The subsequent lift off of the nanosphere monolayer in toluene or by stripping

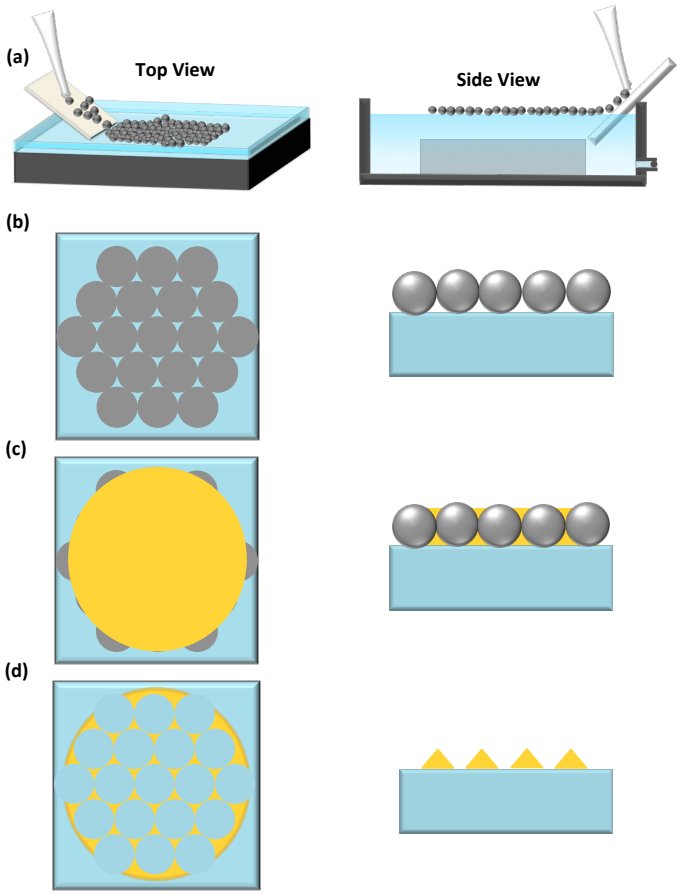

FIGURE 3.10: Schematic diagram showing the steps involved in fabrication of gold triangle arrays by using nanosphere lithography technique. On the left is displayed the top while on the right is the side view of the steps involved. (a) formation of monolayer of polystyrene (PS) nanospheres, (b) monolayer transfered to cleaned glass coverslip (c) coating with chromium and gold, respectively and (d) removing the spheres to achieve final gold triangle arrays.

with scotch tape leaves well-ordered, periodic arrays of gold triangles on the surface of the glass coverslip.

3.3 Materials

In the following Table 3.1, a list of all the chemicals which were used during the study is displayed. Most of the chemicals were purchased from Sigma-Aldrich GmbH with highest available purity grade. Some others were bought from VWR and Merck GmbH. TransFluoSpheres used as a standard calibration sample were purchased from Life Technologies GmbH. The polystyrene

nanospheres employed for nanosphere lithography were purchased from Microparticles GmbH. The small glass coverslips of thickness 200 μm and size 4×4 mm needed for cryogenic measurements were bought from Quartzglas Komponenten und Service QCS GmbH (Germany), while the larger glass coverslips (22×22 mm) used for fabrication of NPs and preparation of SAMs were purchased from Menzel-Gläser (Germany).

Table 3.1: List of all the chemicals used during the study

Chemicals	**Brand**	**Linear Formula**	**CAS Number**
Ammonium Hydroxide	Sigma Aldrich	NH_4OH	1336-21-6
Betaine	Sigma Aldrich	$C_5H_{11}NO_2$	107-43-7
Calcium Chloride	Sigma Aldrich	$CaCl_2$	10043-52-4
D-Glucose	Sigma Aldrich	$C_6H_12O_6$	50-99-7
n-Dodecyl ß-D- maltoside	Sigma Aldrich	$C_{24}H_{46}O_{11}$	69227-93-6
EDC (1-Ethyl-3-(3-Dimethyl-aminopropyl) Carbodiimide)	VWR	$C_8H_{17}N_3$	25952-53-8
1H, 1H,2H,2H-Perfluoro-1-octanethiol	Sigma Aldrich	$CF_3(CF_2)_5CH_2CH_2SH$	34451-26-8
Hydrogen peroxide	Sigma Aldrich	H_2O_2	7722-84-1
Magnesium Chloride	Sigma Aldrich	$MgCl_2$	7786-30-3
11-Mercaptoun-decanoic Acid	Sigma Aldrich	$HS(CH_2)_{10}CO_2H$	71310-21-9
(11-Mercaptoun-decyl)tri-(ethylene glycol)	Sigma Aldrich	$HS(CH_2)_{11}(OCH_2CH_2)_3OH$	130727-41-2
Methanol (Uvasol)	MERCK	CH_3OH	67-56-1
N-Hydroxy-succinimide	Sigma Aldrich	$C_4H_5NO_3$	6066-82-6
PIPES	Sigma Aldrich	$C_8H_{18}N_2O_6S_2$	5625-37-6
Silver Nitrate	Sigma Aldrich	$AgNO_3$	7761-88-8
Sodium Hydroxide	Sigma Aldrich	NaOH	1310-73-2
Sodium L-Ascorbate	Sigma Aldrich	$C_6H_7NaO_6$	134-03-2
Sulfuric Acid	——	H_2SO_4	——-
TransFluo-Spheres (633/720)	life technologies		T8870
Tricine	Sigma Aldrich	$(HOCH_2)_3CNHCH_2CO_2H$	5704-04-1

4

Interaction of Photosystem I with Bimetallic Nanoparticles

In this chapter, the influence of the bimetallic NPs on the optical properties of PSI at cryogenic temperature has been discussed. Bimetallic NPs of different compositions and layer orders of Au and Ag, were fabricated by thermal annealing. Using SMS the variations in fluorescence properties of single uncoupled and metal NP-coupled PSI complexes were investigated. The corresponding results are compared and discussed in this section.

Part of the work discussed here has been published under: Ashraf, I.; Skandary, S.; Khaywah, M. Y.; Metzger, M.; Meixner, A. J.; Adam, P. M.; Brecht, M. Effects of Irregular Bimetallic Nanostructures on the Optical Properties of Photosystem I from Thermosynechococcus elongatus. Photonics. 2015, 2(3), 838-854.

4.1 Background

The enhancement in fluorescence emission of bio-molecules due to interaction with monometallic NPs in proximity has been studied extensively in the last decades [100, 131, 226–228]. Increased fluorescence and photostability of the molecules in the vicinity to NPs influenced many research areas. Various devices, e.g., plasmon-enhanced LEDs [229], plasmon-enhanced optical sensors [230, 231], single-photon sources for quantum cryptography [232] and photonic crystal lasers [233, 234], have been devised depending on the altered spontaneous emission rates. In 2002 Geddes *et al.,* considered the outcome of the near-field of metallic NPs on the brightness and photostability of the chromophores and coined the term MEF [235]. The real mechanisms responsible for MEF are still part of the debate, however, the possible factors causing the modifications in the emission properties of the fluorophores are discussed in section 2.3.3.2. The enhancement of the fluorescence of fluorophores, nevertheless, can be controlled by controlling the distance between the fluorophore and metallic NP, their relative orientation, size and shape of the metallic NPs and the surrounding medium, etc., [236]. The enhanced brightness due to the coupling with NPs makes the detection of fluorophores at single molecule level easier, which otherwise is very challenging due to low signal intensities.

The effects of plasmonic interactions on the emission properties of PSI using ordered monometallic nanostructures (Fischer patterns), AuNPs, and silver island films (SIFs) were studied before at cryogenic temperatures [100, 226, 228]. An enhancement in the fluorescence up to 37-fold accompanied with a shift in spectral peak positions was reported. [152]. During this project work, the study was extended to explore the effects of disordered and arbitrary-shaped bimetallic NPs of different compositions on the emission properties of PSI. Bimetallic NPs have attracted a lot of attention due to their superior performance over their monometallic counterparts [237–240]. AgNPs, widely known to provide larger enhancement in fluorescence emission have weak stability in a biological environment which limits their applications.

In contrast to that, the AuNPs are very stable in biological environment, but their enhancement ability is feebler [241, 242]. Bimetallic NPs with the combined merits of both, AgNPs and AuNPs, offer the solution to benefit from the strong optical enhancement properties of the AgNPs and surface chemical properties of the AuNPs, simultaneously [146]. The bimetallic NPs were fabricated by thermal annealing of the thin metallic films. The choice of this fabrication technique was made because of its simplicity and low cost way of fabrication. In addition, this technique is able to produce large-scale substrates, and optical properties of the NPs can be tuned easily [146, 221]. PSI complexes isolated from *T. elongatus* were coupled to these bimetallic NPs and corresponding effects were investigated by using a home-built confocal microscopy setup operating at a cryogenic temperature (1.6 K). PSI was used, as it is one of the most sophisticated and efficient multi-subunit trans-membrane complexes responsible for harvesting solar energy to support light-induced charge separations. It absorbs a broad spectral range of the solar radiation reaching the Earth's surface. Regardless of the wavelength, almost each captured photon drives an electron translocation and resultant QY of the charge separation approaches to unity [36]. Such a remarkable QY makes the PSI an ideal candidate for photoelectronic and photochemical devices [40, 243–245]. The light harvesting antenna in PSI contains some coupled Chl *a* dimers and trimers, which absorb light at longer wavelength than P700. These Chl *a* molecules have a different number in different organisms and are known as red or LWCs. Their key roles lie in increasing the spectral width of light absorption, facilitating the efficient light energy capturing under extreme environmental conditions and funnelling the excitation energy to the centre of the complex [18, 86]. At physiological temperatures, the energy absorbed by the LWCs is efficiently transferred to P700 to provoke the translocation of an electron. At cryogenic temperatures, however, the transfer of energy to P700 is partially blocked and the LWCs act as a trap for excitation energy. The trapped energy is partially released in the form of fluorescence [88]. A detailed description about PSI and LWCs can be found in section 2.2.

The fluorescence of the single uncoupled and bimetallic NP-coupled PSI complexes from *T. elongatus* was detected using SMS. The emission spectra of a number of the individual PSI complexes were collected and statistical analysis was made to comprehensively explore the influence of bimetallic NPs on the emission properties of PSI. SMS was used, as it offers the opportunity to investigate the dynamics of individual molecules and unravel the information hidden in the ensemble spectra by avoiding the ensemble averaging effects [246]. The advantages of performing the measurements at cryogenic temperature are linked to the reduced conformational fluctuations in proteins and their environment. This leads to an increased photo and frequency stability of protein-bound chromophores and allows the spectroscopic studies with high spectral sensitivity [173]. A detailed description of the advantages of SMS and measurements at cryogenic temperatures can be found in section 2.4. Based on the collected spectral data at cryogenic temperature the variations in the emission profiles of PSI due to coupling with different bimetallic NPs are discussed.

4.2 Fabrication of NPs and Preparation of Bio-Nanohybrids

The metallic NPs investigated in this study were fabricated by Mohammad Y. Khaywah at Laboratory of Nanotechnology, Instrumentation, and Optics, UTT, France. Three substrates with different compositions and orders of Au and Ag layers were fabricated and named as Au/Au, Ag/Au and Au/Ag. The fabrication was carried out by stepwise thermal annealing of multiple thin films of Au and Ag. The general procedure for the thermal annealing of a single metal film is explained in detail in section 3.2.1. Here, a brief description about the fabrication of bimetallic NPs is given. The Au/Au substrates were fabricated by three successive evaporations of 2 nm thin gold films such that each of the evaporation was followed by a thermal annealing for 20 seconds at 250° C. For Ag/Au substrates, the fabrication was started by evaporating a 2 nm Ag film pursued by thermal annealing

under similar experimental conditions (temperature and annealing time). Immediately after the thermal annealing step, a 2 nm film of Au was evaporated. For Au/Ag substrate identical steps were adopted with opposite order of metal layers. Here at first a 2 nm thin Au film was evaporated followed by a thermal annealing step. Afterwards, a 2 nm layer of Ag was evaporated. A detailed description of the procedure can be found in Ref: [146, 221].
In order to prepare a bio-nanohybrid, highly diluted solution of isolated and purified PSI trimers from *T. elongatus* was prepared as described in section 3.1.1.3. A small amount (1 μL) of this solution was sandwiched between two bare glass coverslips or between a bare glass coverslip and respective metallic nanostructured surface (Au/Au, Ag/Au, Au/Ag) to prepare the hybrids of uncoupled and bimetallic NP-coupled PSI. Spectroscopic measurements were performed using home build confocal microscope setup at cryogenic temperature (1.6 K). A cw diode laser of wavelength λ_{exc}= 665 nm with a laser power of ∼100 μW was used for excitation. For each data set, 100 spectra were collected from individual uncoupled and coupled PSI complexes.

4.3 Results

4.3.1 Optical and Morphological Characterization

The morphology of all the substrates was characterized by using SEM (Schottky Jeol 6500F SEM, with 1.5 nm resolution at 15 kV). Fig. 4.1 (a-c) displays the typical SEM images of the Au/Au, Ag/Au and Au/Ag substrates fabricated under similar experimental conditions. The particles are disordered with different inter-particle spacing, size, and shape distributions. For Au/Au sample the size of the particles varies between 6 - 47 nm with an average diameter of the particles ∼19 nm. While for Ag/Au and Au/Ag samples, the diameter varies in the range between 4 - 34 nm with an average diameter of 16 nm. The particles in all three substrates exhibit an arbitrary shape distribution. Some of them are round while the others are elongated. Compared to the NPs of double layer substrates Ag/Au and Au/Ag, those

of triple layer substrate Au/Au have smaller inter-particle spacing and relatively larger and more uniform size and shape distribution. For Ag/Au

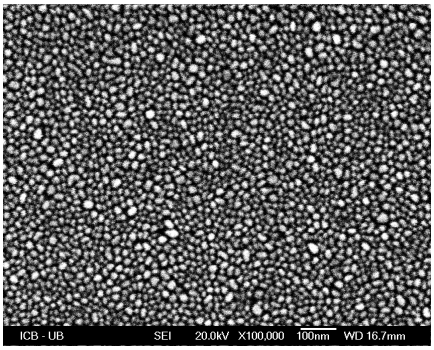

(a) Au/Au

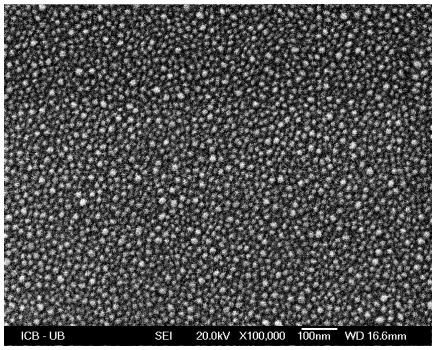

(b) Ag/Au

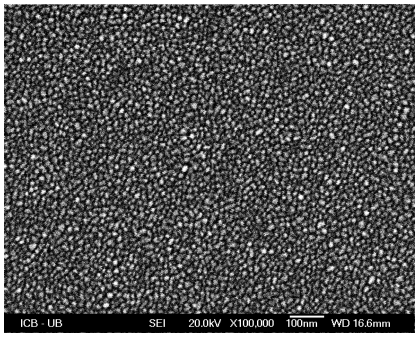

(c) Au/Ag

FIGURE 4.1: SEM images of three different substrates, fabricated under similar experimental condition but with different metallic compositions. (a) Au/Au: fabricated by three consecutive evaporations of only gold films, while each two evaporations are separated by thermal annealing, (b) Ag/Au: fabricated by the evaporation of Ag film followed by thermal annealing and Au film evaporation, respectively. and (c) Au/Ag: fabricated by consecutive evaporation of Au and Ag films separated by thermal annealing.

and Au/Ag substrates, the surface coverage was $\sim 41\%$, while for Au/Au, it was $\sim 49\%$. The more detailed description about the morphology of the substrates can be found in Ref: [146].

The absorption spectra of triple layer Au/Au, double layer Ag/Au and Au/Ag substrates is displayed in Fig. 4.2. The LSPR maxima are positioned at 691, 820 and 686 nm, respectively. To record the absorption spectra of the NPs an inverted microscope (Nikon Eclipse Ti-U) equipped with a spectrometer (Ocean Optics QE 6500) available at Prof. Dr. Monika Fleischer group was used together with Ph.D. student Andreas Horrer. It was found that Au/Au NPs show more defined, sharper and well shaped

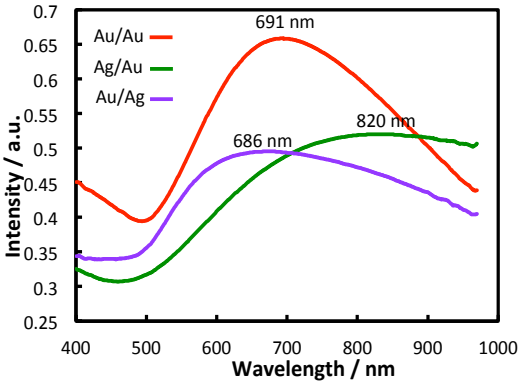

FIGURE 4.2: Absorption spectra of triple layer Au/Au, double layer Ag/Au and Au/Ag samples.

peak compared to the broad and less intensive peaks of Ag/Au and Ag/Au substrates. The difference in the absorption spectra of the substrates is attributed to different metal compositions, shapes and sizes of the NPs and dissimilar inter-particles spacings [146, 221]. It has been reported that the spectral overlap of the absorption and emission wavelength of the fluorophore with the absorption of the metallic NPs [111, 133, 234, 247], and geometrical properties of the metallic NPs [134, 136] are crucial parameters to guarantee an optimal coupling between fluorophore and NPs. Therefore, the NPs were fabricated under controlled experimental conditions, including evaporation rate, annealing temperature and timing, metallic film thickness and vacuum evaporator pressure etc., to achieve the required plasmon resonance.

4.3.2 Spectral Analysis of Single PSI Complexes

In order to study the effects of plasmonic NPs on optical properties of PSI complexes, spectral analysis of the individual uncoupled and metallic NP-coupled PSI complexes was carried out. The hybrids were prepared as discussed in section 4.2. To conduct a comparative study, NPs of different metallic compositions were fabricated and the corresponding effects on the emission properties of PSI were examined. A hybrid with PSI complexes between two bare glass coverslips was named as uncoupled PSI while the hybrids with PSI between glass coverslips and respective bimetallic NPs were named as PSI-Au/Au, PSI-Ag/Au and PSI-Au/Ag. Uncoupled PSI samples

were used as a reference to compare the results. The samples were prepared outside the cryostat and subsequently were quickly inserted onto the scanning desk in the pre-cooled cryostat (4.2 K) by using fast sample transfer mechanism. A detailed description can be found in Ref: [190]. All the measurements were performed under identical experimental conditions that include: temperature (1.6 K), excitation wavelength (λ_{exc}) and laser excitation power, etc. In order to achieve really comparable data at single molecule level for all the hybrid systems, multiple calibration measurements were performed in between with a standard sample (TransFluoSpheres, Life technologies, GmbH). A large number of spectral series of individual uncoupled and bimetallic NP-coupled PSI complexes were collected by the time-dependent SMS. The spectral data was analysed by using a home developed Matlab software called "SMS Analyzer". The software was developed by Dr. Martin Hussels as a part of his Ph.D. project together with Caroline Arnold (student assistant, Hiwi). A detailed description of the structure and functions of the software can be found in Ref: [79]. Fig. 4.3 displays four exemplary time-dependent fluorescence emission sequences of individual uncoupled and metallic NP-coupled PSI complexes. The sequences of the spectra from single uncoupled and Au/Ag coupled PSI complexes were taken with an acquisition time of 2 s per spectra, while for Au/Au and Ag/Au coupled complexes with 1 s per spectra. A direct effect on the fluorescence emission intensity of the PSI complexes due to coupling with metallic NPs can be observed. The coupling with Au/Au and Ag/Au NPs resulted in a strong enhancement of fluorescence emission, while coupling with Au/Ag NPs resulted a minute enhancement. To show a comparative spectral analysis of the uncoupled and metal NP-coupled PSI complexes the mean of all the spectra from single uncoupled PSI and PSI-Au/Au, PSI-Ag/Au, PSI-Au/Ag are plotted in Fig. 4.4 (a). The spectra are plotted after the baseline corrections. Strong differences in the fluorescence intensities of different bio-nanohybrids can be seen clearly. The spectral position of the emission maxima for uncoupled PSI was found at 730.4 nm, whereas for PSI-Au/Au with a slight redshift was found at 731.3 nm, while for PSI-Ag/Au and PSI-Au/Ag with a slight

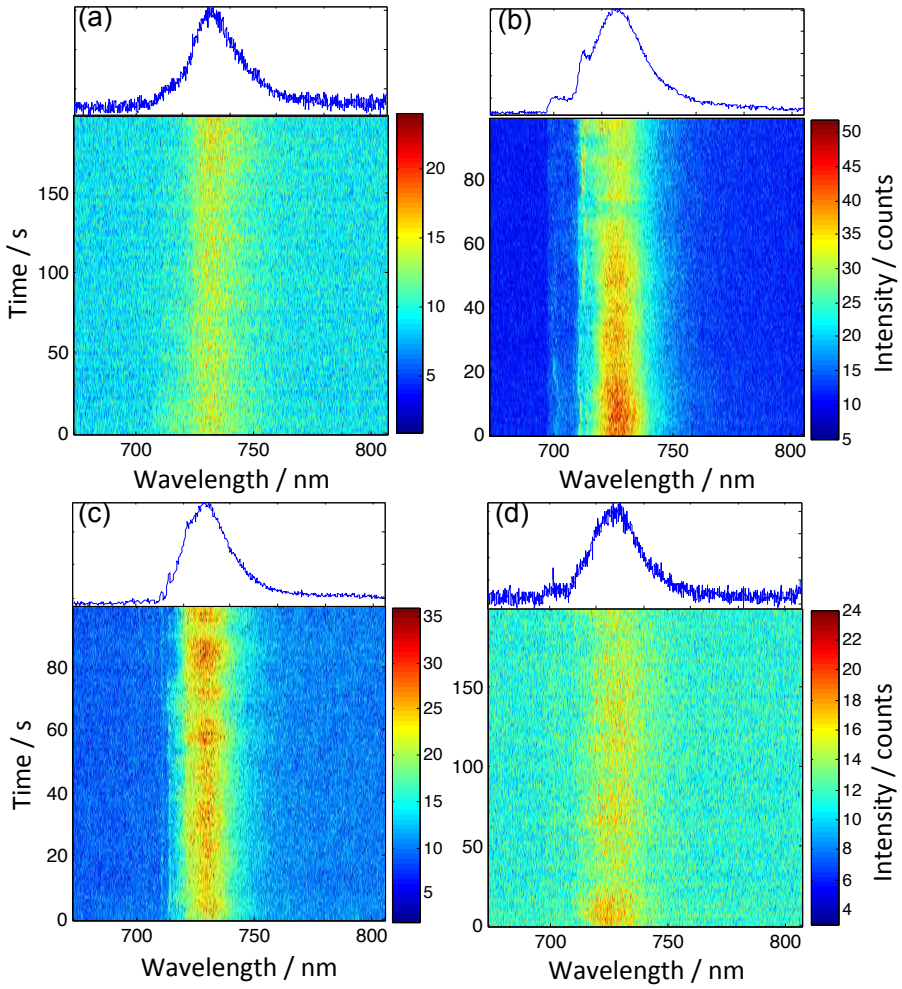

FIGURE 4.3: Time-dependent fluorescence emission sequences taken continuously from one single complex (a) uncoupled PSI, (b) PSI coupled to Au/Au sample, (c) PSI coupled to Ag/Au and (d) PSI coupled to Au/Ag. The time sequences of 100 spectra with time resolution 1s / spectrum were taken for every hybrid system. On top of the sequences are displayed the mean of all the spectra, respectively.

blueshift were found at 729.7 nm and 728.9 nm, respectively. To observe the modifications in emission profiles more precisely the average spectra were scaled to a similar maximum value in Fig. 4.4 (b). It can be observed that for both PSI-Au/Au and PSI-Ag/Au an additional broad shoulder appeared in the far red region between 780 - 850 nm, while for PSI-Au/Ag there was more quenching in the red region. The full width at half maximum (FWHM) of the emission profiles was also slightly altered due to the interaction with the metallic NPs. The modifications in the intensity of fluorescence were different for different bio-nanohybrids. For both PSI-Au/Au and PSI-Ag/Au

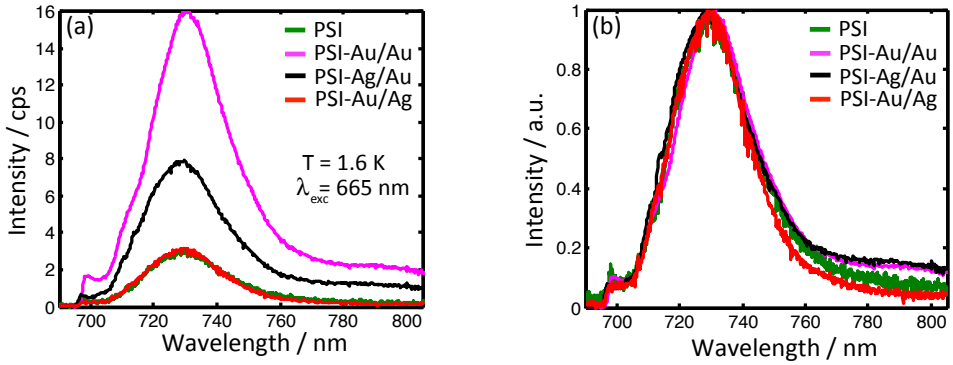

FIGURE 4.4: (a) Mean of all spectra from single PSI trimers (*T. elongatus*) for uncoupled, PSI-Au/Au, PSI-Ag/Au and PSI-Au/Ag after baseline correction at T = 1.6 K upon excitation at 665 nm. The accumulation time for uncoupled and PSI-Au/Ag was 2 s, while for PSI-Au/Au and PSI-Ag/Au was 1 s. (b) The normalized average spectra, scaled to the same maximum value after baseline correction. No pronounced broadening in the linewidth of any sample was found.

the intensity was strongly enhanced while for PSI-Au/Ag the enhancement was minimal with a slight quenching in the red part of the spectra. The enhancement was stronger for PSI-Au/Au than PSI-Ag/Au. Analogous to the main peaks, the additional shoulder appeared in far red region for PSI-Au/Au was also more intense compared to the shoulder of PSI-Ag/Au sample. The comparison of spectral peak positions and FWHM are given in Table 4.1. To elaborate the appearance of the additional shoulder in the far red region, a comparison of the spectra from three individual complexes of each, uncoupled PSI, PSI-Au/Au, PSI-Ag/Au and PSI-Au/Ag is shown in Fig. 4.5. Clear, distinctive and broad enhanced shoulders, which appeared for both of the PSI-Au/Au and PSI-Ag/Au samples in the wavelength range 780 - 850 nm, are evident. The red arrows point out these broad shoulders, which were consistent in all datasets of PSI-Au/Au and PSI-Ag/Au with varying intensity, while such shoulders were not found for uncoupled and Au/Ag coupled PSI complexes.

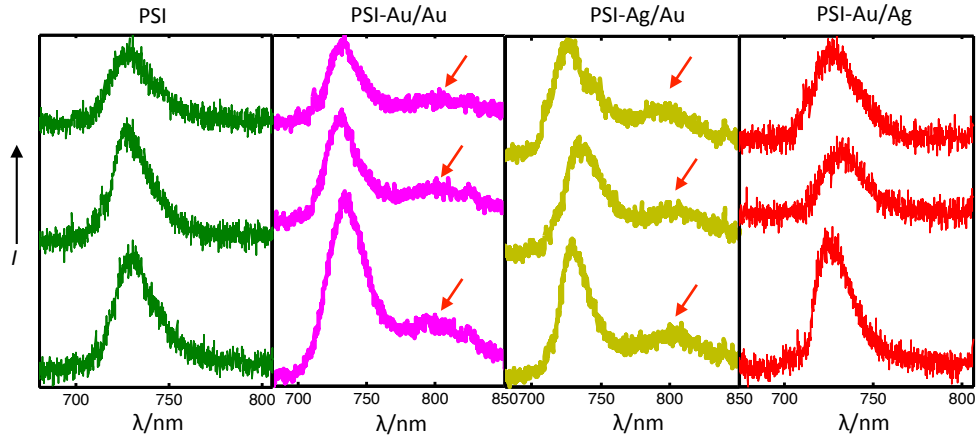

FIGURE 4.5: Comparison of three individual spectra from three different single complexes of each (a) uncoupled PSI (b) PSI-Au/Au and (c) PSI-Ag/Au. The red arrows point to the broad enhanced shoulders appeared in the far red region (from 78050 nm) for almost all coupled complexes of PSI-Au/Au and PSI-Ag/Au samples. The accumulation time for each uncoupled PSI complex was 2 s, while for PSI-Au/Au and PSI-Ag/Au, it was 1s.

4.3.3 Wavelength Dependent Enhancement

The wavelength dependent EF is the ratio of fluorescence emission intensity of the metallic NPs-coupled PSI to the uncoupled PSI at a specific wavelength. To investigate the dependence of fluorescence emission intensity on wavelength, the average spectra of PSI-Au/Au, PSI-Ag/Au, and PSI-Au/Ag were divided by the average spectra of uncoupled PSI. The resulting curves obtained are plotted in the range between 690 - 805 nm as shown in Fig. 4.6. From wavelength dependent enhancement (WDE) curves, it is found that for PSI-Au/Au sample, the intensity was enhanced continuously in the entire wavelength range with three domains of relatively high enhancement. A major broad domain was observed around the main emission peak region in the range 720 - 760 nm and two relatively narrow domains in the blue side from 706 - 716 nm and far red region 780 - 805 nm, respectively. For PSI-Ag/Au sample, a similar trend of continuous enhancement was observed, but the intensity enhancement was comparatively low as compared to the PSI-Au/Au. Additionally, there was only one prominent domain in the far red region in the range 780 - 805 nm with a comparatively high intensity enhancement. In contrast to PSI-Au/Au and PSI-Ag/Au, for PSI-Au/Ag

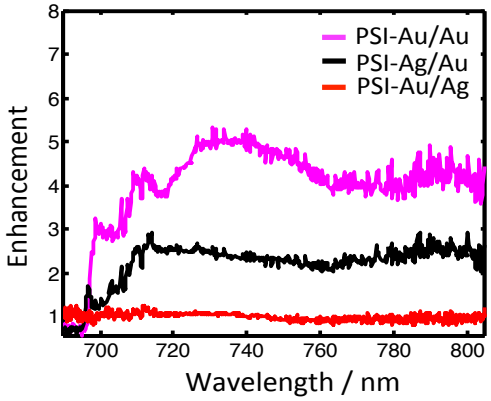

FIGURE 4.6: Wavelength-dependent enhancement spectra obtained after dividing the average spectra of PSI-Au/Au, PSI-Ag/Au and PSI-Au/Ag by the average spectrum of uncoupled PSI. The enhancement for PSI-Au/Au and PSI-Ag/Au was observed more around main peak region (730 nm) and in the far red region (> 780 nm). For PSI-Au/Ag, the intensity was nearly same around the main peak region, but there was a slight quenching in the region 745 - 790 nm.

the shape of the WDE spectra was nearly similar to uncoupled PSI with only a slight increase in intensity around the main peak region. However, in the region >745 nm the slope became slightly negative, indicating a slight quenching in the region 745 - 790 nm. The maximum value of WDE found for PSI-Au/Au is $\sim$ 5.34-fold and for PSI-Ag/Au and PSI-Au/Ag are $\sim$ 2.9 and 1.25-fold, respectively. For PSI-Au/Au, the maximum WDE was around the main peak region while for PSI-Ag/Au and PSI-Au/Ag it was in the region $<$ 720 nm. It is worth noting that, because of the dependence of the selected procedure on the elimination of background contributions, the risk of error in a spectral region with low intensity becomes higher compared to the high intensity spectral region.

4.3.4 Fluorescence Emission Enhancement

The interaction with plasmonic NPs resulted in modifications in, both, the shape and intensity emission spectra of the individual PSI complexes. The intensity was significantly enhanced for PSI-Au/Au and PSI-Ag/Au, while for PSI-Au/Ag the enhancement was negligibly small. The relative intensity of individual spectra from NP-coupled PSI with respect to the mean intensity of uncoupled PSI is defined as EF. In order to calculate the EF

for individual bimetallic NP-coupled PSI complexes, the intensity counts of the recorded spectra from each single uncoupled and coupled PSI complexs were numerically integrated after baseline correction. The resulting counts of each individual NP-coupled PSI complex were compared to the average intensity counts of all uncoupled PSI complexes. The distribution of the EFs calculated for PSI-Au/Au and PSI-Ag/Au together with the intensity distribution of uncoupled PSI complexes is displayed in Fig. 4.7. The histogram in (a) displays the distribution of EFs for PSI-Au/Au and (b) displays for PSI-Ag/Au. The green bars are showing the intensity distribution of uncoupled PSI. The distribution of uncoupled PSI complexes appeared to have nearly

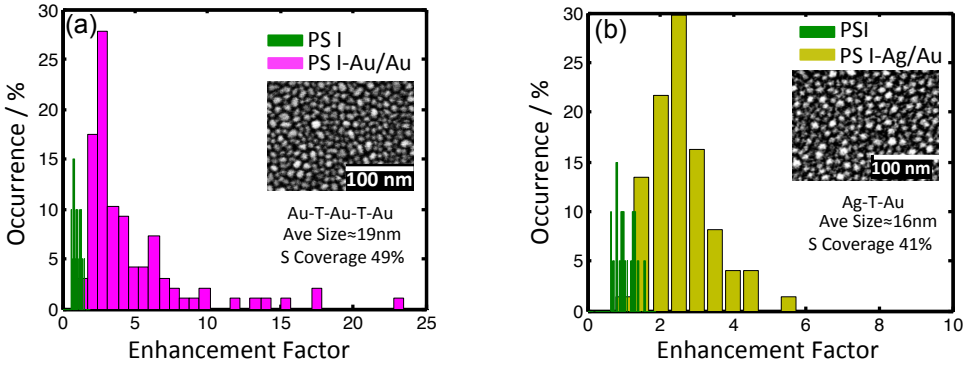

FIGURE 4.7: Comparison of the enhancement factors (EFs) for (a) PSI-Au/Au (magenta) and (b) PSI-Ag/Au (yellow) plotted together with the intensity distribution of uncoupled PSI (green) complexes. The insets are shown the SEM images of the respective NPs used for the investigations. The intensity counts of individual recorded spectra were integrated after baseline correction and compared to the mean intensity counts of uncoupled PSI. The average EFs for PSI-Au/Au and PSI-Ag/Au are 4.4 ± 3.9 and 2.3 ±0.8, respectively. The x-axis defines the EF, whereas the y-axis shows the relative percentage of occurrence of the datasets with respective EFs.

gaussian shape, while, for both the NP-coupled samples, PSI-Au/Au and PSI-Ag/Au, the distribution of EF initially showed a steep increase to maximum value and afterwards decayed almost exponentially. For PSI-Au/Ag, the distribution of intensity from individual uncoupled PSI complexes and EFs from PSI-Au/Ag showed nearly similar shape. Compared to PSI-Au/Au and PSI-Ag/Au the enhancement for PSI-Au/Ag was negligibly small, as can be perceived from Fig. 4.8. Inset are shown the SEM micrographs of

the respective bimetallic NPs used for the investigation. In addition, the information about the metallic composition, order of the involved fabrication steps, average size of the particles and surface coverage is given. The letter 'T' is a representation of the thermal annealing step. On average the fluores-

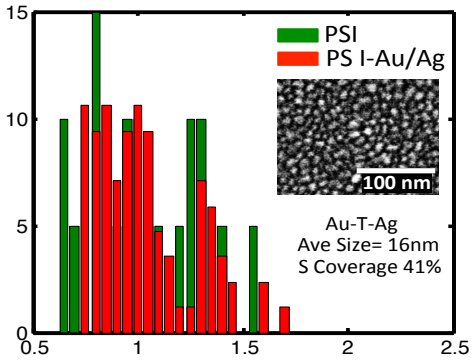

FIGURE 4.8: The distribution of EFs for PSI-Au/Ag. The enhancement in the emission intensity was negligibly small. On average the intensity was enhanced by a factor of 1.02 ± 0.3.

cence was enhanced by a factor of 4.4 ± 3.9 and 2.3 ± 0.8-fold for PSI-Au/Au and PSI-Ag/Au, respectively. For PSI-Au/Ag, the intensity was enhanced only 1.02 ± 0.3-fold (Fig. 4.8). For some individual complexes, however, the EF even up to 22.9, 5.1 and 1.7-fold was found for PSI-Au/Au, PSI-Ag/Au, and PSI-Au/Ag, respectively. The average and maximum intensity EF due to coupling with arbitrary shaped and randomly oriented Au/Au NPs was higher than those of well-ordered gold Fischer patterns (Au△), reported previously in Ref: [100]. Table 4.1 shows the comparison of peak positions, EFs, line widths and standard deviations of EFs for uncoupled PSI and all the bio-nanohybrids.

TABLE 4.1: Comparison of the peak positions, enhancement factors (EFs), linewidths and standard deviations of EFs observed for uncoupled and coupled PSI complexes.

Sample	uncoupled PSI	PSI-Au/Au	PSI-Ag/Au	PSI-Au/Ag
Emission Maximum (nm)	730.4	731.3	729.7	728.9
FWHM (nm)	27.6	27.3	28.3	26.9
Average Enhancement	-	4.4	2.3	1.1
Max. Enhancement	-	22.9	5.1	1.7
Standard Deviation	0.3	3.9	0.8	0.3

4.4 Discussion

The results reported in this chapter have shown the exciting effects of bimetallic NPs on the optical properties of trimeric PSI from *T. elongatus*. It has been found that the intensity, as well as the shape of the spectra from individual PSI complexes, is altered due to the coupling with bimetallic NPs. Studies have revealed that the spectral overlap between LSPR of the metallic NPs and absorption and emission spectra of fluorophore [133, 234, 247, 248], distance between the metallic NPs and the fluorophores [67, 248], their relative orientation [249] and spectral peak position of SPR of NPs with respect to the emission of fluorophore [133, 250], plays critical role in altering the fluorescence of the fluorophores. Therefore, the NPs were fabricated under controlled experimental conditions e.g., metallic film thickness, annealing temperature and time for annealing etc. [146, 221], to obtain the NPs with different SPR peak positions covering a broad range of wavelengths. Such NPs, thus, offer the possibility to analyse the effects of many above mentioned key factors.

All the bimetallic NPs investigated in this study resulted in an enhancement in the fluorescence emission of coupled PSI complexes. The volume of enhancement was different for different substrates. On average the integral fluorescence intensity was enhanced by a factor of 4.4 $\pm$ 3.9 for PSI-Au/Au, while for PSI-Ag/Au and PSI-Au/Ag the corresponding values were 2.3 $\pm$ 0.8 and 1.02 $\pm$ 0.3-fold, respectively. For some individual complexes, however, the EF reached up to even 22.9, 5.1 and 1.7-fold for PSI-Au/Au, PSI-Ag/Au, and PSI-Au/Ag, respectively. The average EF due to Au/Au NPs is almost twofold larger and for Ag/Au NPs it is comparable to the results reported for the regular, homogeneous and periodic arrays of gold triangles (Au $\triangle$) [100, 226]. For Au/Ag substrate, the EF was too small to compare. The difference in EFs due to coupling with Au/Au, Ag/Au and Au/Ag is attributed mainly to the different spectral overlaps between LSPR of bimetallic NPs and emission of PSI, sharpness of the plasmon resonance peaks and surface oxidation effects [146, 247, 251].

Spectral overlap of LSPR with the absorption and emission spectra of the fluorophore and excitation wavelength is crucial for altering (i.e., quenching or enhancing) the fluorescence emission of the fluorophore [133, 247, 252]. The fluorescence intensity of the proteins have been reported to enhance strongly when excited in the spectral region of LSPR compare to excitation far out of plasmon resonance feature [247]. Furthermore, the dyes with their emission peak redshifted to the LSPR peak of NPs were the subject of more enhancement [133, 250]. The highest fluorescence enhancement due to Au/Au was discussed considering these factors. For Au/Au, the absorption spectrum is well defined and more intensive with LSPR maxima at 691 nm, leading to stronger spectral overlap with absorption and emission spectra of trimeric PSI. Additionally, the fluorescence emission maxima of PSI is redshifted from the LSPR peak and the excitation at 665 nm is also well in the spectral range of Au/Au NPs. Therefore, the maximum enhancement of fluorescence due to coupling with Au/Au NPs complies with the reported results. Additionally, Au/Au substrates were fabricated by a coating of three layers in contrast to the double layer fabrication of Ag/Au and Au/Ag. Due to the additional layer, the density of the particles in the Au/Au substrate was increased and the inter-particle distance was decreased. The smaller inter-particle space lead to more uniform hotspots and consequently stronger enhancement [146]. Contrary to Au/Au, for Ag/Au the LSPR maximum ($\sim$ 820 nm) is far redshifted from excitation wavelength (665 nm), as well as, emission maxima of trimeric PSI from *T. elongatus*. The LSPR spectra is also very broad and less intensive. As a result the enhancement of the fluorescence emission is less. For Au/Ag, on the other hand, the maximum of LSPR is located at 686 nm, which is blue shifted from the emission maximum of PSI. The excitation is well in the spectral range of plasmon resonance feature. Also, the top layer of Au/Ag substrate is of silver (Ag), which is known to lead stronger enhancement. Therefore, a stronger enhancement was expected for PSI-Au/Ag. The experimental results, however, were conflicting to the expectations, resulting in the least (negligibly small) enhancement compared to its counterparts. This conflict can be explicated considering the surface

oxidation effect. Prior to the measurements, the Au/Ag substrate was stored under ambient conditions for over two months. Silver, despite being from the noble metal family is renowned for its easy oxidation [253, 254]. Once oxidized, the AgNPs are reported to lead a drop in EF [251]. It was therefore hypothesized that the storage of Au/Ag substrate under ambient conditions for such a long time may have resulted in the oxidation of the Ag layer. That consequently may have lead to a decrease in EF, which otherwise was expected to increase substantially.

The histograms shown in Fig. 4.7 exhibit more heterogeneous distribution of EFs for PSI-Au/Au and PSI-Ag/Au compared to the uncoupled PSI complexes. The standard deviations of the EFs for uncoupled PSI, PSI-Au/Au, and PSI-Ag/Au samples are presented in Table 4.1. The high standard deviations of EFs of PSI coupled to Au/Au and Ag/Au substrates were linked to the: (i) heterogeneity in the size of the metallic NPs [255]; (ii) the distance dependence of the interaction between plasmonic NPs and fluorophores [67]; and (iii) different emission/excitation dipole orientations. The size of the metallic NPs investigated in our study was not homogenous, but it varied between 6 - 47 nm for the Au/Au substrate and between 4 - 34 nm for the Ag/Au and Au/Ag substrates, as can be seen in the SEM images in Fig. 4.1 (the detail about the size distribution of the NPs can be found in Ref: [146]). It also has been shown both, theoretically and experimentally, that enhancement in fluorescence emission depends on the size of the metallic NP [136]. With the increase of the size of the metal NP up to a certain extent, the electric field gets stronger and also extends further out of the particle [136]. Depending on the strength of the field, the fluorescence enhancement will vary. For smaller particles the electric field will be weaker and feebly extended out so the resultant enhancement will also be less, while for bigger particles the field will be more intense and spread out, thus, a stronger enhancement will be the outcome. Applying the similar analogy to our hybrid systems, broad variation in the size of NPs produced a broad distribution of the near-fields and, therefore, a broad distribution of EFs. For Au/Au substrate because of an additional layer of Au, the size distribution was even

more spread and standard deviation of EF was higher.

The broad distribution of EF can also be ascribed to the distance (between fluorophore and the metallic NP) dependence of emission enhancement. It has been studied comprehensively that the enhancement or quenching of the fluorescence of a fluorophore is highly distance dependent [67, 247]. It was found by Anger *et al.,* that for a distance of 2 nm or shorter the emission was quenched, but, as the distance increases the enhancement started increasing and reached a maximum value at $\sim$ 5 nm. At a distance higher than 5 nm, the fluorescence of the coupled fluorophore decayed exponentially, leading to vanishing enhancement at $\sim$ 80 nm, suggesting the absence of any coupling between the NP and the fluorophore [67]. PSI in its trimeric form has a clover-shaped structure with a diameter around $\sim$ 22 nm and approximately 5 nm in height composed of almost 288 Chl *a* molecules [86]. Considering a similar distance-dependence of enhancement for Au/Au and Ag/Au as observed for a fluorophore coupled to a AuNPs, some of the Chl *a* molecules will be in the distance range where maximum enhancement will occur, while others will be in the range where quenching of the fluorescence will be a dominant phenomena, so the ultimate EFs will be different for different coupled complexes, resulting in the broad distribution.

The emission spectra of PSI coupled to Au/Au, Ag/Au, and Au/Ag were nearly similar to uncoupled PSI without any pronounced changes in the emission profiles. Analogous to single-chromophore and two-chromophore FRET- coupled systems, the enhancement of the fluorescence emission of PSI coupled to Au/Au, Ag/Au, and Au/Ag was uniform. Slight deviations in the shape of emission profiles in the form of minute modifications in the line widths and spectral peak positions were noticed for all the bio-nanohybrids (Fig. 4.4). The comparison of the resulting linewidths and peak positions is shown in Table 4.1. The studies about the influence of the plasmonic interactions on the functionality of photosynthetic proteins have established that even in close proximity to metallic NPs the PSI complexes maintain their charge-transfer and light harvesting capabilities [243, 256]. Based on the literature, the modifications in the structure of PSI complexes

due to interactions with the bimetallic NPs in the proximity seems improbable. The observations made in our lab with different metallic NPs to study the plasmonic interactions with PSI have revealed that the enhancement in fluorescence and the deviation in the shape of the emission spectra go hand in hand. For those metallic NPs (AuNPs and SIF) which resulted much higher enhancement in fluorescence emission of PSI, the resultant deviations in the emission profiles of coupled systems were also very strong [100, 226, 228]. Contrary to that, for the metallic NPs (Au/Au, Ag/Au and Au/Ag) investigated in this study the resultant EF were smaller and so were the deviations in the shape of the emission spectra. The deviations from the uniform enhancement were attributed to the couplings between the chromophores in PSI [100, 228].

Due to the coupling with NPs, additional enhanced fluorescence shoulders in the far red spectral region (> 770 nm) were noticed for both PSI-Au/Au and PSI-Ag/Au samples and are displayed in Fig. 4.5. These shoulders can be attributed to "vibronic sidebands corresponding to the mirror image of the Q_y ($0 \rightarrow 1$) absorption band of LWC C708" [88]. In oxidation form of $P700^+$ the fluorescence intensity on the long-wavelength side of the main emission peak is quenched [88], because $P700^+$ has a broad absorption band that shows a considerable overlap with the fluorescence spectrum of LWCs [158, 257]. As a result, the fluorescence of LWCs should reduce, but in contrary, we observed an enhancement in this region. This gain in fluorescence intensity, therefore, can only be explained by considering a dramatic change in the process of fluorescence quenching by $P700^+$ due to the presence of the metallic NPs [100]. Therefore, it was assumed that the metallic NPs may have changed the irreversible energy transfer pathways from red Chls to $P700^+$, resulting in the lower quenching of fluorescence.

4.4.1 Proposed Mechanism

The actual mechanisms behind the enhancement of fluorescence emission due to the metallic NPs in proximity to the fluorophores are still part of the

debate. And it becomes even more difficult to propose a mechanism for complex multichromophoric biological systems such as PSI. However, considering (i) the transfer of energy from the plasmons to the PSI, (ii) generation of new energy transfer pathways and (iii) appearance of new emission channels, etc., the enhancement in the fluorescence emission of PSI can be discussed. The metallic NP in the proximity acts as an additional antenna and transfers energy from the plasmons to PSI, which causes an enhancement in excitation rate and consequently an enhancement in the fluorescence emission [152, 153]. In an uncoupled PSI complex, the excitation energy captured by the antenna system is efficiently transferred to the RC through the involved chromophores. To ensure the fast and efficient transfer of excitation energy to the RC the chromophores are coupled together [89]. The energy transfer rates among the chromophores of photosynthetic pigment-protein complexes depend on the spectral overlap, spatial separation and orientation of the involved chromophores [155]. The specific coupling conditions between the chromophores lead to a characteristic set of transition rates and, thus, to preferred energy transfer pathways [155, 156]. Fig. 4.9 (a) shows the exaggerated energy transfer pathways for uncoupled PSI. The effect of plasmonic interaction on the Förster interaction distance of the coupled chromophores was studied by Zhang *et al.* [154]. They have found that depending on the size of the NPs and the distance from the particle, the Förster radius between chromophores alters due to the interaction with plasmonic NPs [154, 258]. For a single donor-acceptor pair, they noticed that the Förster radius increased from 8.3 - 13 nm [154]. Following the similar analogy for PSI, it was speculated that the coupling between PSI-bound chromophores was disturbed due to the interaction with metallic NPs in close vicinity. Consequently, the naturally existing energy transfer pathways were distorted and new energy transfer pathways were developed among chromophores, leaving effects on the energy transfer efficiencies. As a result, the chromophores, which in their native state were not contributing in EET, also got involved in the process. And additional EET pathways as illustrated in Fig. 4.9 (b)

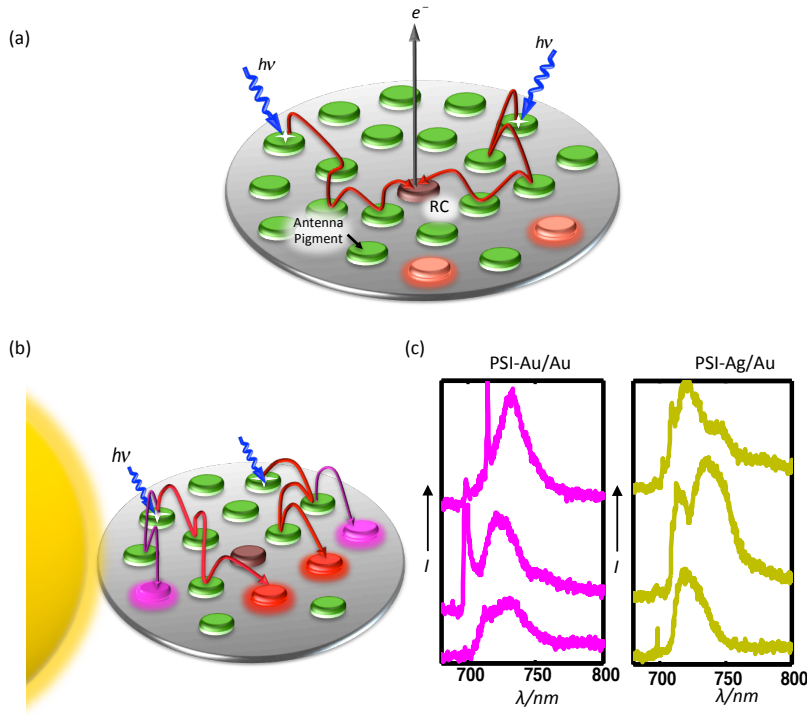

FIGURE 4.9: (a) An exaggerated illustration of energy transfer pathways in PSI. Due to the specific coupling among chromophores in the native state of PSI, energy is transferred to the RC by following certain energy transfer pathways. (b) In the presence of plasmonic NPs, the coupling among chromophores is changed, resulting in the emergence of new energy transfer pathways and the turning on of non-fluorescent Chl *a* molecules (magenta discs), as well. The representative emission spectra of individual coupled complexes for each of the sample types PSI-Au/Au and PSI-Ag/Au show the deviation in their shapes compared to the uncoupled PSI complexes, indicating the emergence of new energy transfer pathways.

were constituted. Furthermore, the chromophores that were initially non-fluorescent also become fluorescent (magenta discs). Thus, the fluorescence emission is enhanced [100, 228]. Variations in the shape of the emission spectra of PSI-Au/Au and PSI-Ag/Au shown in Fig. 4.9 (c) strengthens this hypothesis. The spectra show the extreme cases of WDE. In some cases, a strong enhancement was observed in the region around 720 nm while in some other cases was observed around 740 nm. Depending on the distance between metallic NP and chromophores in the PSI, the emission of the certain chromophores within one PSI will increase strongly whereas the emission of some others will be quenched. As a result, the metallic NPs-coupled PSI

complexes will exhibit remarkably altered shape than uncoupled PSI.

4.5 Summary

In this chapter, the interaction of the irregular bimetallic NPs with trimeric PSI from *T. elongatus* have been discussed. Three different nanostructured substrates Au/Au, Ag/Au and Au/Ag were fabricated by coating double and triple metal layers. Different metal compositions and film thicknesses resulted in arbitrarily shaped particles of different sizes and consequently of different SPR. The metallic NPs were coupled to single trimeric PSI complexes. Using SMS at cryogenic temperature, the emission spectra from a reasonable number of individual uncoupled and metal NPs-coupled PSI complexes were collected and the variations in the fluorescence emission properties were studied. It was found that the fluorescence emission of PSI was enhanced prominently due to coupling with the particles fabricated solely from gold (Au/Au) or if they had a gold film on top (Ag/Au), while for Au/Ag substrate, having a silver film on top, the enhancement was negligibly small with a slight quenching in the region 745 - 790 nm. The average enhancement for PSI-Au/Au and PSI-Ag/Au was 4.4 $\pm$ 3.9 and 2.3 $\pm$ 0.8-fold, while for PSI-Au/Ag the enhancement was 1.1 $\pm$ 0.3-fold. However, for individual complexes, an EF even up to 22.9, 5.1 and 1.7-fold was noted for Au/Au, Ag/Au and Au/Ag, respectively. Additionally, it was observed that the fluorescence showed a WDE.

The fluorescence enhancement effects were discussed considering the modifications in energy transfer pathways within PSI and the appearance of new emission channels. The large enhancement due to coupling with Au/Au substrate was assigned to large spectral overlap between absorption of metallic NPs and emission of PSI, while the least enhancement for Au/Ag substrate was assigned to oxidation of the silver layer on top. The wavelength dependence of the fluorescence enhancement was explained considering the multichromophore composition of PSI.

5

Temperature Dependence of Metal-Enhanced Fluorescence

This chapter presents the investigations of temperature dependence of the metal enhanced fluorescence (MEF) of PSI from T. elongatus. Monometallic NPs composed of gold only were fabricated by thermal annealing and the study was performed using SMS at 1.6, 90, 190 and 250 K. The results are discussed considering the rate model which includes the temperature dependence of the fluorescence yield of PSI and the spectral overlap between the absorption of metallic NPs and the emission of PSI.

Part of the work discussed here has been published under: Ashraf, I.; Konrad, A.; Lokstein, H.; Skandary, S.; Metzger, M.; Djouda, J. M.; Maurer, T.; Adam, P. M.; Meixner, A. J.; Brecht, M. Temperature Dependence of Metal-Enhanced Fluorescence of Photosystem I from Thermosynechococcus elongatus. Nanoscale. 2017, 9, 4196-4204.

5.1 Background

Due to the ability of the metallic NPs to influence the optical properties of neighboring emitters, such as organic dye molecules [67, 111, 131, 259], semiconductor crystals [255, 260] and biomolecules [74, 149, 152, 153, 228] etc., they appealed to many scientific and technological areas. They have been extensively used for detection of biological molecules [71, 74], surface-enhanced Raman spectroscopy (SERS) [261], medical imaging [72] and sensing applications [262].

Therefore, because of their huge attraction for the scientific community, investigation of the plasmonic interactions and understanding the actual mechanisms responsible for the modifications in the emission properties of the fluorophores was a hot topic in the last decade. Various studies were performed to examine different types of NPs and simple emitters, e.g., quantum dots or dye molecules, under different experimental conditions [64, 138, 260, 263–265]. Extensive studies of the interactions of NPs composed of different metals with complex multichromophoric systems, e.g., trimeric PSI and LHCs, were also carried out at the room, as well as, at cryogenic temperatures [47, 100, 153, 227, 228, 247]. In all the cases an enhancement in fluorescence emission was noted. The volume of the enhancement was different for the different metallic NPs and experimental conditions. The average enhancement was in the best case around 10-fold and the maximum enhancement never exceeded 40-fold [228]. In the previous chapter, an extensive study of the interactions of various bimetallic NPs with the PSI at cryogenic temperature is presented. It was found that on average the fluorescence enhanced by 4.4 (Au/Au), 2.3 (Ag/Au) and 1.1 (Au/Ag)-fold. For some individual complexes, the enhancements were raised up to 22.9 (Au/Au), 5.1 (Ag/Au) and 1.7 (Au/Ag)-fold. At cryogenic temperatures, the maximum enhancement so far have been observed was ∼37-fold, found for AuNPs by Nieder *et al.,* [228]. At room temperatures, however, an enhancement up to ∼200-fold was observed by Czechowski *et al.,* using SIFs under λ_{exc}=640 nm. For some individual complexes they even noted

the enhancement up to $\sim$ 250-fold [152]. These results hinted toward the crucial role of temperature in the enhancement of fluorescence emission of PSI.

Therefore, in light of these results, a study comprises of a series of experiments at different temperatures was performed and the temperature dependence of the experimentally determined EFs was discussed. Monometallic NPs of gold (AuNPs) fabricated by thermal annealing of the thin gold films were used for investigation. The measurements were performed at 1.6, 90, 190 and 250 K, using SMS. The spectral data from a reasonable number of the individual uncoupled and AuNP-coupled PSI complexes was collected and a detailed comparative investigation was made. The EFs at the respective temperatures were determined.

So far, the enhancement in fluorescence emission of the PSI has been discussed based on the enhanced excitation rates, modifications of EET pathways, generation of new EET pathways and activation of new emission channels [100, 152, 153]. In this study, additionally the role of the initial fluorescence quantum yield of PSI and spectral overlap between the absorption of NPs and emission of PSI has been included. Comparison of the results showed a strong temperature dependence of the MEF with a huge increase in the EF at higher temperatures. The strong temperature dependence of MEF is, thus, discussed based on the temperature dependence of initial fluorescence yield of PSI and of the spectral overlap. The gained better understanding of the enormous increase in fluorescence of AuNP-coupled PSI at higher temperatures will help to better understand the MEF of multichromophore systems in general.

5.2 Experimental Section

Monometallic AuNPs were fabricated following the procedure discussed in section 3.2.1 and in Ref: [221] with slight modifications. In brief, the AuNPs were deposited on thin glass coverslips by following the thermal annealing approach. The glass substrates were pre-cleaned for 20 minutes at 50° C

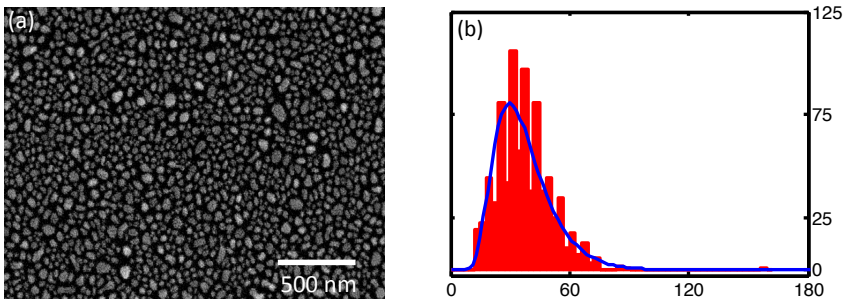

FIGURE 5.1: (a) SEM image of AuNPs fabricated on flat glass substrate by thermal annealing of 8 nm thin gold films at 300° C and (b) histogram of particle size distribution corresponding to SEM image. The NPs were of varying sizes in range 12 to 156 nm, with an average size of 36 nm.

with a mixture of detergent (Decon 90) and double-distilled water and dried prior to metal evaporation by using a nitrogen (N_2) stream. Contrary to bimetallic NPs where multiple thin metallic films separated by thermal annealing steps were evaporated, for monometallic NPs only a single thin gold film of thickness 8 nm was deposited on a glass coverslip using a vacuum evaporator under a pressure of $\sim 10^{-6}$ Torr. The sample was thermally annealed at 300° C by using a hot plate for 20 seconds, which led to the formation of NPs. Fig. 5.1 shows SEM image accompanied by the histogram of particle size distribution.

Trimeric PSI from *T. elongatus* was purified following the procedure described in Ref: [191]. PSI trimers were diluted stepwise in a buffer solution containing 20 mM Tricine, 25 mM $MgCl_2$, 0.4 mM β-DM, and 5 mM sodium ascorbate in milli-Q water to obtain a very low concentration ($\sim$3 pM) necessary for SMS. A detailed explanation of the sample preparation is given in section 3.1.1.3. Less than 1 μL of the diluted solution was sandwiched between two bare glass coverslips (for reference sample) and between a bare glass coverslip and the AuNPs (for actual sample), as shown in Fig. 3.3. The sample was then transferred to pre-cooled Helium bath cryostat using our fast sample transfer mechanism [190]. SMS was performed at different temperatures using a 665 nm *cw* diode laser at an excitation power of 100 μW. In total, 100 spectra were collected for one data set from one single PSI complex, with an acquisition time of 1s per spectrum.

5.3 Results

5.3.1 Morphological and Optical Characterization

The exterior morphology of the AuNPs was characterised by SEM (Philips XL 30, Prof. Monika Fleischer group,University of Tübingen). Fig. 5.1 (a) displays the SEM image of AuNPs, showing that the particles exhibit arbitrary shapes with various sizes and random orientations. Some of them are relatively round while others are more elongated. Fig. 5.1 (b) shows a histogram of particle size distribution, which was obtained by using the "Analyze Particle" application of the ImageJ software. The size of the AuNPs varies in a range from 12 to 156 nm with an average size of 36 nm. The fitting curve overlaid on the particle size distribution histogram was fitted with a log-normal function. For optical characterization, the absorption spectra of AuNPs was collected by using an inverted microscope (Nikon Eclipse Ti-U) equipped with a spectrometer (Ocean Optics QE 6500), together with Ph.D. student Andreas Horrer at Prof. Dr. Monika Fleischer group, University of Tübingen. The absorption spectrum of AuNPs shows a broadband with an FWHM of $\sim$ 146.0 nm and peak position, which correspond to the occurrence of LSPR at $\sim 604.0 \pm 0.2$ nm. In order to assure an optimal coupling between trimeric PSI complexes and AuNPs and hence a maximum enhancement in fluorescence emission, the spectral overlap of the absorption spectrum of the AuNPs with the excitation wavelength, as well as, with the absorption and emission spectra of PSI is crucial. Therefore, the AuNPs were fabricated under controlled experimental conditions, including evaporation rate, gold film thickness, pressure, annealing temperature and timing to tune the LSPR in required wavelength domain. Fig. 5.2 shows a comparison of the absorption spectrum of the AuNPs (blue broken line) with the absorption spectrum (green), emission spectra at 77 K (magenta) and 293 K (red) of trimeric PSI from *T. elongatus*. The absorption spectrum of the AuNPs is broad and expanded up to near infrared region covering both, the excitation wavelength at 665 nm, as well as, the absorption and emission

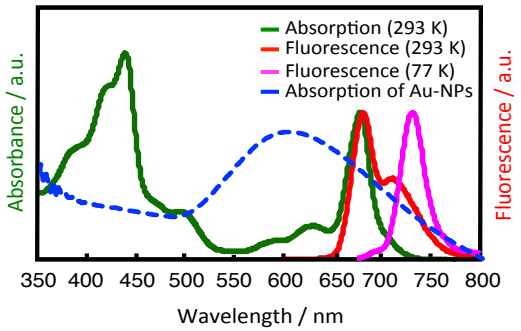

FIGURE 5.2: A comparison of absorption spectrum of AuNPs with the absorption spectrum (green), emission spectra at 77 K (magenta) and at 293 K (red) of trimeric PSI from Thermosynechococcus elongatus (*T. elongatus*). The absorption curve of AuNPs in blue is superimposed on top of the absorption and emission spectra of PSI. With rising temperature the fluorescence of PSI is shifted to blue.

spectra of trimeric PSI.

5.3.2 Spectral Analysis at Different Temperatures

To prepare the bio-nano hybrids, PSI complexes were coupled to the AuNPs by sandwiching the solution of PSI between a bare glass coverslip and the AuNPs, as displayed in Fig. 3.3. The concentration of PSI was kept low enough to ensure the presence of only single PSI complexes in the entire focal volume of the excitation. The hybrids were prepared outside and afterwards, were transferred to precooled cryostat to perform SMS different temperatures. The temperature of the cryostat is precisely adjusted by using an automatic temperature controller (Lake Shore, CX-1030-SD-HT, Model Number: 336), equipped with cernox sensor offering high sensitivity in the temperature range 0.3 - 420 K. By using home build confocal microscopy setup (explained in section: 3.1.1.1), the fluorescence emission spectra of individual uncoupled and AuNP-coupled trimeric PSI complexes were measured at temperatures of 1.6, 90, 190 and 250 K. The mean of all the spectra for each temperature and sample configuration are displayed in Fig. 5.3. The spectra were normalised to maximum intensity so that the spectral changes in the emission profiles of PSI due to variations in temperature and coupling with AuNPs can be compared. With increasing temperature from 1.6

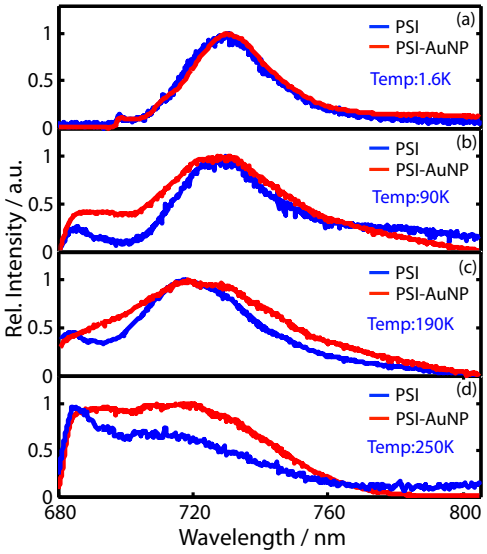

FIGURE 5.3: Averaged fluorescence emission spectra of all individual uncoupled (blue line) and AuNP-coupled (red line) PSI complexes measured at different temperatures. To compare the spectral modifications in the emission profiles of PSI due to changes in temperature and coupling with AuNPs, all the spectra are normalised to maximum intensity. Appearance of a shoulder in the shorter-wavelength region (688.0 ± 2.0 nm) for both uncoupled and AuNP-coupled PSI, increase in FWHM of the long-wavelength peak of PSI due to change of temperature and coupling with NPs and a blueshift of the emission maximum of the fluorescence spectra with the rise of temperature can be observed at respective temperatures.

- 250 K, we observed a blueshift in the peak position of uncoupled PSI - from 730.4 ± 0.5 to 718.5 ± 1.0 nm - and of AuNP-coupled PSI - from 731.1 ± 0.5 to 720.3 ± 1.0 nm. Additionally, a shorter-wavelength peak at ∼ 688.0 ± 2.0 nm appears for both uncoupled and AuNP-coupled PSI at higher temperatures. This peak is cut off somewhat in the experiments due to the used filter (HQ680LP, AHF Analysentechnik AG).

TABLE 5.1: Comparison of peak positions, spectral widths (FWHM) and enhancement factors for uncoupled and AuNP-coupled PSI at different temperatures.

Temperature	Peak Values / nm		FWHM / nm		Enhancement Factors		
	PSI	PSI-AuNP	PSI	PSI-AuNP	Min EF	Mean EF	Max EF
1.6 K	730.4 ± 0.5	731.1± 0.5	27.4 ± 0.4	27.1 ± 0.5	1.3	4.3	21.7
90 K	729.0 ± 0.5	727.3 ± 0.5	27.9 ± 0.7	41.2 ± 0.7	9.0	19.4	82.0
190 K	719.9 ± 0.5	720.7 ± 0.5	39.9 ± 0.5	49.7 ± 1.0	21.9	57.6	177.2
250 K	718.5 ± 1.0	720.3 ± 1.0	56.2 ± 0.7	58.6 ± 0.8	54.2	84.0	441.0

Both, the increase in temperature as well as coupling with AuNPs lead to an increase in spectral width (FWHM) of PSI emission spectra. For the average spectra of uncoupled PSI, the spectral width increases from 27.4 ± 0.4 nm at 1.6 K to 56.2 ± 0.7 nm at 250 K. However, due to coupling with AuNPs the width changes to 27.1 ± 0.5 nm at 1.6 K and 58.6 ± 0.8 nm at 250 K. Table 5.1 displays the comparison of the widths of average spectra of uncoupled and AuNP-coupled PSI at different temperatures.

Furthermore, in order to investigate heterogeneity of the individual spectra and the effects of temperature variations and AuNPs coupling on the shape of emission spectra of individual PSI complexes, the FWHM of each individual spectra (corresponding to single PSI complex) was determined at respective temperatures. Fig. 5.4 shows the corresponding scatter-plot of the FWHM of each individual spectra collected from coupled or uncoupled PSI complexs against the peak positions at respective temperatures. The

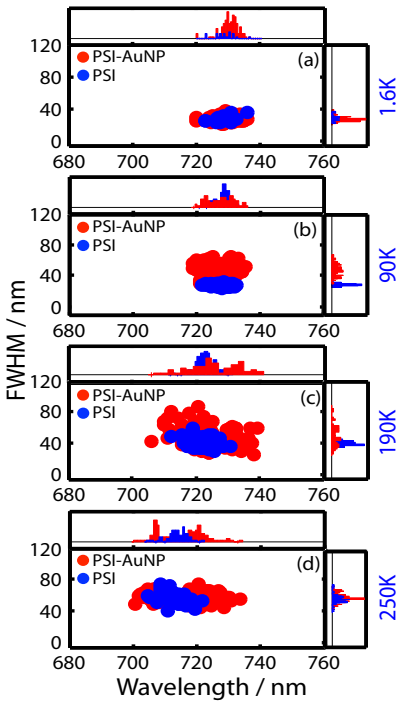

FIGURE 5.4: Scatter-plots of spectral widths (FWHM) vs. emission maxima of uncoupled PSI (blue) and AuNP-coupled PSI (red) at different temperatures. The histograms on the top display the emission maxima and those on the right displays the spectral widths. With rising temperature the peak positions of both uncoupled and AuNP-coupled PSI shift towards blue and the widths (FWHM) increases.

blue dots indicate the widths and peak positions of spectra from uncoupled PSI complexes while the red dots represent those of from AuNP-coupled PSI complexes. The histograms on top of each scatter-plot are showing the distribution of the peak positions and those on the right side are showing of the FWHM of the long-wavelength peaks. It is observed that at higher temperatures the spread in the peak positions of spectra from AuNP-coupled PSI complexes is higher, giving an indication of huge wavelength-dependent enhancement at higher temperatures. A broadening of the linewidths of both, uncoupled and AuNP-coupled PSI complexs, with the rise of temperature can also be noticed from these histograms. Scatter-plots clearly show that the AuNPs in vicinity and variations in temperature significantly altered the spectral shapes.

5.3.3 Temperature Dependent Enhancement Factor

To investigate the overall fluorescence enhancement as a function of temperature, all the experimental conditions, except temperature, were kept constant and emission spectra of the single coupled and uncoupled PSI complexes were collected. Keeping the experimental conditions similar is highly challenging. Several calibration measurements with a standard sample (TransFluoSpheres, Life Technologies GmbH) are needed to be performed on a regular basis during the measurements, to ensure high accuracy, same sensitivity and finally comparable datasets at the single molecule level. Fig. 5.5 display the histograms of all determined EFs for each individual PSI complex at the respective temperature. The EFs for the individual PSI complexes were determined based on the recorded spectra. For this purpose, the intensity counts of individual spectra of AuNP-coupled PSI were integrated after baseline corrections and compared to the average intensity counts of uncoupled PSI complexes. Based on this procedure an average EF=1 was obtained for all the uncoupled PSI samples at each respective temperature. The red bars represent the EF distribution of AuNP-coupled while the blue bars indicate the intensity distribution of uncoupled PSI complexes. The insets display the magnified intensity distributions of uncoupled PSI for better

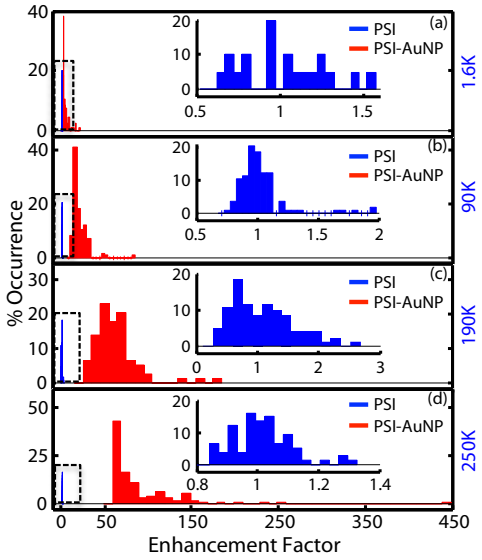

FIGURE 5.5: Histograms of EFs determined for PSI coupled to AuNPs (red) at different temperatures. Blue bars (in dashed boxes) represent the intensity distribution of uncoupled PSI. EFs show an increase with the rising temperature. Inset are the magnified intensity distributions of uncoupled PSI.

visibility. For AuNP-coupled PSI, on average the fluorescence was enhanced by 4.3-fold at 1.6 K, with further increases to 19.4, 57.6 and 84.0-fold at 90, 190 and 250 K, respectively. Notably, for some individual PSI complexes, EFs up to 230, 250 and 441-fold were recorded (see Fig. 5.5). Average and individual EFs, along with the spectral linewidths of the average and individual spectra indicate inter- and intra-molecular heterogeneities.

The temperature-dependent mean EFs together with the widths of their distributions are displayed as green dots in Fig. 5.6, showing a rising trend with rising temperature. The determined EF(T) is a combination of the two effects, i.e., the initial fluorescence yield of PSI and spectral overlap between the absorption of AuNPs and emission of PSI. The spectral overlaps were calculated at each respective temperature. Compared to 1.6 K, the spectral overlap increased by 1.2, 1.5 and 2.0-fold at 90, 190 and 250 K, respectively. In order to show the contribution of both: the initial fluorescence yield and spectral overlap effects distinctly, the combined EFs (green dots) were divided by the spectral overlap factors at corresponding temperatures. The resultant EF(T) were merely assigned to the initial fluorescence yield effect

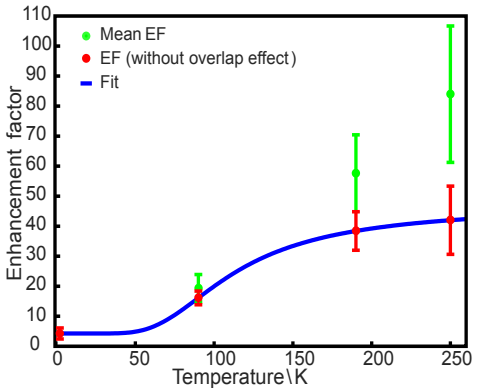

FIGURE 5.6: Temperature dependence of enhancement factor (EF). The green dots indicate the experimental values of mean EF with the corresponding error bars. The solid line shows the fitted curve. We divided the EFs by the overlap factor at corresponding temperature and fitted the resulting EFs (red dots) with the yield-function. Experimental values have shown a good agreement with the theoretical model.

and were plotted as red dots.

5.4 Discussion

The results presented in this chapter have shown a dramatic temperature dependency of (i) the intensity enhancement and (ii) the spectral shapes of the fluorescence of individual AuNP-coupled PSI complexes with respect to the uncoupled PSI complexes. The enhancement in fluorescence emission of the fluorophores by the metallic NPs in proximity has been a subject of intensive discussions in the recent years. Numerous factors, including spectral overlaps [129, 133, 234, 247], excitation wavelengths [67, 152, 247], geometrical properties of NPs [134, 136], mutual separations between fluorophores and NPs [67, 247, 266] and their relative orientations [249, 250] have been held responsible in literature for the enhancement of fluorescence emission. Moreover, the kinetic relaxation properties and the initial fluorescence QY of the fluorophores are also important parameters for MEF [138, 147, 267, 268]. It has been shown, both theoretically and experimentally, that the fluorophores with low initial fluorescence QY can gain a larger enhancement due to the metallic NPs in their close vicinity than those with high initial fluorescence QY [138, 147].

In the last chapter and in previous studies published under [100, 226, 228, 269], the fluorescence enhancement due to interactions of monometallic and bimetallic NPs with trimeric PSI complexes at cryogenic temperatures was studied and discussed in detail. In this chapter, now the study was extended to investigate the temperature dependence of MEF of individual pigment-proteins complexes coupled to AuNPs. The temperature dependence of MEF of a pigment-protein complex was the first study of its kind and never have been discussed before. The dependency of the determined EFs on temperature was discussed considering the two main responsible factors: (i) temperature dependence of initial fluorescence yield of PSI and (ii) temperature dependence of the spectral overlap.

5.4.1 Temperature dependence of initial fluorescence yield

The effect of temperature dependence of the initial fluorescence yield on MEF is crucial to understand the enormous increase in the fluorescence at higher temperatures. The initial fluorescence yield of a fluorophore, which is the ratio of radiative and non-radiative deactivation rates, is an important parameter that must be considered carefully to forecast the temperature dependent fluorescence enhancement induced by the coupling to a metallic NP. It has been reported that the initial fluorescence yield of PSI is highly temperature dependent and shows a $\sim$ 11-fold increase with the decrease of temperature from 295 to 4 K [97, 158, 270, 271], which can be explained by a reduction of the non-radiative deactivation rates. The observed huge increase in EF of AuNP-coupled trimeric PSI complexes with increasing temperature can, in part, be attributed to the low initial fluorescence yield of PSI at ambient temperatures. In order to estimate this effect, first the initial fluorescence yield of uncoupled PSI as a function of temperature can be simply given by [111]:

$$\Phi_0(T) = \frac{\Gamma_r^0}{\Gamma_r^0 + \Gamma_{nr}^0(T)}, \tag{5.1}$$

where $\Phi_0(T)$ denotes the temperature dependence of initial fluorescence QY without the metallic NPs in proximity, while Γ_r^0 and $\Gamma_{nr}^0(T)$ denotes the radiative and temperature dependent non-radiative decay rates, respectively. The temperature dependence of non-radiative rate can be approximated by adapting a simple model from [157] given by:

$$\Gamma_{nr}(T) = \frac{C}{T^{1/2}} \cdot e^{-E/T}, \tag{5.2}$$

where C and E are composed of thermodynamical constants, the activation energy for the non-radiative decay and the frequencies of the active vibrational modes. At ambient temperature, most of the excitation energy captured by the antenna system of PSI is efficiently transferred to the reaction centre pigment P700, resulting a light-induced charge separation. As a consequence, the initial fluorescence yield Φ_0 of PSI is very low, and hence, Γ_{nr}^0 very high. Lowering the temperature, more and more excitation energy gets trapped by the long-wavelength ("red") antenna pigments, which are also known as a red Chls or LWCs, and transfer of energy to the RC is partially blocked [88, 97]. There, a certain portion of the excitation energy from these LWCs then decays by fluorescence emission, increasing dramatically the fluorescence yield of PSI [158, 272].

As an additional factor influencing the QY, the excitation rate of PSI can be further increased by transferring energy from the nearby plasmonic NPs [152, 153, 227]. Within the native pigment-protein complex, the pigments are positioned at specific distances and orientations to assure an efficient EET and consequently the charge separation. If the AuNPs are located close to the PSI complex they are able to alter the EET pathways between the chromophores in PSI [100, 154, 269]. As a result, the existing EET pathways are disturbed and new pathways develop. This leads to the generation of new emission channels. Apparently, chromophores which in their native state do not fluoresce starts contributing in fluorescent and subsequently the overall fluorescence emission gets enhanced [100, 152]. The enhancement of the fluorescence emission of PSI by nearby metallic NPs is determined mainly by

three factors: increased excitation rate, modifications in the energy transfer pathways and enhanced emission rates based on the generation of new emission channels. However, the temperature dependence of the initial fluorescence yield of PSI is crucial to determine the enhancement in fluorescence emission. The parameter with most dominant temperature dependence with regards to MEF is the non-radiative decay rate. Thus, we can describe the MEF QY of PSI by:

$$\Phi_M(T) = \frac{\Gamma_r^M}{\Gamma_r^M + \Gamma_{nr}^M + \Gamma_{nr}^0(T)} \tag{5.3}$$

where $\Phi_M(T)$ denotes the modified QY due to the presence of AuNPs in proximity, while Γ_r^M and Γ_{nr}^M denote the modified radiative and non-radiative decay rates, respectively. Finally, the EF_{yield} for the fluorescence yield effect can be defined as a combination of excitation enhancement and change in QY by [111, 134, 138, 267]:

$$EF_{yield}\ (T) = M_{LF}\ .\frac{\Phi_{M(T)}}{\Phi_{0(T)}}, \tag{5.4}$$

where M_{LF} denotes the local field intensity EF. When induced by an incident light close to their plasmon resonance, the local field around the metallic NPs gets enhanced leading to an enhanced excitation process. The EF results from the modifications in both excitation and emission process and is inversely proportional to the initial fluorescence yield of a fluorophore. A fluorophore with a low initial fluorescent yield can be subject to a larger enhancement than the one with a high initial fluorescent yield. The huge increase of EF (250 K) compared to EF (1.6 K), therefore, partly can be attributed to a dramatic decrease of fluorescence QY of PSI with rising temperature and a strongly enhanced local field intensity M_{LF}.

5.4.2 Temperature dependence of spectral overlap

The second factor that was considered to discuss the temperature dependence of EF was spectral overlap. The spectral overlap of the laser excitation wavelength, absorption and emission spectra of a fluorophore with the absorption spectrum of the plasmonic NPs determines the coupling strength between the NPs and the fluorophores and thus the EF [67, 133, 234, 247]. In the study discussed in the previous chapter, a larger EF was found where the spectral overlap between laser excitation, emission spectra of PSI and absorption spectra of bimetallic NPs was stronger [269]. An optimal enhancement in fluorescence emission of the fluorophore has also been reported in literature for the strong overlap between the absorption spectra of the metallic NPs and fluorescence emission spectra of the fluorophore [129, 133, 234, 273]. The emission peak of PSI is redshifted too from the absorption peak of AuNPs, which is often considered critical for the larger enhancement of fluorescence emission [250, 274]. Upon rising the temperature from 1.6 to 250 K, the emission maximum of PSI shows a blueshift from $\sim$730.4 $\pm$ 0.5 nm to $\sim$718.5 $\pm$ 1.0 nm which clearly can be seen in Fig. 5.3. The strong temperature dependence of the emission maxima of PSI massively increases the spectral overlap with absorption of AuNPs as the temperature rises. At 250 K, the spectral overlap reached to maximum (2.0-fold). The increased spectral overlap means an increased coupling strength between AuNPs and PSI and consequently an increased MEF. Therefore, a part of the observed enormous increase in EF at higher temperatures was attributed to the enhanced spectral overlap.

Thus, the determined EF was described as a combination of the two contributions, i.e., initial fluorescence yield effect and spectral overlap effect. Fig. 5.6 displays both of the contributions distinctly as a function of temperature. The red dots fitted with the yield function represent the EF(T) only due to the contribution of initial fluorescence yield. The curve was simulated by a model function based on equations (5.1 - 5.4). This model fitted the experimental data well. The advantages of using this model lie in its

simplicity, as it only takes into account the already known parameters like temperature dependence of the initial fluorescence yield of PSI. Taking into account the overlap effect, the EF was influenced dramatically and nearly doubled at 250 K. This indicates that the temperature dependence of the QY of PSI and spectral overlap between absorption spectra of metallic NPs and emission spectra of PSI successfully explained our experimental values of EF(T). The huge increase in EF(250 K) compared to EF(1.6 K), therefore, was attributed to a dramatic decrease of initial fluorescence QY of PSI and significant increase in spectral overlap with rising temperature.

5.5 Summary

In this chapter, the investigation was extended to temperature dependence of MEF of single trimeric PSI complexes from *T. elongatus*, coupled to monometallic NPs. The NPs were composed of gold only (AuNPs) and fabricated by following a single step thermal annealing procedure. The study was performed using SMS at 1.6, 90, 190 and 250 K. The modifications in the emission spectra of individual complexes at each temperature were investigated. Our measurements showed that the AuNP based fluorescence enhancement of PSI was substantially influenced by the temperature. The intensity and shape of the emission spectra showed a strong temperature dependence. With the rise of temperature, on average the fluorescence was enhanced by 4.3 (1.6 K), 19.4 (90 K), 57.6 (190 K) and 84.0 (250 K)-fold. However, for individual complexes, the EFs even up to 230, 250 and 441-fold were observed. The spectral widths of all the individual spectra were calculated at each respective temperature. It was found that the spectral widths broaden continuously with the rise of temperature, showing a strong temperature dependence of the shape of emission spectra. In addition, a strong blueshift in the peak position of both uncoupled and AuNP-coupled PSI complexes was witnessed. The blueshift is presumably caused due to phase transition of the sample from solid to liquid (frozen to melted) in the temperature region between 180 - 220 K. The huge increase in EFs was

explained considering the initial fluorescence yield of PSI, excitation rate enhancement, alteration of energy transfer pathways, appearance of new emission channels and increased spectral overlap. It was shown that a simple rate model which takes into account only the already know properties like, the temperature dependence of the initial fluorescence yield of PSI and spectral overlap between the fluorescence emission of PSI and absorption of AuNPs, is able to explain the observed temperature dependence of EF. The gained better understanding of the remarkable fluorescence enhancement of AuNP-coupled PSI at higher temperatures will help to better understand the mechanisms of MEF for complex multi-chromophore systems in general.

6

Site-Specific Protein Binding

Proteins bound at the specific sites of metallic nanostructures can support in-depth understanding of the basic interaction mechanism(s) between protein and metal NP. In the study presented in this chapter, the attempts were made to develop an approach for binding the desired proteins (e.g., PSI) at specific sites on gold substrates. SAMs were formed by adsorption of alkanethiols on a gold substrate and patterned by exposure to UV light. Different characterization techniques, e.g., contact angle measurement, XPS, SEM and He-Ion microscopy were used to analyse the formation and photopatterning of the SAMs. Protein immobilisation was examined by using fluorescent microscopy. Efforts were made to achieve homogenous and site-specific binding.

6.1 Background

Protein immobilization has established its importance in numerous areas incorporating drug screening, biological engineering, protein microarrays, medical diagnostics and tissue engineering [275–277]. Different approaches like physisorption, covalent adsorption, and bioaffinity immobilisation are usually used to adsorb protein in ordered or disordered orientation on solid surfaces [276, 278, 279]. An approach of forming SAMs of species with reactive functionalized end groups on Au surfaces have been conventionally used for the site-specific attachment of the target proteins [279–283]. "SAMs are ordered molecular assemblies formed by the adsorption of an active surfactant on a solid surface" [284]. The SAMs because of their advantages like: easy tailoring of the interfacial properties of surfaces, controlled tuning of the functionality of organic thin films by simple modifications of the end groups, and the ability of the thiols to assemble in ordered and highly oriented manner, are highly suitable as bio-interface for adsorption of proteins [279]. Because of their high affinity for metal surfaces SAMs of alkanethiols formed onto the surfaces of Au have been most extensively studied and employed for electronic applications [285].

Interaction of the proteins with the metallic NPs, on the other hand, also have attracted a lot of attention in the last decades. Because of the ability of plasmonic NPs to achieve extreme light concentration at the nanometer scale, the hybrids of protein-NPs have propelled their use for optoelectronics, photoelectrochemical cells and nano-biosensing devices etc., [40, 48–50, 286]. PSI, a key component of photosynthetic apparatus responsible for light-induced electron translocation [287] is well known for its efficient light harvesting capability [104]. Due to its nano-sized dimensions, generation of 1 V photo-voltage and intrinsic conversion efficiency of 58 %, PSI is a promising candidate for molecular optoelectronics applications [40, 287–289]. However, the low absorption of solar light ($\sim$ 1 % per monolayer) by PSI limits its applications. Coupling the PSI with metallic NPs to enhance the photoinduced signals has been used to overcome this problem [47]. It

has been established that the metallic NPs depending on their shape and smaller size posses the optical properties which are strikingly different from those corresponding bulk metals [137, 138]. When the light of a specific frequency is illuminated, a collective coherent oscillation of the conduction band electrons on the surface of NP is induced [137, 290], resulting a strong electromagnetic field near the surface of the NPs [137, 138]. Compared to the single NP, it has been shown both, theoretically and experimentally, that the resulting electromagnetic field is highly intense between the gaps of two NPs [138, 291, 292]. These regions with the strongest electromagnetic field are known as hot spots. The enhancement in the fluorescence emission of the fluorophores coupled to plasmonic NPs has been found to be optimal at hot spots [130, 138, 293–295].

Therefore, the aim of this study was to develop an approach for placing PSI precisely at the specific sites (hot spots) of the metallic NPs and to investigate the corresponding effects of plasmonic interactions on optical properties of PSI. To accomplish this goal, an approach of forming mono-

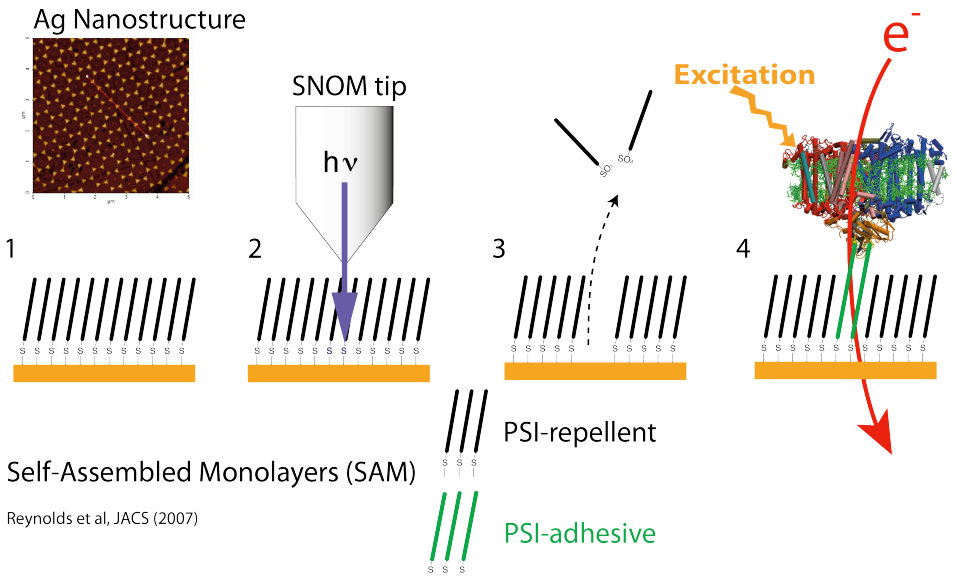

FIGURE 6.1: Schematic diagram showing the patterning of protein-resistant SAMs by near-field illumination (1-2), and the subsequent addition of PSI-adhesive monolayers (3) and immobilization of PSI (4).

layers of thiols and patterning them with UV exposure through a SNOM tip was planned. The principle of the planned approach is shown in Fig. 6.1.

In the first step the aim was to coat the surface of nanostructures with a SAM of protein-resistant thiol followed by the removal of layer at specific sites using UV light through SNOM tip. In the third step the free regions were to be filled with PSI-adhesive SAM followed by the attachment of PSI. This approach was adopted as it was already successfully used by the Prof. Neil Hunter group (University of Sheffield, UK) to selectively bind the light-harvesting LH2 complex from *Rhodobacter sphaeroides* on gold surface. They achieved finely patterned surface with LH2 complexes attached at specific sites (Fig. 6.2) [282]. The successful site specific binding of LH2 complex was a motivation to follow the same procedure for attachment of the PSI which is also a membrane pigment-protein complex.

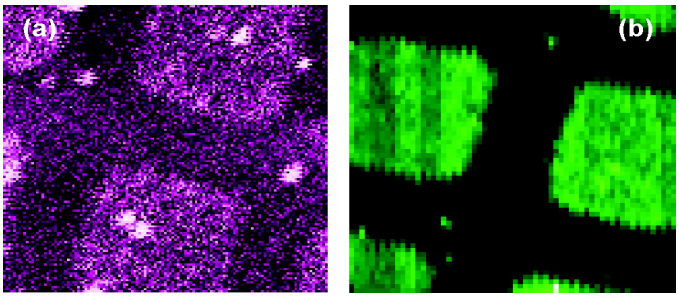

FIGURE 6.2: Fluorescence image of LH2 complex immobilized onto a photopatterned SAM. The image (a) obtained by a single photon counting APD while (b) obtained by a prism-based spectrograph. The bright squares are representing the high level of attachment, while the dark areas are showing the masked regions. Image size(a, b): 23.3 x 23.3 μm. The figure is taken from the Ref: [282].

The SAMs were formed by following an easiest and widely used protocol of immersing the gold substrate into the 1 mM solution of respective thiol. The advantage of this method is that it does not require any extravagant lab equipment. Since the long chain alkanethiols are more suitable to form a uniform and well-ordered SAMs as compared to short chain [296], therefore, the alkanethiols of long chains (with the property of repelling and adhering proteins, respectively) were chosen for the study and SAMs were formed as depicted in Fig. 6.3. Gold films were obtained on glass coverslips by vapour deposition of thin chromium and gold layers, respectively. Different characterization techniques including SEM, HIM, contact angle measurement,

XPS and fluorescent microscopy were used to investigate the formation of SAMs and site-specific binding of proteins and the corresponding results were discussed.

6.2 Experimental Section

Piranha Preparation

The piranha is used to clean all the glass wares for removing any organic residues. Different protocols are followed to prepare the piranha. In this study, however, it was prepared by mixing 3 parts of concentrated sulfuric acid (H_2SO_4) and 1 part of 30 % aqueous hydrogen peroxide (H_2O_2) [1].

Gold Substrate Prepration

Glass coverslips were rinsed copiously with deionized water and methanol (Uvasol, Merck Chemicals GmbH), respectively, and afterwards dried with a stream of N_2 or under laminar airflow workbench. Electron beam physical vapour deposition (EBPVD) technique was used to coat glass coverslips with gold. The choice of gold as a substrate was made considering the characteristics such as easy availability and preparation of films, exceptionally easy patterning, no oxidation effects, high-affinity binding with thiols and its strong compatibility with biological samples [297]. Edwards electron beam evaporator equipped with a high vacuum pump (Model: E2m-12), turbo pump (Model: TPH240, DN 100 ISO-K) and electron beam source (EB3) was used for evaporation. First, a 2 nm (20 Å) layer of chromium (Cr) was deposited on a glass coverslip as an adhesion promoter followed by a 20 nm (200 Å) thin film of gold in a sequence with a base pressure of (4×10^{-6}Torr). After removing from evaporation chamber, the cleaning of the fresh gold coated substrates was performed by methanol. The substrates were dried with N_2 stream prior to the formation of SAM.

[1] **Warning:** Piranha solution reacts ferociously so it should be handled with extra care. While preparing the piranha solution, it is preferred to first add H_2SO_4 followed by H_2O_2 with gentle stirring to avoid any explosion.

Preparation of SAMs

Formation of SAMs was carried out by using a well-known method shown in Fig. 6.3 [282, 298]. Prior to use, all the glass wares were cleaned with piranha solution. A 1 mM adsorption solution of the alkanethiol (i.e. 1H, 1H, 2H, 2H- perfluoro -1- octanethiol) exhibiting protein-resistant properties was prepared in methanol in a glass Petri dish. Gold coated substrates were cleaned with water and methanol, respectively, and were blown dried

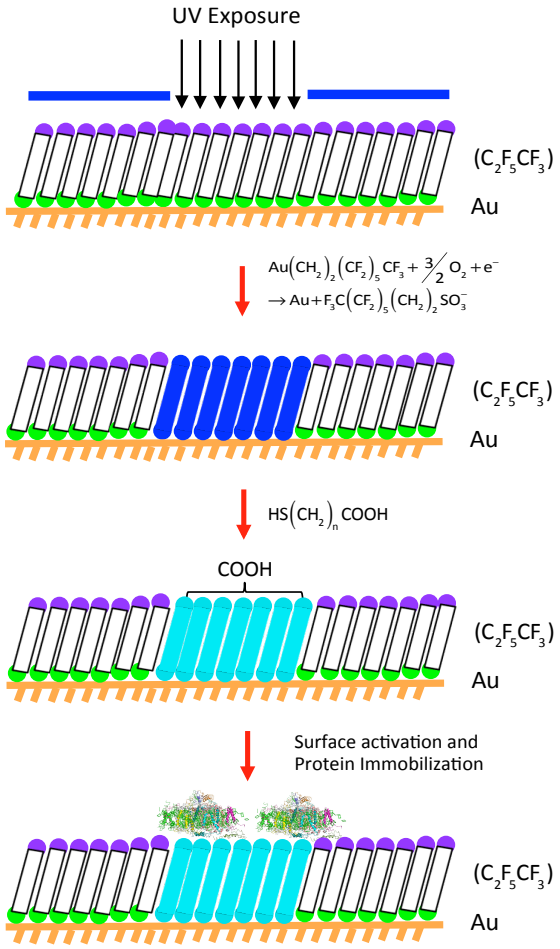

FIGURE 6.3: Schematic diagram showing the step by step the procedure for formation of SAM and photopatterning for site-specific protein immobilization on gold substrate. At first step Au substrate is placed in perfluorinated thiol ($C_2F_5CF_3$) solution for almost 18 hours. After formation of monolayer, it is selectively exposed to UV light through a mask and subsequently was placed in solution of 11- Mercaptoundecanoic acid (MUA) for formation of second SAM. Surface activation is carried out by EDC/NHS followed by the incubation in protein solution. The figure is adopted from Ref: [282].

with N_2 stream prior to the immersion in adsorption solution. Substrates were immersed in the solution for almost 18 hours at ambient temperature. Although a dense coverage of adsorbates is achieved within minutes, but to obtain the maximum density of molecules and to minimise the defects in SAM, a slow reorganisation process prolongs to hours [297]. After 18 hours a monolayer of protein-resistant alkanethiol was formed on the surface. Following the rinsing with distilled water, methanol and drying with N_2 stream, the substrate was photopatterned through UV exposure.

The photopatterning was conducted by exposing the monolayer to UV light through an aluminium mask for ∼17 minutes. A UV lamp (UVAHAND 250 GS, Honle UV Technology) covering the wavelength range of ∼320 nm - 400 nm was used as a UV light source. After exposing to UV light the substrate was immediately immersed for another 18 hours in 1 mM adsorption solution of contrasting thiol 11-Mercaptoundecanoic acid (MUA), which behaves as a protein adherent solution. The UV exposure of alkanethiols SAM in air leads to photochemical conversion of alkylthiolate adsorbates to alkylsulfonates [299–301].

$$\mathrm{Au-SR} + 3/2\mathrm{O_2} + \mathrm{e^-} \longrightarrow \mathrm{Au} + \mathrm{RSO_3^-}$$

Unlike alkanethiols, the alkylsulfonates adsorb to the gold surface very weakly [300]. As a result, when the sample is immersed in a solution containing a different thiol (i.e. MUA, a protein adherent thiol) the oxidation products in the exposed area get replaced by the new thiol through adsorption to the surface [301, 302]. While, during the exposure the original chemistry of alkanethiols in the masked region, was retained. The oxidation of thiols in UV exposed regions is associated with ozone produced by UV photolysis of O_2 [297, 303, 304]. All the steps were performed at ambient temperature. The selective photo exposure resulted in a patterned surface with protein repellent and adherent thiols at respective sites. The substrate was cleaned again with water, methanol and was blown dried with N_2 stream, respectively.

Surface Activation

In order to ensure the permanent interaction between proteins and the surface, the MUA surface was functionalized to form a reactive intermediate which is next coupled to a ligand. A familiar approach is the activation of carboxylic acid-terminated SAM by N-Hydroxysuccinimide (NHS) and subsequent reaction with 1-ethyl-3,3-dimethyl carbodiimide (EDCA) which yields the amide bonds [297, 305, 306]. A 20 mM aqueous solution of the NHS and EDCA was prepared in water and subsequently the patterned surface was incubated in solution for 30 minutes [282, 307]. As a result of the activation process, an active NHS ester monolayer is assembled and forms amide linkages by reacting with free amine groups from lysine residues on the protein [308].

Protein Immobilisation

The activated patterned surface was exposed to the protein solution. Green fluorescent protein (GFP) was used as a test protein as it is easily detectable under a fluorescent microscope. Different concentrations of GFP in water were tried initially, but 1 μL of GFP per 20 μL of tri-distilled water was found appropriate for the sample. To prepare the solution of the protein, 1 μL of GFP was added to 20 μL of tri-distilled water and was mixed completely with MS 3 digital shaker. NHS and EDCA activated surface was rinsed with methanol and dried with N_2 stream. An equal amount of GFP solution was placed on the surface and it was covered with parafilm and placed at room temperature for 45 minutes. After 45 minutes the parafilm was removed and the surface was gently washed with tri-distilled water couple of times and dried with N_2 stream. The immobilisation of the protein at specific sites was analysed by imaging the patterned surfaces using a confocal fluorescent microscopy (CLSM Leica SP2 AOBS) facility available at the centre for molecular biology of plants (ZMBP, University of Tübingen).

6.3 Results and Discussions

Following the method of SAMs formation, the attempt was made to prepare the surfaces which could resist the unwanted adsorption and encourage the adsorption at desired sites. SAMs were prepared following the procedure discussed above. Diverse experimental techniques were used to confirm the presence of a particular SAM and for analysis of corresponding photopatterning after UV exposure. The respective results are discussed in this section.

6.3.1 SEM and HIM

In order to analyse the photopatterning of the SAM with a terminal group ($C_2F_5CF_3$) after UV exposure, the SEM and HIM were applied. The SAM was prepared by following the procedure discussed above. The monolayer of only protein-repellent thiol ($C_2F_5CF_3$) was prepared and photopatterned by exposing half of the monolayer surface to UV light, while, masking the other half with aluminium foil. The diagram of the procedure followed to pattern the substrate before and after the exposure is displayed in Fig. 6.4. The patterned substrate was examined by the SEM and HIM. The resulting surface morphology is shown in Fig. 6.5. SEM was performed together

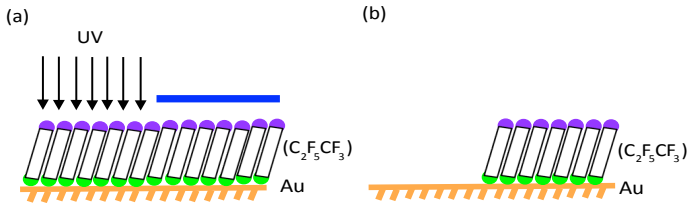

FIGURE 6.4: Sample prepared to analyse the photo patterning of the SAM. (a) Au substrate with a monolayer of $C_2F_5CF_3$ exposed to UV light through mask, (b) photo chemical oxidation of alkylthiolate to corresponding alkylsulfonates resulted the removal of weakly bound sulfonate species.

with Ph.D. student Julia Fulmes (Prof. Dr. Monika Fleischer group, University of Tüebingen) by using a conventional SEM (Philips XL 30). While,

HIM was performed in cooperation with Carl Zeiss AG, USA. A clear parting between the UV exposed and the unexposed part can be observed from both the SEM and HIM images. The bright regions in both the images correspond to the photo-irradiated region, whereas, the dark regions are the areas masked during UV exposure. In the dark region presence of a thiol monolayer can be witnessed very clearly, while, in the bright regions no indication of thiol layer was found. The monolayer of thiol appears very smooth and homogeneous in the masked region and in UV exposed region the layer was almost completely washed away. The small spheres or drops which are

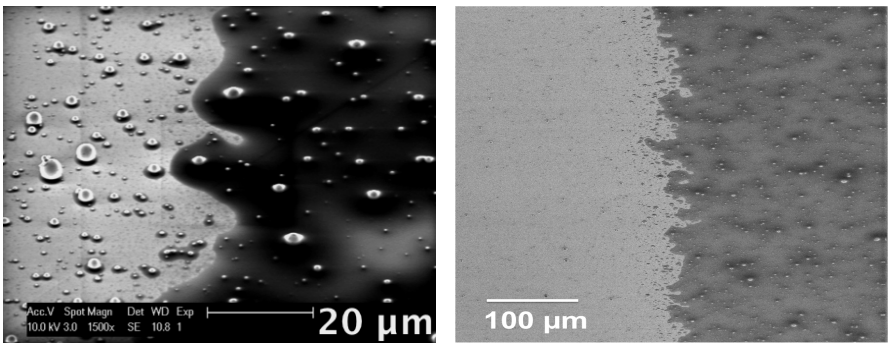

(a) SEM (b) HIM

FIGURE 6.5: Central part of the sample observed under (a) SEM and (b) HIM. Dark and bright regions show a clear difference between UV exposed and unexposed part. Bright regions are the areas where sample was exposed to UV light, as a result the thiol was removed while the dark areas show the presence of a thiol layer.

seen in both SEM and HIM images can be because of the contamination either during physical evaporation of Au on the glass substrate or during the preparations of SAM due to the weak purity of the solution of adsorbates. Thus, the results from SEM and HIM provides strong evidence of the successful formation of monolayer and photoinduced patterning. A complete photochemical oxidation of the $C_2F_5CF_3$ monolayer resulted rapidly after UV exposure and alkylthiolate adsorbates were photooxidized to the corresponding alkylsulfonates [299–301]. The weakly bound sulfonate species in the photo exposed region were removed by rinsing with water (a polar solvent) [297] and the underlying Au layer was uncovered. While the presence of thiol layer in the masked region demonstrates that the perfluorinated thiol

in this region retained its original chemistry even after UV exposure. Consequently, the layer of thiol was not removed from this specific area. Both, the characterization techniques, thus, verified the success of photoinduced decomposition of perfluorinated thiol molecules by direct photoirradiation in the air and subsequent oxidation of decomposed molecules.

6.3.2 Contact Angle

The formation of the SAM on a surface of the substrate alters the physical properties of the surface depending on the properties of the thiol used. In order to confirm the presence of the monolayer of a particular thiol, the wettability of the surface was measured through contact angle measurements. The procedure to measure the contact angle have been discussed in detail in section 3.1.5. After the formation the SAMs of both the thiols as discussed above, the substrate was cut in the centre to separate the UV exposed and unexposed parts. UV exposed part should have a monolayer of protein adherent thiol (MUA) on top, while in the unexposed part the protein repellent thiol (perfluorinated thiol) must have retained the original chemistry. To verify the presences of the monolayer of respective thiols on the respective side, the contact angle of the drop of water was measured by using drop analysis plugin of ImageJ software. Drops of water were placed on both i.e. the UV exposed and unexposed parts of the sample and using a camera the images were collected and contact angles were calculated (as discussed in section 3.1.5). Fig. 6.6 shows the drops of water on the respective surface of the sample with corresponding contact angles.

Fig. 6.6 (a) shows the contact angle measurement performed on the unexposed part of the sample. A very high contact angle of $\sim 137^{\circ}$ was found. While on UV exposed part of the sample (Fig. 6.6 (b)) the contact angle of water drop was $\sim 53^{\circ}$. Generally, a contact angle higher than 90° is an indication of the more hydrophobic surface while the one less than 90° shows hydrophilic surface [309]. Both of the surfaces showed different contact angles, which means different wettability of the surface, hinting the presence of two different surfaces. The part of the sample which was not exposed to UV

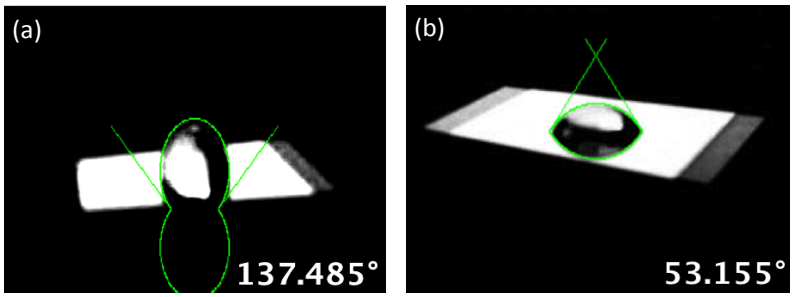

FIGURE 6.6: Formation of the SAMs was confirmed by contact angle measurement. (a) Protein repellent monolayer is hydrophobic resulting higher contact angle of water drop with the surface of substrate while protein adherent surface is hydrophilic resulting lower contact angle of water droplet.

light have shown a very high contact angle (>90°) showing that the surface is highly hydrophobic. This high hydrophobicity can be attributed to the composition of the protein-repellent thiol of a hydrophobic terminal group ($C_2F_5CF_3$). Perfluorinated thiols are well known to have superhydrophobic nature [282, 310]. The higher contact angle, therefore, shows that the first monolayer formed by the perfluorinated thiol which has protein-resistant properties has retained its original chemistry in the masked region. So, it was not affected when it was incubated in the solution of protein adherent thiol (MUA). While, on the other hand, the part of the sample which was exposed to UV light (Fig. 6.6 (b)) shows very low contact angle (<90°), suggesting the hydrophilic nature of the surface. The increased hydrophilicity is attributed to the composition of the protein-adherent thiol of the hydrophilic thiol group ($C_{10}COOH$). MUA monolayers are accepted to have hydrophilic nature [307, 311]. Therefore, it was assumed that in the exposed part of the sample the alkylthiolate adsorbates are converted into alkylsulfonates [299–301], which are very weakly bound to the gold surface. After incubation in the solution of contrasting adsorbate i.e., carboxylic acid-terminated thiol (MUA), the alkylsulfonate species were replaced by MUA [312]. A low contact angle measurement of UV exposed part of the sample, therefore, confirm the presence of only MUA on this side. Thus, through the contact angle measurements, it was presumed that the formation of SAM and

photopatterning was successful and resulted in the desired patterned substrate having the protein-repellent thiol layer in the masked region, while the protein-adherent thiol layer on UV exposed side.

6.3.3 X-ray Photoelectron Spectroscopy (XPS)

XPS, a surface analysis technique, was used to verify the presence of a specific thiol layers at specific sites by verifying the compositions of certain elements in the respective regions. XPS have been extensively used for surface analysis after the formation of SAM [297, 313, 314]. The composition of carbon, oxygen, sulfur and fluorine was detected and the results were analyzed. A standard source with twin anodes (Al Kα and Mg Kα) equipped with a Phoibos 100 hemispherical analyzer (SPECS) was used to perform the XPS measurements. XPS facility available at Prof. Dr. Thomas Chasse Group (University of Tübingen) was used together with Ph.D. student Mathias Glasser.

The SAM of both the thiols, i.e., perfluorinated thiol and MUA were prepared. The presence of MUA was anticipated to be in UV exposed region while monolayer of perfluorinated thiol was most likely to be in the masked region of the substrate. To measure the concentration of all the detectable elements in both, UV exposed and unexposed regions, broad survey scans were collected. The scan for the UV exposed region, where the presence of MUA is most likely, is shown in Fig. 6.7. Due to photoinduced decomposition and subsequent oxidation during UV exposure [282, 299, 300], the presence of perfluorinated thiol in this region was highly unlikely. The survey scan of the unexposed region is presented in Fig. 6.8. Both the surveys show F 1s, C 1s and O 1s, etc., lines very clearly. For being masked during UV exposure the perfluorinated thiol in this region was ought to preserve its original chemistry [282] and show the strong existence. Comparison of two surveys shows the obvious differences. The most significant difference between the two survey spectra is the concentration of fluorine showing a high concentration presence in unexposed region of the substrate. However,

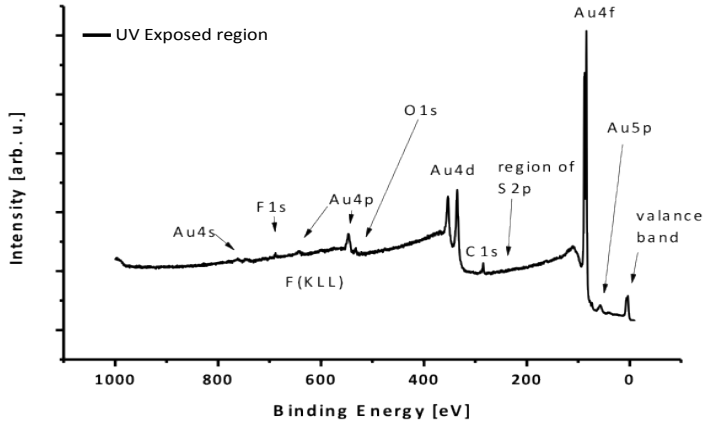

FIGURE 6.7: Survey of the side of the sample which after the formation of first monolayer of per fluorinated thiol was exposed to UV light and then was placed in solution of MUA.

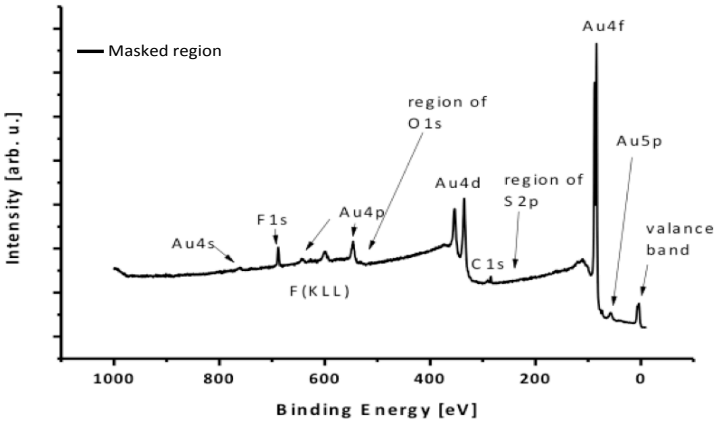

FIGURE 6.8: Survey of the side of the sample which was masked during the exposure to UV light and afterwards was transferred to the solution of MUA.

contrary to the presumptions, the survey did not show zero presence of fluorine in UV exposed region but an observable peak was spotted. Fig. 6.9 shows the XPS spectra of F 1s core level in the range 685 - 695 eV for both UV exposed and unexposed regions. The surface which was masked during UV exposure shows a strong dominance of the fluorine compared to its equivalent exposed surface. The dominant peak of fluorine was because of the presence of perfluorinated thiol in the region, which was not exposed to UV light. Thus, confirming that the perfluorinated thiol retained its original chemistry. A small concentration of fluorine witnessed on UV exposed region of the sample was not expected and was assigned to broadband UV lamp

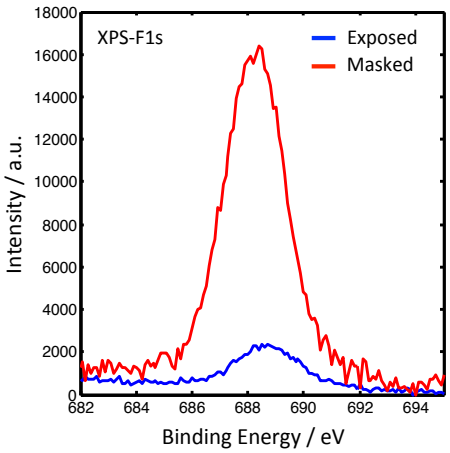

FIGURE 6.9: XPS F 1s core level lines measured from the regions covered by the SAM of perfluorinated thiol (red) and MUA (blue). Appearance of intense peak for fluorine in the masked region with respect to the exposed region confirms the presence of perfluorinated thiol monolayer in masked region. A small concentration of fluorine observed in the exposed region is attributed to the poor photooxidation of the thiolate headgroup to sulfonate.

used for the photochemical reaction with a wavelength range between 320 - 400 nm, instead of using a specific wavelength for exposure (as reported by [282, 300]). The broadband lamp did not result in complete photooxidation of the thiolate headgroup to a sulfonate. As a consequence, some of the molecules of perfluorinated thiol were still present in the region resulting the appearance of the fluorine peak.

A noticeable difference in the quantity of carbon and oxygen was also observed. Fig. 6.10 presents the high-resolution XP spectra for comparison of the C 1s core level (in the range 280 - 290 eV) and O 1s core level (in the range 530 - 536 eV) peaks. The quantity of both the carbon and oxygen was slightly higher in photo exposed regions than masked regions. The results acquired by the comparison of the quantity of carbon and oxygen were as per expectation. A certain amount of the oxygen is always expected due to either adventitious contamination or oxidation, however, the observed slightly higher concentration in exposed region is assigned to the presence of -COOH group. Relatively high concentration of carbon in exposed region compared to the masked one is justified by considering the higher number of carbon

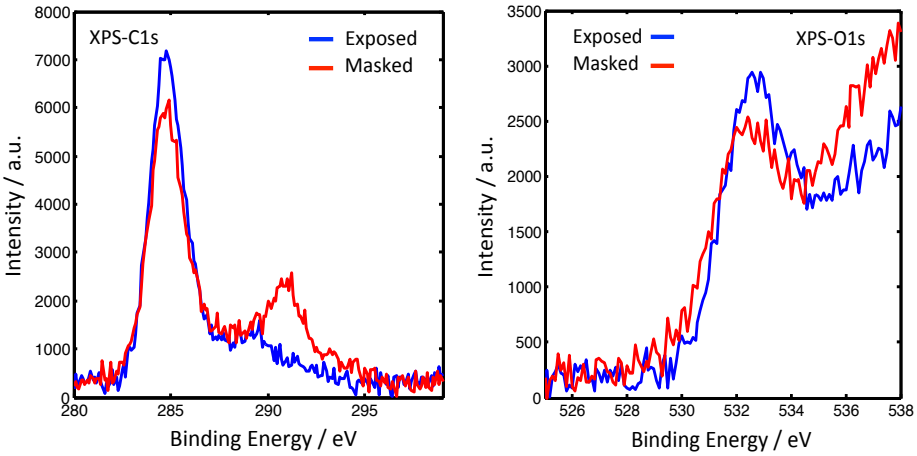

FIGURE 6.10: XPS C 1s (left) and O 1s (right) core level high-resolution spectra measured in ranges 280-290 eV and 530-536 eV, respectively. The higher concentration of both, the carbon and oxygen confirms the formation of the SAM of -COOH-terminated thiol in the exposed region.

atoms in MUA than perfluorinated thiol.

Thus, the XPS broad and high-resolution survey scans suggested that the first monolayer formed by self-assembly of perfluorinated thiol retained its original chemistry in the masked region, showing a dominant peak of F 1s. However, in the UV exposed region, contrary to the contact angle measurement, which showed a low contact angle hinting the presence of only MUA, the XPS results showed the presence of an observable amount of perfluorinated thiol in the exposed region too. This observation indicates that the photooxidation of the perfluorinated thiolate head group to the sulfonate was weak therefore the perfluorinated thiol was not washed completely from exposed region. The low concentration of carbon and oxygen in the masked region, however, shows the dominant presence of perfluorinated thiol.

6.3.4 Protein Immobilisation

Attachment of protein to the carboxylic acid-terminated thiol was achieved by following the similar procedures reported in the literature [280, 307, 315]. Initially GFP, because of its easy detection under the fluorescent microscope, was used as a model protein for site-specific protein immobilisation. The photopatterned surface was activated by incubation in the NHS and

EDCA solution and binding of protein was achieved. Investigation of the attachment of protein on the surface of the SAM was carried out using a commercially available confocal microscope. Fig. 6.11 shows the images of the surface topography. The region of the substrate with SAM favouring the attachment of protein is displayed in (a), while the region with protein-repellent SAM is displayed in (b). The fluorescence images of the resulting

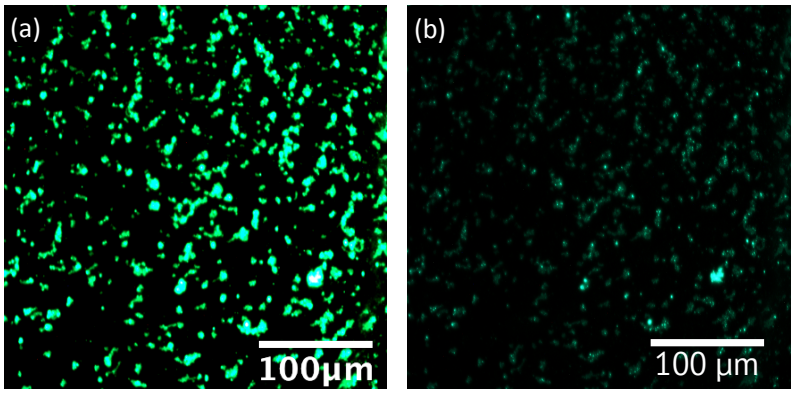

FIGURE 6.11: Site-specific protein immobilization on the surface with SAM of protein-adherent thiol (a) and protein-repellent thiol (b). The region of the surface with the thiol favouring the attachment of protein shows the adherence of GFP on the surface in the form of green spots. The region with protein repellent thiol shows a dark contrast with relatively less but significant presence of GFP.[2]

patterns show a good contrast between UV exposed and masked region. The bright fluorescence patches observed in UV exposed regions indicate the substantial attachment of GFP. In contrast the image of the masked region show less but a significant attachment of the GFP. The presence of GFP in UV exposed region was not very homogeneous (Fig. 6.11 (a)), showing an arbitrary distribution with some regions having less while the others having dense presence of GFP. Nearly similar results were observed for site-specific binding of PSI. However, contrary to GFP for PSI the attachment was nearly same on both, exposed and masked, regions of the surface (Fig. 6.12). The presence of PSI in UV exposed region appeared to be far less when compared to the presence of GFP in the similar region. While, in the masked

[2]The fluorescence images are taken only for comparison. The images are taken with high-definition 5.0-megapixel camera from Nikon (DS-Fi1) under same illumination conditions. The count rates are not accessible for this type of camera.

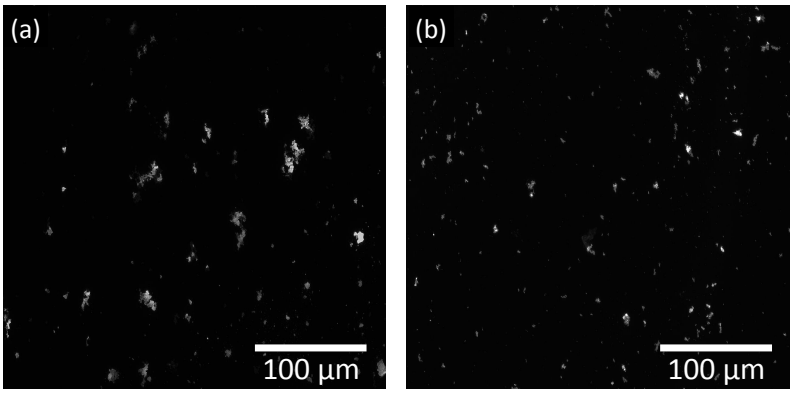

FIGURE 6.12: Site-specific immobilization of PSI on the surface with SAM of protein-adherent thiol (a) and protein-repellent thiol (b). Nearly equal levelled attachment was observed for both UV exposed and masked regions. The white spots in both the regions are showing the presence of PSI.

region the presence of PSI was nearly similar to GFP. These observations indicates that site-specific attachment of the proteins was partially successful for GFP. For PSI, on the other hand, the binding at selective sites did not work very successfully. An equal levelled attachment was observed on both UV exposed and masked region.

To investigate the reasons for the attachment of GFP and PSI on both sides of the substrate the crystal structures of GFP and PSI are drawn and the hydrophobic/hydrophilic regions and surface charge distribution patterns are displayed. Fig. 6.13 show the crystal structure of GFP molecule in cartoon style with chromophore responsible for the emission shown in red in centre (a), while same GFP molecule with separately displayed hydrophobic (blue) and hydrophilic (red) regions is shown in (b). In (c): electrostatic potential surface is shown with red indicates the negative charge regions while the blue shows positive charge regions. GFP appeared to have more hydrophilic regions outside. The electrostatic potential surface shows that GFP has both positive and negative charge regions on the surface. The patches of negative charge (red) are relatively more and bigger than positive (blue). Similarly, for monomeric PSI complex the crystal structure is shown in Fig. 6.14, where (a) shows the structure of PSI monomer with Chl *a* coloured yellow and carotenoids in black, while (b) shows same PSI

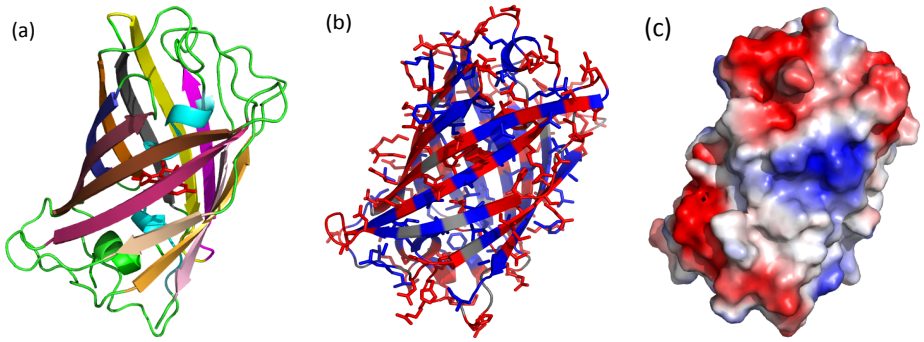

FIGURE 6.13: (a) GFP molecule drawn in cartoon style using a molecular visualization software Pymol. At the centre (in red) lies the chromophore responsible for the light emission. (b) GFP molecule with highlighted hydrophobic (blue) and hydrophilic (red) regions. (c) surface electrostatic potential (red for negative and blue for positive charges). From PDB: 1EMA.

monomer with hydrophobic regions displayed as blue and hydrophilic as red. In lower panel (c-e) electrostatic potential surfaces are shown as: side view (c), stromal view (d), and luminal view (e). The red patches are indicating the negative charge while the blue patches are the positive charges regions. The central domain of the PSI in the side view appears to be more neutral in charge. The stromal side of the PSI, however, have relatively more positive charge regions while the luminal side appeared more occupied by negative charge regions. Therefore it is speculated that may be due to the presence of both hydrophobic/hydrophilic and positive/negative charge regions on the surfaces of GFP and PSI they have attached on both sides of the substrate. The attachment on the UV exposed region probably is mainly due to electrostatic interactions between protein and the terminal carboxylate group, while on unexposed region due to hydrophobic interactions between hydrophobic surface and hydrophobic domains of proteins [282, 307].

The failure to resist unwanted attachment of both GFP and PSI in the non-specific region can be associated to the protein-repellent thiol. It is largely reported in the literature that in general, the proteins adsorb very rapidly and irreversibly onto most of the solid surfaces [282, 316–320]. Therefore, it is critical to identify a thiol to functionalize the surface which could resist the nonspecific protein attachment. Extensive studies had been carried out

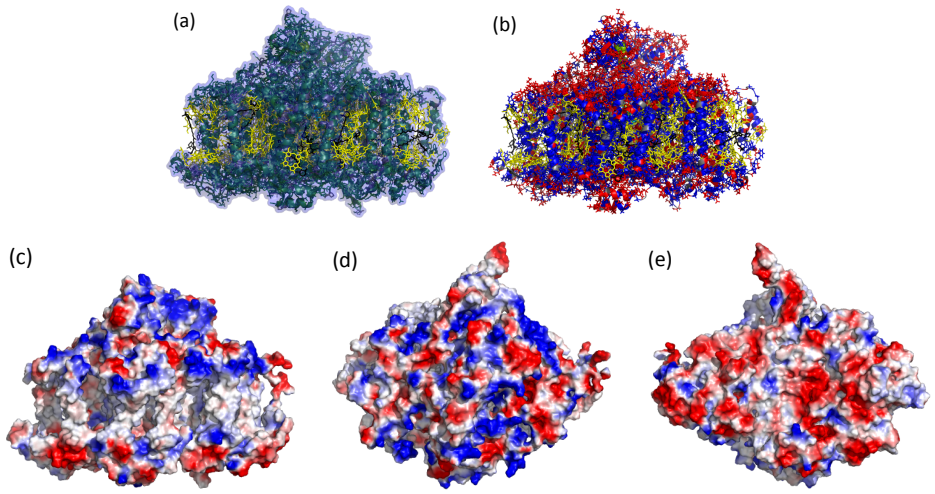

FIGURE 6.14: (a) Side view of monomer of PSI complex from *Thermosynechococcus elongatus* (*T. elongatus*) at 2.5 Å resolution with view direction parallel to the membrane plane. The Chl *a* are coloured in yellow while the carotenoids in black. (b) PSI complex with highlighted hydrophobic (blue) and hydrophilic (red) regions. (c-e) Surface electrostatic potential of PSI with (c) displaying side view of PSI, (d) stromal electrostatic surface and (e) luminal electrostatic surface. The red colors is for negative while the blue is for the positive charge. The figures are generated from PDB: 1JB0 by using molecular visualization software PyMol.

in last two decades to resist the adsorption of plasma proteins on gold and silver surface and a huge amount of literature is available in this regard [321–323]. In contrast a very less is known about the of membrane proteins. The mechanisms of protein adherence and repellence have been extensively debated. It is formulated that the force balance between steric repulsion, van der Waals attraction and hydrophobic interactions between protein and thiol altered surfaces, determines if the adsorption will occur or it will be resisted [321, 324]. The resistance to adsorption has been designated to the steric repulsion effect [321], while a combination of attractive forces is considered the cause of adherence [323]. Perfluorinated thiol was studied recently and appeared to be a very strong resistant against the binding of LH2 [282]. Considering its high-quality results against LH2, it was selected to resist the adsorption of PSI in this study. However, from the above mentioned observations, it was established that perfluorinated thiol did not prove beneficial for resisting the binding of GFP and PSI. For LH2, it was speculated that

the hydrophobic side of the LH2 was surrounded by the detergent molecules, which not only provide the hydrophilic exterior, but also provided the stabilisation to LH2 to avoid any of the reorganisation of its confirmation [282]. On the other hand, despite of low surface energy of fluorinated surface which should resist the adhesive interactions, the attachment of PSI and GFP can be explained considering the presence of hydrophobic exterior domains and reorganisation of their confirmation due to interaction with surface resulting a substantial hydrophobic interaction [325]. The hydrophobic interactions between the perfluorinated functionalized hydrophobic surface and the proteins consequences the enhanced attractive forces and subsequently enhanced adherence [324]. Depending on different factors, including the type of protein under investigation, environmental conditions like ionic strength, temperature and pH value and the type and wettability of the surface, the degree of proteins conformational reorganisation in their adsorbed state and consequently their efficiency of attachment or resistance to attachment fluctuates [325]. A thiol which fulfils the requirements of adherence or repellence of one protein may not be functioning equally same for a different protein even of similar structure. The partial repellence of the perfluorinated thiol against PSI and GFP in contrast to the strong resistance against LH2, thus, can be attributed to the different type of protein and effect of environmental conditions. It is noteworthy to mention here that we discussed the issue of partial adherence/repellence of PSI/GFP with Prof. Neil Hunter group (who successfully used these thiols for LH2) and it turned out that these thiols worked only for LH2 specifically. Therefore, for each individual protein, identifying a suitable thiol candidate with required properties of adherence and repellence is essential. This can be achieved only by surveying a number of the thiols one by one. That may turn highly expensive (because of the high cost of thiols) and time consuming.

In order to explain the inhomogenous attachment in UV exposed region, we considered the effect of the wavelength used for photo-patterning. It has been extensively reported in the literature that to achieve the optimum photooxidation of alkylthiolate SAM on Au substrate, a specific wavelength

should be used as a source of illumination [203, 276, 280, 299, 300, 316]. Norrod *et al.* and Zhang *et al.*, even claimed that a light source of wavelength 185 nm is prerequisite for oxidation to occur [299, 303, 304]. In the current study, instead of using a specific UV wavelength for irradiation, a broadband UV lamp with a wavelength ranging from 320 - 400 nm was used. This may have resulted in the poor photooxidation of alkyl thiols to sulfonate species. Consequently, the alkylthiolate adsorbate was not completely converted to alkylsulfonates and some of the perfluorinated thiol molecules were still present on the UV exposed region. This unwanted presence of perfluorinated thiol may have resisted the homogenous adherence of proteins and thus the in-homogenous attachment of proteins may have emerged.

This study thus revealed that perfluorinated thiol is not an ideal candidate to resist the adherence of PSI or GFP in the unwanted region. A vast amount of literature has proved that Oligo (ethylene glycol) (OEG)-terminated ($C_{11}(OEG)_3$) thiols are strongly resistant to adherence of plasma protein [203, 316, 322, 323]. Therefore, in future it will be worthwhile to probe these thiols for membrane proteins also. Additionally, for site-specific immobilization, the denaturation of PSI also needs to be considered. The aim of the study was to develop a method where PSI could be adsorbed at a specific site of NPs and SMS could be carried out. However, for binding the protein after photopatterning a 45 - 60 mins treatment under lab conditions is necessary to achieve a dense protein adsorbance. This may result in the light and heat-induced denaturation of PSI, affecting its fluorescence properties [325, 326]. Therefore, to avoid the denaturation, a strategy needs to be developed which do not require any long treatments under ambient conditions for attachment. One possible approach can be to prepare a SAM of ($C_{11}(OEG)_3$) thiol and after patterning it with specific UV light using a suitable linker to attach PSI directly to Au surface (as shown in Fig. 6.15).

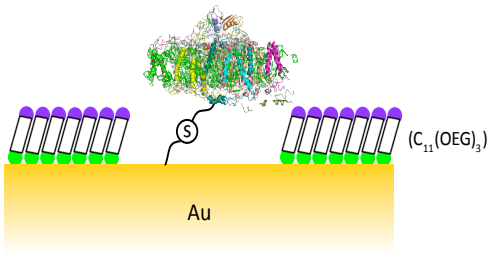

FIGURE 6.15: A possible approach to bind the PSI at specific sites on Au surface.

6.4 Summary

To summarize, it was tried to develop a method for controlled immobilization of PSI at the specific sites of Au substrate. In this regard, an approach of forming SAMs to bind the proteins at wanted sites and resist the binding at unwanted sites was adopted. A perfluorinated thiol and MUA were used as a protein repellent and adherent surfaces, respectively. Glass coverslips were coated with gold using physical vapour deposition and patterned surfaces for site-specific attachment of protein were prepared by using a three step process. In the first step, a SAM of perfluorinated thiol was formed by incubating the gold coated glass coverslip in 1 mM solution of the thiol for 18 h. Afterwards, the surface was patterned by photolithography using a broadband UV lamp. The sample was then incubated in MUA solution for another 18 h. A patterned surface with protein adherent thiol in UV exposed region and protein repellent thiol in unexposed region was obtained. Immobilization of both, GFP and PSI, was investigated. GFP was used as a model protein as it is easily detectable under fluorescent microscope. It was observed that perfluorinated thiol did not prove a strong repellent for both GFP and PSI. As a noticeable amount of both GFP and PSI was attached at nonspecific binding sites. MUA, on the other hand, to some extent partially fulfilled its objective and resulted significant adherence at the specific sites. However, the adherence was inhomogeneous and not very dense with certain hollow patches (particularly for PSI). It is speculated that because of the presence of both hydrophilic/hydrophobic and positive/negative charge

regions on the surface of the proteins, they attached on both wanted and unwanted sides through electrostatic and hydrophobic interactions.

Different characterization and analysis techniques were used to examine the formation of SAMs, photopatterning, and attachment of proteins. Through XPS surveys, it was found that the perfluorinated thiol molecules were also present in UV exposed regions. Therefore, the inhomogeneous binding with hollow patches in MUA covered regions was assigned to the undesired presence of perfluorinated molecules. It was presumed that a broadband UV light was not successful in providing an optimal photochemical oxidation of alkylthiolate adsorbates. As a consequence, some of the perfluorinated thiol molecules were still present in the UV exposed region and resisted the homogenous adherence of the proteins. Therefore, it is essential to use a specific UV wavelength to thoroughly photo oxidise the perfluorinated thiol and achieve a homogenous binding of protein. To prevent the binding of PSI at unwanted region needs a specific thiol with particular PSI repellent behaviour. Perfluorinated thiol, which proved a strong resistor to the binding of LH2 complexes [282], did not succeed to prevent the binding of GFP and PSI. A significant amount of these proteins, presumably due to hydrophobic interactions, was attached on the surface of perfluorinated thiol. Since every thiol has a specific behaviour against specific protein species. One thiol which is suitable for repellence (or adherence) of one specific protein is not bound to have a similar behaviour against other species too. It turned out that perfluorinated thiol was suitable specifically to resist the binding of LH2. Thus, it was concluded that an extensive study, which involves testing a number of thiols with protein repellent (or adherence) properties is needed to find a suitable candidate to resist (or adhere) PSI.

7

Conclusion

This work demonstrates the potential of the metallic NPs to increase light-harvesting in photosynthetic complexes (PSI). Different types of the metallic NPs (mono and bimetallic) were employed and their effects on optical properties of PSI were studied at single molecule level. To this aim, SMS tools were used to collect the spectral data from single isolated and metal NP-coupled PSI complexes and variations in the emission properties of PSI were analyzed to get new insights into the flow of the excitation energy. Measurements were performed at different temperatures between 1.6 - 250 K to comprehensively investigate the fluorescence properties of isolated and metal NP-coupled PSI complexes.

At first, bimetallic NPs with different compositions of Au and Ag were employed. Bimetallic NPs integrated with the synergistic effects of monometallic NPs exhibit unique physical and chemical properties which are superior

to those of their monometallic counterparts. For example, AgNPs are generally known to provide larger enhancement but are less stable in the biological environment. In contrast, AuNPs are highly stable with lower enhancement ability. Bimetallic fabrication approach, thus, offers an opportunity to cumulate the merits of both the AgNPs (larger enhancement) and AuNPs (chemical surface properties). For a deep understanding of the fundamental interaction mechanism(s) between metal NPs and PSI, it was convenient to use NPs with tailored optical properties. Therefore, the thermal annealing approach was adopted, as, it is simple, adaptable, low-cost way to fabricate large-scale substrates. It allows to easily tune the optical properties of NPs by controlling the size, shape and inter-particle distance via direct control of film thickness, annealing temperature and time, etc.

Three different nanostructured substrates were produced by coating double and triple metal layers and arbitrarily named as Au/Au, Ag/Au, and Au/Ag, respectively. The Au/Au substrate was fabricated by three successive evaporations of thin Au film where each two evaporations were separated by thermal annealing. The Ag/Au and Au/Ag substrates were fabricated by two consecutive evaporations of the respective metal separated by thermal annealing. Different metallic compositions and thicknesses of the layers resulted in different SPR for different substrates. These NPs were coupled to PSI complexes. The variations in the emission properties of the uncoupled and metal NP-coupled PSI were studied using SMS. An enhancement in the fluorescence emission of PSI was observed due to coupling with these NPs. Statistical analysis of the EFs showed that the NPs composed of Au/Au resulted in the maximum enhancement in fluorescence followed by Ag/Au and Au/Ag. On average the fluorescence was enhanced up to 4.4, 2.3 and 1.1-fold for Au/Au, Ag/Au, and Au/Ag NPs, respectively. For individual complexes, EFs up to 22.9 (Au/Au), 5.1 (Ag/Au) and 1.7 (Au/Ag) were observed. The large enhancement for Au/Au samples was assigned to stronger spectral overlap between absorption spectra of NPs and emission of PSI, while the least enhancement for Au/Ag was explained taking into account

the silver oxidation effect. The comparison of the emission spectra demonstrated a strong wavelength dependence of the enhancement in fluorescence. This was discussed considering the largely extended multichromophore composition of PSI.

In order to get a deep insight into the plasmonic interactions with PSI, the study was further extended to the temperature dependence of MEF of PSI. Monometallic NPs composed of Au only were used for the investigations. A single step thermal annealing strategy was followed. Glass coverslips were coated with a single Au layer, followed by thermal annealing under controlled experimental conditions. The measurements were performed at 1.6, 90, 190 and 250 K. The shape and intensity of the emission spectra showed a strong temperature dependence. On average the fluorescence was enhanced 4.3 (1.6 K), 19.4 (90 K), 57.6 (190 K) and 84.0 (250 K)-fold. However, for individual complexes an enormous increase in EFs up to 230, 250 and even 441-fold was observed. The remarkable increase in EFs at higher temperatures was discussed taking into account the low initial fluorescence yield of PSI, an increase in excitation rate, appearance of new emission channels due to altered EET pathways and increased spectral overlap between absorption spectra of AuNPs and emission spectra of PSI. The results were explained using a simple rate model which includes only the already know properties like the temperature dependence of the initial fluorescence yield of PSI and spectral overlap.

The precise and controlled placement of desired proteins is of growing interest for many fields. Placing PSI directly at positions with strong field enhancement (hotspots) can enhance its function in controlled manner. In the last part, therefore, SAM strategy was used for placement of PSI at specific sites. Different thiols were investigated to achieve a controlled binding of PSI on gold substrates. Perfluorinated thiol was used to resist the attachment of the protein while carboxylic acid-terminated thiol was used to achieve required binding. The monolayer of perfluorinated thiol was photopatterned by selective UV exposure. In the following step, a monolayer of carboxylic acid-terminated thiol was introduced to achieve a patterned surface with

specific regions for attachment of PSI. Different surface analysis techniques were used to examine the formation of SAM and photo-patterning of the monolayer. It was observed that the perfluorinated thiol is a weak resistor to PSI adsorption, as, a considerable nonspecific attachment of the protein was observed. While, carboxylic acid-terminated thiol proved a reasonably suitable candidate to adsorb PSI. The inhomogeneous attachment of the PSI at specific sites was assigned to the presence of perfluorinated thiol chunks in UV exposed region.

A

Scientific contributions

A.1 Journal Articles

- **Ashraf**, **I**.; Skandary, S.; Khaywah, M. Y.; Metzger, M.; Meixner, A. J.; Adam, P. M.; Brecht, M. Effects of Irregular Bimetallic Nanostructures on the Optical Properties of Photosystem I from Thermosynechococcus elongatus. Photonics, 2015, 2(3), 838-854.

- Metzger, M.; Konrad, A.; Skandary, S.; **Ashraf**, **I**.; Meixner, A. J.; Brecht, M. Resolution Enhancement for Low-temperature Scanning Microscopy by Cryo-immersion. Opt. Express, 2016, 24(12), 13023-13032.

- **Ashraf**, **I**.; Konrad, A.; Lokstein, H.; Skandary, S.; Metzger, M.; Djouda, J. M.; Maurer, T.; Adam, P. M.; Meixner, A. J.; Brecht, M.

Temperature Dependence of Metal-Enhanced Fluorescence of Photosystem I from Thermosynechococcus elongatus. Nanoscale, 2017, 9, 4196-4204.

- Skandary, S.; Müh, F.; **Ashraf**, **I.**; Ibrahim, M.; Metzger, M.; Zouni, A.; Meixner, A. J.; Brecht, M. Role of missing Carotenoid in Reducing the Fluorescence of Single Monomeric Photosystem II Core Complexes. Phys. Chem. Chem. Phys., 2017, 19, 13189-13194

- Metzger, M.; Riedel, D.; Konrad, A.; **Ashraf**, **I.**; Meixner, A. J.; Bucher, V.; Brecht, M. Low-cost Nephelometric Sensing. (manuscript in preparation)

A.2 Conference Contributions

- Light-Harvesting Processes, March 8 - 12, 2015 Banz Monastery (Germany): **Ashraf**, **I.**; Skandary, S.; Khaywah, M. Y.; Meixner, A. J.; Adam, P. M.; Brecht, M.: Plasmonic Interaction of Bimetallic Nanostructures with Photosystem I. (Poster Presentation)

- COST Action, Optical Nanospectroscopy I, March 24 - 28, 2014 Tübingen (Germany): **Ashraf**, **I.**; Skandary, S.; Konrad, A.; Fulmes, J.; Meixner, A. J.; Fleischer, M.; Brecht, M.: Site-specific Immobilization of Photosynthetic Proteins on Gold Nanostructures. (Poster Presentation)

Bibliography

(1) Chen, A. Y.; Deng, Z.; Billings A. N. Seker, U. O. S.; Lu, M. Y.; Citorik, R. J.; Zakeri, B.; Lu, T. K. *Nat. Mater.* **2014**, *13*, 515–523.

(2) Fox, J. D.; Capadona, J. R.; Marasco, P. D.; Rowan, S. J. *J. Am. Chem. Soc.* **2013**, *135*, 5167–5174.

(3) Kim, J. J.; Lee, Y.; Kim, H. G.; Choi, K. J.; Kweon, H. S.; Park, S.; Jeong, K. H. *Proc. Nat. Acad. Sci. U.S.A.* **2012**, *109*, 18674–18678.

(4) Kim, J. J.; Lee, J.; Yang, S. P.; Kim, H. G.; Kweon, H. S.; Yoo, S.; Jeong, K. H. *Nano Lett.* **2016**, *16*, 2994–3000.

(5) Spitzer, D.; Cottineau, T.; Piazzon, N.; Josset, S.; Schnell, F.; Pronkin, S. N.; Savinova, E. R.; Keller, V. *Angew. Chem. Int. Ed.* **2012**, *51*, 5334–5338.

(6) Xiao, M.; Li, Y.; Allen, M. C.; Deheyn, D. D.; Yue, X.; Zhao, J.; Gianneschi, N. C.; Shawkey, M. D.; Dhinojwala, A. *ACS Nano* **2015**, *9*, 5454–5460.

(7) *Introduction to Plant Physiology*, 4th Edition; Hopkins, W. G., Huener, N. P. A., Eds.; John Wiley and Sons, 1995.

(8) Badura, A.; Guschin, D.; Esper, B.; Kothe, T.; Neugebauer, S.; Schuhmann, W. *Electroanalysis* **2008**, *10*, 1043–1047.

(9) Graetzel, M. *Nature* **2001**, *414*, 338–344.

(10) Huber, R. C.; Ferreira, A. S.; Thompson, R.; Kilbride, D.; Knutson, N. S.; Devi, L. S.; Toso, D. B.; Challa, J. R.; Zhou, Z. H.; Rubin, Y.; Schwartz, B. J.; Tolbert, S. H. *Science* **2015**, *348*, 1340–1343.

(11) Kamat, P. V. *J. Phys. Chem. C* **2007**, *111*, 2834–2860.

(12) Kongkanand, A.; Tvrdy, K.; Takechi, K.; Kuno, M.; Kamat, P. V. *J. Am. Chem. Soc.* **2008**, *130*, 4007–4015.

(13) Meunier, C. F.; Yang, X. Y.; Rooke, J. C.; Su, B. L. *Chem. Cat. Chem.* **2011**, *3*, 476–488.

(14) Robel, I.; Subramaniam, V.; Kuno, M.; Kamat, P. V. *J. Am. Chem. Soc.* **2006**, *128*, 2385–2393.

(15) Wang, F.; Liu, X.; Willner, I. *Adv. Mater.* **2013**, *25*, 349–377.

(16) Wold, A. *Chem. Mater.* **1993**, *5*, 280–283.

(17) Youngblood, W. J.; Lee, S. A.; Maeda, K.; Mallouk, T. E. *Chem. Res.* **2009**, *42*, 1966–1973.

(18) Jordan, P.; Fromme, P.; Witt, H. T.; Klukas, O.; Saenger, W.; Krauss, N. *Nature* **2001**, *411*, 909–917.

(19) Duysens, L. N. M. *Photosyn. Res.* **1989**, *21*, 61–79.

(20) *Photosynthesis and Related Processes*; Rabinowitch, E. I., Ed.; Interscience Publishers: 1956; Vol. II.

(21) Emerson, R.; Chalmers, R. V.; Cederstrand, C. *Proc. Nat. Acad. Sci. U.S.A.* **1957**, *43*, 133–143.

(22) *Discoveries in Photosynthesis*; Govindjee, Beatty, J. T., Gest, H., Allen, J. F., Eds.; Springer: 2005; Vol. 20.

(23) Hill, R.; Bendall, F. *Nature* **1960**, *186*, 136–137.

(24) Duysens, L. N. M.; Amesz, J.; Kamp, B. M. *Nature* **1961**, *190*, 510–511.

(25) Fromme, P.; Mathis, P. *Photosynth. Res.* **2004**, *80*, 109 –124.

(26) Witt, H. T.; Mueller, A.; Rumberg, B. *Nature* **1961**, *191*, 194–195.

(27) Bengis, C.; Nelson, N *J. Biol. Chem.* **1975**, *250*, 2783–2788.

(28) Ford, R. C. *Biochim. Biophys. Acta* **1987**, *893*, 115–125.

(29) Newman, P. J.; Sherman, L. A. *Biochim. Biophys. Acta* **1978**, *503*, 343–361.

(30) Ogawa, T.; Obata, F.; Shibata, K. *Biochim. Biophys. Acta* **1966**, *112*, 223–234.

(31) Reed, D.; Clayton, R. K. *Biochem. Biophys. Res. Commun.* **1968**, *30*, 471–475.

(32) Roegner, S. E.; Muehlenhoff, U.; Boekema, E. J.; Witt, H. T. *Biochim. Biophys. Acta* **1990**, *1015*, 415–424.

(33) Vernon, L. P.; Shaw, E. R.; Ke, B. *J. Biol. Chem.* **1966**, *241*, 4101–4109.

(34) Wessels, J. S. C. *Biochim. Biophys. Acta.* **1966**, *126*, 581–583.

(35) Williams, J. C.; Glazer, A. N.; Lundell, D. J. *Proc. Nat. Acad. Sci. U.S.A.* **1983**, *80*, 5923–5926.

(36) Amunts, A.; Drory, O.; Nelson, N. *Nature* **2007**, *447*, 58–63.

(37) Badura, A.; Esper, B.; Ataka, K.; Grunwald, C.; Woell, C.; Kuhlmann, J.; Heberle, J.; Roegner, M. *Photochem. Photobiol.* **2006**, *82*, 1385–1390.

(38) Feifel, S. C.; Stieger, K. R.; Lokstein, H.; Lux, H.; Lisdat, F. *J. Mater. Chem. A* **2015**, *3*, 12188–12196.

(39) Feifel, S. C.; Lokstein, H.; Hejazi, M.; Zouni, A.; Lisdat, F. *Langmuir* **2015**, *31*, 10590–10598.

(40) Frolov, L.; Rosenwaks, Y.; Carmeli, C.; Carmeli, I. *Adv. Mater.* **2005**, *17*, 2434–2437.

(41) Giardi, M. T.; Pace, E. *Trends Biotechnol.* **2005**, *23*, 257–263.

(42) Koblizek, M.; Maly, J.; Masojidek, J.; Komenda, J.; Kucera, T.; Giardi, M. T.; Mattoo, A. K.; Pilloton, R. *Biotechnol. Bioeng.* **2002**, *78*, 110–116.

(43) Manocchi, A. K.; Baker, D. R.; Pendley, S. S.; Nguyen, K.; Hurley, M. M.; Bruce, B. D.; Sumner, J. J.; Lundgren, C. A. *Langmuir* **2013**, *29*, 2412–2419.

(44) Mershin, A.; Matsumoto, K.; Kaiser, L.; Yu, D.; Vaughn, M.; Nazeeruddin, M. K.; Bruce, B. D.; Graetzel, M.; Zhang, S. *Sci. Rep.* **2012**, *2*, 1–7.

(45) Nagy, L.; Magyar, M.; Szabo, T.; Hajdu, K.; Giotta, L.; Dorogi, M.; Milano, F. *Curr. Protein Pept. Sci.* **2014**, *15*, 363–373.

(46) Shing, W. L.; Heng, L. Y.; Surif, S. *Sensors* **2013**, *13*, 6394–6404.

(47) Carmeli, I.; Lieberman, I.; Kraversky, L.; Fan, Z.; Govorov, A. O.; Markovich, G.; Richter, S. *Nano Lett.* **2010**, *10*, 2069–2074.

(48) Atwater, H. A.; Polman, A. *Nat. Mater.* **2010**, *9*, 205–213.

(49) Kim, I.; Kihm, K. D. *Langmuir* **2009**, *25*, 1881–1884.

(50) Lee, S. E.; Lee, L. P. *Curr. Opin. Biotechnol.* **2010**, *21*, 489–497.

(51) Schuller, J. A.; Barnard, E. S.; Cai, W. S.; Jun, Y. C.; White, J. S.; Brongersma, M. L. *Nat. Mater.* **2010**, *9*, 193–204.

(52) Standridge, S. D.; Schatz, G. C.; Hupp, J. T. *J. Am. Chem. Soc.* **2009**, *131*, 8407–8409.

(53) Drexhage, K. H.; Fleck, M.; Kuhn, H.; Schafer, F. P.; Sperling, W. *Ber.Bunsenges. Phys. Chem* **1966**, *70*, 1179.

(54) Fleischmann, M.; Hendra, P. J.; McQuillan, A. J. *Chem. Phys. Lett.* **1974**, *26*, 163–166.

(55) Albrecht, M. G.; Creighton, J. A. *J. Am. Chem. Soc.* **1977**, *99*, 5215–5217.

(56) Jeanmaire, D. L.; van Duyne, R. P. *J. Electroanal. Chem.* **1977**, *84*, 1–20.

(57) Vukovic, S.; Corni, S.; Mennucci, B. *J. Phys. Chem. C* **2009**, *113*, 121–133.

(58) Aussenegg, F. R.; Leitner, A.; Lippitsch, M. E.; Reinisch, H. *Surf. Sci.* **1987**, *189/190*, 935–945.

(59) Das, P.; Metiu, H. *J. Phys. Chem.* **1985**, *89*, 4680–4687.

(60) Leitner, A.; Lippitsch, M. E.; Draxler, S.; Riegler, M.; Aussenegg, F. R. *Appl. Phys. B* **1985**, *36*, 105–109.

(61) Sokolov, K.; Chumanov, G.; Cotton, T. M. *Anal. Chem.* **1998**, *70*, 3898–3905.

(62) Weitz, D. A.; Garoff, S.; Hansen, C. D.; Gramila, T. J. *Opt. Lett.* **1982**, *7*, 89–91.

(63) Weitz, D. A.; Garoff, S.; Gersten, J. I.; Nitzan, A. *J. Chem. Phys.* **1983**, *78*, 5324–5338.

(64) Geddes, C. D.; Lakowicz, J. R. *J. Fluoresc.* **2002**, *12*, 121–129.

(65) Deng, W. Metal Nanostructure-Enhanced Fluorescence and its Applications in Bioassays and Bioimaging., Ph.D. Thesis, Macquarie University, Austrailia., 2011.

(66) Kruszewski, S.; Malak, H.; Ziomkowska, B.; Cyrankiewicz, M. *Proc. SPIE* **2006**, *6158*.

(67) Anger, P.; Bharadwaj, P.; Novotny, L. *Phys. Rev. Lett.* **2006**, *96*, 113002 1–4.

(68) Darvill, D.; Centeno, A.; Xie, F. *Phys. Chem. Chem. Phys.* **2013**, *15*, 15709–15726.

(69) Dubertret, B.; Calame, M.; Libchaber, A. J. *Nat. Biotechnol.* **2001**, *19*, 365–370.

(70) Lee, J.; Hernandez, P.; Lee, J.; Govorov, A. O.; Kotov, N. A. *Nat. Mater.* **2007**, *6*, 291–295.

(71) Malicka, J.; I., G.; Lakowicz, J. R. *Biochem. Biophys. Res. Commun.* **2003**, *306*, 213–218.

(72) Moal, E. L.; Fort, E.; Fort, S. L.; Cordelieres, F. P.; Aupart, M. P. F.; Ricolleau, C. *Biophys. J.* **2007**, *92*, 2150–2161.

(73) Slocik, J. M.; Tam, F.; Halas, N. J.; Naik, R. *Nano Lett.* **2007**, *7*, 1054–1058.

(74) Szalkowski, M.; Ashraf, K. U.; Lokstein, H.; Mackowski, S.; Cogdell, R. J.; Kowalska, D. *Photosynth. Res.* **2016**, *127*, 103–108.

(75) Frauenfelder, H.; Sliar, S. G.; Wolynes, P. G. *Science* **1991**, *254*, 1598–1603.

(76) Weber, G. *Adv. Protein Chem.* **1975**, *29*, 1–83.

(77) Smock, R. G.; Gierasch, L. M. *Science* **2009**, *324*, 198–203.

(78) Brecht, M.; Nieder, J. B.; Studier, H.; Schlodder, E.; Bittl, R. *Photosynth. Res.* **2008**, *95*, 155 –162.

(79) Hussels, M. Einzelmolekulspektroskopie an Photosystem-I-Komplexen und Bio-Nano-Hybridsystemen unter Kryogenen Bedingungen., Ph.D. Thesis, Eberhard Karls Universität Tübingen, Germany., 2012.

(80) Marriott, M. F. H.; Blankenship, R. E. *Annu. Rev. Plant Biol.* **2011**, *62*, 515–548.

(81) Blankenship, R. E. *Plant Physiol.* **2010**, *154*, 434–438.

(82) Liberton, M.; Page, L. E.; Dell, W. B. O.; Neill, H. O.; Mamontov, E.; Urban, V. S.; Pakrasi, H. B. *J. Biol. Chem.* **2013**, *288*, 3632–3640.

(83) Nelson, N.; Ben-Shem, A. *Nat. Rev. Mol. Cell Biol.* **2004**, *5*, 1–13.

(84) Berg, J. M.; Tymoczko, J. L.; Stryer, L., *Biochemistry*, 5th; W. H. Freeman: 2002.

(85) Lodish, H.; Berk, A.; Zipursky, S. L., *Molecular Cell Biology*, 4th; W. H. Freeman: 2000.

(86) Grotjohann, I.; Fromme, P. *Photosyn. Res.* **2005**, *85*, 51–72.

(87) Karapetyan, N. V.; Holzwarth, A. R.; Roegner, M. *FEBS Lett.* **1999**, *460*, 395–400.

(88) Schlodder, E.; Hussels, M.; Cetin, M.; Karapetyan, N. V.; Brecht, M. *Bioch. Biophys. Acta* **2011**, *1807*, 1423–1431.

(89) Gobets, B.; van Grondelle, R. *Biochim. Biophys. Acta* **2001**, *1507*, 80–99.

(90) Fromme, P.; Jordan, P.; Krauss, N. *Biochim. Biophys. Acta, Bioenerg.* **2001**, *1507*, 5–31.

(91) Ben-Shem, A.; Frolow, F.; Nelson, N. *Nature* **2003**, *426*, 630–635.

(92) Ben-Shem, A.; Frolow, F.; Nelson, N. *Photosyn. Res.* **2004**, *81*, 239–250.

(93) Nelson, N.; Yocum, C. F. *Annu. Rev. Plant Biol.* **2006**, *57*, 521–565.

(94) Anna, J. M.; Ostroumov, E. E.; Maghlaoui, K.; Barber, J.; Scholes, G. D. *J. Phys. Chem. Lett.* **2012**, *3*, 3677–3684.

(95) Bjorn, L.; Papageorgiou, G. C.; Blankenship, R. E.; Govindjee *Photosynth. Res.* **2009**, *99*, 85–98.

(96) Schlodder, E. *Photosynth. Res.* **2009**, *101*, 93–104.

(97) Wittmershaus, B. P.; Woolf, V. M.; Vermaas, W. F. J. *Photosyn. Res.* **1992**, *31*, 75–87.

(98) Grondelle, R.; Dekker, J. P.; Gillbro, T.; Sundstrom, V. *Biochim. Biophys. Acta* **1994**, *1187*, 1–65.

(99) Schlodder, E.; Shubin, V. V.; El-Mohsnwy, E.; Rogner, M.; Karapetyan, N. V. *Biochim. Biophys. Acta* **2007**, *1767*, 732–741.

(100) Brecht, M.; Hussels, M.; Nieder, J. B.; Fang, H.; Elsässer, C. *Chem. Phys.* **2012**, *406*, 15 –20.

(101) Karapetyan, N. V.; Bolychevtseva, Y. V.; Yurina, N. P.; Terekhova, I. N.; Shubin, V. V.; Brecht, M. *Biochemistry (Moscow)* **2014**, *79*, 213–220.

(102) Roemer S. Senger, H.; Bishop, N. I. *Bot. Acta.* **1995**, *108*, 80–86.

(103) Scholes, G. D.; Mirkovic, T.; Turner, D. B.; Fassioli, F.; Buchleitner, A. *Energy Environ. Sci.* **2012**, *5*, 9374–9393.

(104) Brettel, K.; Leibl, W. *Biochim. Biophys. Acta, Bioenerg.* **2001**, *1507*, 100–114.

(105) Forti, G.; Grubas, P. M. G. *FEBS Journal* **1985**, *186*, 149–152.

(106) Lakowicz, J. R., *Principles of Fluorescence Spectroscopy*, 3rd; Springer: 2006.

(107) Noomnarm, U.; Clegg, R. M. *Photosyn. Res.* **2009**, *101*, 181–194.

(108) Trnavsky, M. Surface Plasmon-Coupled Emission for Applications in Biomedical Diagnostics., Ph.D. Thesis, Dubline City University, Ireland., 2009.

(109) Albani, J. R., *Principles and Applications of Fluorescence Spectroscopy*; Blackwell: 2007.

(110) Stokes, G. G. *Phil. Trans. R. Soc. Lond.* **1852**, *142*, 463–562.

(111) Gill, R.; Tian, L.; van Amerongen, H.; Subramaniam, V. *Phys. Chem. Chem. Phys.* **2013**, *15*, 15734–15739.

(112) Kern, A. M.; Meixner, A. J.; Martin, O. J. F. *ACS Nano* **2012**, *6*, 9828–9836.

(113) So, P. T. C.; Dong, C. Y. *eLS* **2002**, 1–4.

(114) Emerson, R.; Arnold, W. *J. Gen. Physiol.* **1932**, *16*, 191–205.

(115) *Light-Harvesting Antennas in Photosynthesis*; Green, B. R., Parson, W. W., Eds.; Kluwer Academic Publishers (Springer), 2003.

(116) Schubert, A.; Beenken, W. J. D.; Stiel, H.; Voigt, B.; Leupold, D.; Lokstein, H. *Biophys. J.* **2002**, *82*, 1030–1039.

(117) Struempfer, J.; Sener, M.; Schulten, K. *J. Phys. Chem. Lett.* **2012**, *3*, 536–542.

(118) Clegg, R. M.; Sener, M.; Jee, G. *Proc. SPIE* **2010**, *7561*.

(119) Croce, R.; van Amerongen, H. *Nat. Chem. Biol.* **2014**, *10*, 492–501.

(120) Förster, T. *Naturwissenschaften* **1946**, *33*, 166–175.

(121) Dexter, D. L. *J. Chem. Phys.* **1953**, *21*, 836–850.

(122) Förster, T. *Annalen Der Physik* **1948**, *2*, 55–75.

(123) Förster, T. *Discuss. Faraday Soc.* **1959**, *27*, 7–17.

(124) Praveen, V. K.; Ranjith, C.; Bandini, E.; Ajayaghosh, A.; Armaroli, N. *Chem. Soc. Rev.* **2014**, *43*, 4222–4242.

(125) Nieder, J. B. Single-Molecule Spectroscopy on Pigment-Protein Komplexes., Ph.D. Thesis, Freie Universität Berlin, Germany, 2011.

(126) Xu, H.; Chen, R.; Sun, Q.; Lai, W.; Su, Q.; Huang, W.; Liu, X. *Chem. Soc. Rev.* **2014**, *43*, 3259–3302.

(127) Parson, W.; Nagarajan, V., *Light-Harvesting Antennas in Photosynthesis*; Kluwer Academic Publishers: 2003; Vol. 13.

(128) Chen, C.; Chu, P.; Bobisch, C. A.; Mills, D. L.; Ho, W. *Phys. Rev. Lett.* **2010**, *105*, 217402 1–4.

(129) Gill, R.; Tian, L.; Somerville, W. R. C.; Ru, E. C. L.; van Amerongen, H.; Subramaniam, V. *J. Phys. Chem. C* **2012**, *116*, 16687–16693.

(130) Kochuveedu, S. T.; Kim, D. H. *Nanoscale* **2014**, *6*, 4966–4984.

(131) Kuhn, S.; Hakanson, U.; Rogobete, L.; Sandoghdar, V. *Phys. Rev. Lett.* **2006**, *97*, 017402 1–4.

(132) Szunerits, S.; Spadavecchia, J.; Boukherroub, R. *Rev. Anal. Chem.* **2014**, *33*, 153–164.

(133) Chen, Y.; Munechika, K.; Ginger, D. S. *Nano Lett.* **2007**, *7*, 690–696.

(134) Kang, K. A.; Wang, J.; Jasinski, J. B.; Achilefu, S. *J Nanobiotechnology* **2011**, *9*, 1–13.

(135) Lee, J.; Lee, S.; Jen, M.; Pang, Y. *J. Phys. Chem. C* **2015**, *119*, 23285–23291.

(136) Zhang, J.; Fu, Y.; Chowdhury, M. H.; Lakowicz, J. R. *J. Phys. Chem. C* **2008**, *112*, 18–26.

(137) Eustis, S.; El-Sayed, M. A. *Chem. Soc. Rev.* **2006**, *35*, 209–217.

(138) Gill, R.; Ru, E. C. L. *Phys. Chem. Chem. Phys.* **2011**, *13*, 16366–16372.

(139) Myroshnychenko, V.; Rodriguez-Fernandez, J.; Pastoriza-Santos, I.; Funston, A. M.; Novo, C.; Mulvaney, P.; Liz-Marzan, L. M.; de Abajo, F. J. G. *Chem. Soc. Rev.* **2008**, *37*, 1792–1805.

(140) Huang, X.; El-Sayed, I. H.; El-Sayed, M. A., *Applications of Gold Nanorods for Cancer Imaging and Photothermal Therapy. In Cancer Nanotechnology*; Grobmyer, S. R., Moudgil, B. M., Eds.; Humana Press: 2010.

(141) Yasun, E.; Kang H. Erdal, H.; Cansiz, S.; Ocsoy, I.; Huang, Y. F.; Tan, W. *Interface Focus* **2013**, *3*, 1–9.

(142) Cobley, C. M.; Chen, J.; Cho, E. C.; Wang, L. V.; Xia, Y. *Chem. Soc. Rev.* **2011**, *40*, 44–56.

(143) Konrad, A.; Wackenhut, F.; Hussels, M.; Meixner, A. J.; Brecht, M. *J. Phys. Chem. C* **2013**, *117*, 21476–21482.

(144) Liu, M.; Pelton, M.; Guyot-Sionnest, P. *Phys. Rev. B* **2009**, *79*, 035418 1–5.

(145) Deng, W.; Xie, F.; Baltar, H. T.M.C. M.; Goldys, E. M. *Phys. Chem. Chem. Phys.* **2013**, *15*, 15695–15708.

(146) Khaywah, M. Y.; Jradi, S.; Louarn, G.; Lacroute, Y.; Toufaily, J.; Hamieh, T.; Adam, P. M. *J. Phys. Chem. C* **2015**, *119*, 26091–26100.

(147) Lakowicz, J. R.; Shen, Y.; D'Auria, S.; Malicka, J.; Fang, J.; Gryczynski, Z.; Gryczynski, I. *Anal. Biochem.* **2002**, *301*, 261–277.

(148) *Metal-Enhanced Fluorescence*; Geddes, C. D., Ed.; John Wiley and Sons: 2010.

(149) Aslan, K.; Gryczynski, I.; Malicka, J.; Matveeva, E.; Lakowicz, J. R.; Geddes, C. D. *Curr. Opin. Biotechnol.* **2005**, *16*, 55–62.

(150) Chen, H.; Ming, T.; Zhao, L.; Wang, F.; Sun, L. D.; Wang, J.; Yan, C. H. *Nano Today* **2010**, *5*, 494–505.

(151) Schneider, G.; Decher, G. *Nano Lett.* **2006**, *6*, 530–536.

(152) Czechowski, N.; Lokstein, H.; Kowalska, D.; Ashraf, K.; Cogdell, R. J.; Mackowski, S. *Appl. Phys. Lett.* **2014**, *105*, 043701 1–5.

(153) Kim, I.; Bender, S. L.; Hranisavljevic, J.; Utschig, L. M.; Huang, L.; Wiederrecht, G. P.; Tiede, D. M. *Nano Lett.* **2011**, *11*, 3091–3098.

(154) Zhang, J.; Fu, Y.; Lakowicz, J. R. *J. Phys. Chem. C* **2007**, *111*, 50–56.

(155) Byrdin, M.; Jordan, P.; Krauss, N.; Fromme, P.; Stehlik, D.; Schlodder, E. *Biophys. J.* **2002**, *83*, 433–457.

(156) Brecht, M.; Radics, V.; Nieder, J. B.; Bittl, R. *Proc. Natl. Acad. Sci. U. S. A.* **2009**, *106*, 11857–11861.

(157) Helenius, V.; Monshouwer, R.; Grondelle, R. *J. Phys. Chem. B* **1997**, *101*, 10554–10559.

(158) Palsson, L. O.; Flemming, C.; Gobets, B.; van Grondelle, R.; Dekker, J. P.; Schlodder, E. *Biophys. J.* **1998**, *74*, 2611–2622.

(159) Hirschfeld, T. *Appl. Opt.* **1976**, *15*, 2965–2966.

(160) Moerner, W. E.; Kador, L. *Phys. Rev. Lett.* **1989**, *62*, 2535–2538.

(161) Orrit, M.; Bernard, J. *Phys. Rev. Lett.* **1990**, *65*, 2716–2719.

(162) Moerner, W. E.; Fromm, D. P. *Rev. Sci. Instrum.* **2003**, *74*, 3597–3619.

(163) Moerner, W. E.; Shechtman, Y.; Wang, Q. *Faraday Discuss.* **2015**, *184*, 9–36.

(164) Moerner, W. E.; Orrit, M. *Science* **1999**, *283*, 1670–1676.

(165) *Handbook of Spectroscopy*, 2nd ed.; Gauglitz, G., Moore, D. S., Eds.; Wiley-VCH Verlag GmbH: 2014; Vol. 4, pp: 823-838.

(166) Moerner, W. E.; Dickson, R. M.; Norris, D. J. *Adv. At. Mol. Opt. Phys.* **1997**, *38*, 193–236.

(167) Rebane, K. K. *Chem. Phys.* **1994**, *189*, 139–148.

(168) Weiss, S. *Science* **1999**, *283*, 1676–1683.

(169) Basche, T.; Kummer, S.; Braeuchle, C. *Nature* **1995**, *373*, 132–134.

(170) Kaufmann, R.; Hagen, C.; Gruenewald, K. *Curr. Opin. Chem. Biol.* **2014**, *20*, 86–91.

(171) Yu, Z.; Barbara, P. F. *J. Phys. Chem.B* **2004**, *108*, 11321–11326.

(172) Yu, Z. W.; Liu, J.; Noda, I. *Appl. Spectrosc.* **2003**, *57*, 1605–1609.

(173) Brecht, M. *Mol. Phys.* **2009**, *107*, 1955–1974.

(174) Basche, T. *J. Lumin.* **1998**, *76*, 263–269.

(175) *Handbook of Biological Confocal Microscopy,* Pawley, J. B., Ed.; Springer Science and Business Media, 2006.

(176) Zondervan, R.; Kulzer, F.; Kolchenko, M. A.; Orrit, M. *J. Phys. Chem. A* **2004**, *108*, 1657–1665.

(177) Bernas, T.; Zarebski, M.; Cook, R. R.; Dobrucki, J. W. *J. Microsc.* **2004**, *215*, 281–296.

(178) Latychevskaia, T. Y.; Liang, K. K.; Hayashi, M. *J. Chin. Chem. Soc.* **2003**, *50*, 477–516.

(179) Tsien, R. Y. *Annu. Rev. Biochem.* **1998**, *67*, 509–544.

(180) Betzig, E.; Chichester, J. *Science* **1993**, *262*, 1422–1424.

(181) Schmidt, T.; Schuetz, G. J.; Baumgartner, W.; Grauber, H. J.; Schindler, H. *Proc. Nat. Acad. Sci. U.S.A.* **1996**, *93*, 2926–2929.

(182) Ha, T.; Enderle, T.; Chemla, D. S. *Phys. Rev. Lett.* **1996**, *77*, 3979–3982.

(183) Ha, T.; Glass, J.; Enderle, T.; Chemla, D. S.; Weiss, S. *Phys. Rev. Lett.* **1998**, *80*, 2093–2096.

(184) Edman, L.; Mets, U.; Rigler, R. *Proc. Natl. Acad. Sci. U.S.A* **1996**, *93*, 6710–6715.

(185) Rigler, R. *J. Biotechnol.* **1995**, *31*, 177–186.

(186) Rigler, R.; Mets, U.; Widengren, J.; Kask, P. *Eur. Biophys. J.* **1993**, *22*, 169–175.

(187) Goodwin, P. M.; Cai, H.; Jett, J. H.; Ishaug-Riley, S. L.; Machara, N. P.; Semin, D. J.; van Orden, A.; Keller, R. A. *Nucleosides and Nucleotides* **1997**, *16*, 543–550.

(188) Ibach, J.; Brakmann, S. *Angew. Chem. Int. Ed.* **2009**, *48*, 4683–4685.

(189) Michalet, X.; Weiss, S.; Jager, M. *Chem. Rev.* **2006**, *106*, 1785–1813.

(190) Hussels, M.; Konrad, A.; Brecht, M. *Rev. Scie. Instr.* **2012**, *83*, 123706 1–5.

(191) Fromme, P.; Witt, H. T. *Biochim. Biophys. Acta, Bioenerg.* **1998**, *1365*, 175–184.

(192) Buhr, E.; Senftleben, N.; Klein, T.; Bergmann, D.; Gnieser, D.; Frase, C. G.; Bosse, H. *Meas. Sci. Technol.* **2009**, *20*, 084025 1–9.

(193) Goldstein, J.; Newbury, D.; Joy D. Lyman, C.; Echlin, P.; Lifshin, E.; Sawyer, L.; Michael, J., *Scanning Electron Microscopy and X-Ray Microanalysis*, 3rd; Kluwer Academic/Plenum: 2003.

(194) Liu, F.; Wu, J.; Chen, K.; Xue, D. *Microscopy: Science, Technology, Applications and Education* **2010**, 1781–1792.

(195) Bell, D. C. *Microsc. Microanal.* **2009**, *15*, 147–153.

(196) Joens, M. S.; Huynh, C.; Kasuboski, J. M.; Ferranti, D.; Sigal, Y. J.; Zeitvogel, F.; Obst, M.; Burkhardt, C. J.; Curran, K. P.; Chalasani, S. H.; Stern, L. A.; Goetze, B.; Fitzpatrick, J. A. J. *Sci. Rep.* **2013**, *3*, 1–7.

(197) Hlawacek, G.; Veligura, V.; van Gastel, R.; Poelsema, B. *J. Vac. Sci. Technol. B* **2014**, *32*.

(198) Notte, J.; Ward, B.; Economou, N.; Hill, R.; Percival, R.; Farkas, L.; McVey, S. *AIP Conf. Proc.* **2007**, *931*, 489–496.

(199) Bell, D. C.; Lemme, M. C.; Stern, L. A.; Williams, J. R. *Nanotechnology* **2009**, *20*, 455301 1–5.

(200) Ward, B. W.; Notte, J. A.; Economou, N. P. *J. Vac. Sci. Technol. B* **2006**, *24*, 2871–2874.

(201) Morgan, J.; Notte J. Hill, R.; Ward, B. *Micros. Today* **2006**, *14*, 24–31.

(202) Van der Heide, P., *X-ray Photoelectron Spectroscopy: An Introduction to Principles and Practices*; John Wiley and Sons: 2012.

(203) Ahmad, S. A. A.; Wong, L. S.; ul Haq, E.; Hobbs, J. K.; Leggett, G. J.; Micklefield, J. *J. Am. Chem. Soc.* **2011**, *133*, 2749–2759.

(204) Ye, S.; Li, G.; Noda, H.; Uosaki, K.; Osawa, M. *Surf. Sci.* **2003**, *529*, 163–170.

(205) Watts, J. F.; Wolstenholme, J., *An Introduction to Surface Analysis by XPS and AES*; John Wiley and Sons: 2003.

(206) Rossi, A.; Elsener, B.; Spencer, N. D. *Spectrosc. Eur.* **2004**, 14–19.

(207) Lamour, G.; Hamraoui, A. *J. Chem. Educ.* **2010**, *87*, 1403–1407.

(208) Colorado, R.; Lee, T. R. *Langmuir* **2003**, *19*, 3288–3296.

(209) Kasalkova, N. S.; Slepicka, P.; Kolska, Z.; Svorcik, V., *Wettability and Other Surface Properties of Modified Polymers, Wetting and Wettability*; Aliofkhazraei, D. M., Ed., 2015.

(210) Drelich, J.; Chibowski, E.; Meng, D. D.; Terpilowski, K. *Soft Matter* **2011**, *7*, 9804–9828.

(211) Claxton N. S., F. T. J.; Davidson, M. W., *Encyclopedia of Medical Devices and Instrumentation*; Webster, J. G., Ed.; John Wiley and Sons: 2006.

(212) Meng, F.; Liao, B.; Liang, S.; Yang, F.; Zhang, H.; Song, L. *J. Membr. Sci.* **2010**, *361*, 1–14.

(213) Zhang, L.; Folkenberg, D. M.; Qvist K. B. Ipsen, R. *Int. Dairy J.* **2015**, *46*, 88–95.

(214) Conchello, J. A.; Lichtman, J. *Nat. Mathods* **2005**, *2*, 920–931.

(215) Smith, C. L. *Curr. Protoc. Neurosci.* **2001**, *56*, 2.2 1—13.

(216) Semwogerere, D.; Weeks, E. R., *Confocal Microscopy*; Encyclopedia of Biomaterials and Biomedical Engineering, 2005.

(217) Lagali, N., *Confocal Laser Microscopy - Principles And Applications in Medicine, Biology and the Food Sciences*; team, I. D., Ed.; InTech: 2013.

(218) Grzelczak, M.; Juste, J. P.; Mulvaney, P.; Liz-Marzan, L. M. *Chem. Soc. Rev.* **2008**, *37*, 1783–1791.

(219) Hu, J.; Wang, Z.; Li, J. *Sensors* **2007**, *7*, 3299–3311.

(220) Kimling, J.; Maier, M.; Okenve, B.; Kotaidis, V.; Ballot, H.; Plech, A. *J. Phys. Chem. B* **2006**, *110*, 15700–15797.

(221) Jia, K.; Bijeon, J. L.; Adam, P. M.; Ionescu, R. E. *Plasmonics* **2013**, *8*, 143–151.

(222) Lopatynskyi, A. M.; Lytvyn, V. K.; Nazarenko, V. I.; Guo, L. J.; Lucas, B. D.; Chegel, V. I. *Nanoscale Res. Lett.* **2015**, *10*, 1–9.

(223) Colson, P.; Henrist, C.; Cloots, R. *J. Nanomater.* **2013**, 1–19.

(224) Hulteen, J. C.; Treichel, D. A.; Smith, M. T.; Duval, M. L.; Jensen, T. R.; Van Duyne, R. P. *J. Phys. Chem. B* **1999**, *103*, 3854–3863.

(225) Haynes, C. L.; van Duyne, R. P. *J. Phys. Chem. B* **2001**, *105*, 5599–5611.

(226) Hussels, M.; Nieder, J. B.; Elsässer, C.; Brecht, M. *Acta Phys. Polo. A* **2012**, *122*, 269–274.

(227) Mackowski, S.; Wormke, S.; Maier, A. J.; Brotosudarmo, T. H. P.; Harutyunyan, H.; Hartschuh, A.; Govorov, A. O.; Scheer, H.; Brauchle, C. *Nano Lett.* **2008**, *8*, 558–564.

(228) Nieder, J. B.; Bittl, R.; Brecht, M. *Angew. Chem., Int. Ed.* **2010**, *49*, 10217–10220.

(229) Vuckovic, J.; Lonear, M.; Scherer, A. *IEEE J. Quant. Electron.* **2000**, *36*, 1131–1144.

(230) Anker, J. N.; Hall, W. P.; Lyandres, O.; Shah, N. C.; Zhao, J.; Van Duyne, R. P. *Nat. Mater.* **2008**, *7*, 442–453.

(231) Li, M.; Cushing, S. K.; Wu, N. *Analyst* **2015**, *140*, 386–406.

(232) Pelton, M.; Santori, C.; Vuckovic, J.; Zhang, B. Y.; Solomon, G. S.; Plant, J.; Yamamoto, Y. *Phys. Rev. Lett.* **2002**, *89*, 233602 1–4.

(233) Painter, O.; Lee, R. K.; Scherer, A.; Yariv, A.; O'Brien, J. D.; Dapkus, P. D.; Kim, I. *Science* **1999**, *284*, 1819–1821.

(234) Tam, F.; Goodrich, G. P.; Johnson, B. R.; Halas, N. J. *Nano Lett.* **2007**, *7*, 496–501.

(235) Dragan, A. I.; Geddes, C. D. *Phys. Chem. Chem. Phys.* **2011**, *13*, 3831–3838.

(236) Xie, F.; Centeno, A.; Ryan, M. R.; Riley, D. J.; Alford, N. *J. Mater. Chem. B* **2013**, *1*, 536–543.

(237) Sharma, M.; Pudasaini, R.; Ruiz-Zepeda, F.; Vinogradova, E.; Ayon, A. A. *ACS Appl. Mater. Interfaces* **2014**, *6*, 15472–15479.

(238) Wang, J. L.; Ando, R. A.; Camargo, P. H. C. *ACS Catal.* **2014**, *4*, 3815–3819.

(239) Wang, S.; Zhang, D.; Ma, Y.; Zhang, H.; Gao, J.; Nie, Y.; Sun, X. *Appl. Mater. Interfaces* **2014**, *6*, 12429–12435.

(240) Zhang, J.; Teo, J.; Chen, X.; Asakura, H.; Tanaka, T.; Teramura, K.; Yan, N. *ACS Catal.* **2014**, *4*, 1574–1583.

(241) Sloufova, I. S.; Vlckova, B.; Bastl, Z.; Hasslett, T. L. *Langmuir* **2004**, *20*, 3407–3415.

(242) Yang, Y.; Shi, J.; Kawamura, G.; Nogami, M. *Scr. Mater.* **2008**, *58*, 862–865.

(243) Govorov, A. O.; Carmeli, I. *Nano Lett.* **2007**, *7*, 620–625.

(244) Lubner, C. E.; Grimme, R.; Bryant, D. A.; Golbeck, J. H. *Biochemistry* **2010**, *49*, 404–414.

(245) Terasaki, N.; Yamamoto, N.; Hiraga, T.; Yamanoi, Y.; Yonezawa, T.; Nishihara, H.; Ohmori, T.; Sakai, M.; Fujii, M.; Tohri, A.; Iwai, M.; Inoue, Y.; Yoneyama, S.; Minakata, M.; Enami, I. *Angew. Chem. Int. Ed.* **2009**, *48*, 1585–1587.

(246) Brecht, M.; Studier, H.; Elli, A. F.; Jelezko, F.; Bittl, R. *Biochem.* **2007**, *46*, 799–806.

(247) Beyer, S. R.; Ullrich, S.; Kudera, S.; Gardiner, A. T.; Cogdell, R. J.; Koehler, J. *Nano Lett.* **2011**, *11*, 4897–4901.

(248) Viste, P.; Plain, J.; Jaffiol, R.; Vial, A; Adam, P. M.; Royer, P. *ACS Nano* **2010**, *4*, 759–764.

(249) Galarreta, B. C.; Harte, E.; Marquestaut, N.; Norton, P. R.; Lagugne-Labarthet, F. *Phys. Chem. Chem. Phys.* **2010**, *12*, 6810–6816.

(250) Thomas, M.; Greffet, J. J.; Carminati, R. *Appl. Phys. Lett.* **2004**, *85*, 3863–3865.

(251) Han, Y.; Lupitskyy, R.; Chou, T. M.; Stafford, C. M.; Du, H.; Sukhishvili, S. *Anal. Chem.* **2011**, *83*, 5873–5880.

(252) Bek, A.; Jansen, R.; Ringler, M.; Mayilo, S.; Klar, T. A.; Feldmann, J. *Nano Lett.* **2008**, *8*, 485–490.

(253) Kuzma, A.; Weis, M.; Flickyngerova, S.; Jakabovic, J.; Satka, A.; Dobrocka, E.; Chlpik, J.; Cirak, J.; Donoval, M.; Telek, P.; Uherek, F.; Donoval, D. *J. Appl. Phys.* **2012**, *112*, 1–5.

(254) Moore, W. M. *J. Phys. Chem.* **1988**, *92*, 4421–4426.

(255) Ray, K.; Badugu, R.; Lakowicz, J. R. *J. Am. Chem. Soc.* **2006**, *128*, 8998–8999.

(256) Krassen, H.; Schwarze, A.; Friedrich, B.; Ataka, K.; Lenz, O.; Heberle, J. *Acs Nano* **2009**, *3*, 4055–4061.

(257) Shibata, Y.; Yamagishi, A.; Kawamoto, S.; Noji, T.; Itoh, S. *J. Phys. Chem. B.* **2010**, *114*, 2954–2963.

(258) Fu, Y.; Lakowicz, J. R. *Laser Photon. Rev.* **2009**, *3*, 221–232.

(259) Bardhan, R.; Grady, N. K.; Cole, J. R.; Joshi, A.; Halas, N. J. *ACS Nano* **2009**, *3*, 744–752.

(260) Kulakovich, O.; Strekal, N.; Yaroshevich, A.; Maskevich, S.; Gaponenko, S.; Nabiev, I.; Woggon, U.; Artemyev, M. *Nano Lett.* **2002**, *2*, 1449–1452.

(261) Kneipp, K.; Kneipp, H.; Itzkan, I.; Dasari, R. R.; Feld, M. S. *J. Phys. Condens. Matter* **2002**, *14*, R597–R624.

(262) Ganguly, M.; Mondal, C.; Chowdhury, J.; Pal, J.; Pal, A.; Pal, T. *R. Soc. Chem.* **2014**, *43*, 1032–1047.

(263) Ganesh, N.; Zhang, W.; Mathias, P. C.; Chow, E.; Soares, J. A.n. T.; Malyarchuk, V.; Smith, A. D.; Chunningham, B. T. *Nat. Nanotechnol.* **2007**, *2*, 515–520.

(264) Jiang, Y.; Wang, H. Y.; Wang, H.; Gao, B. R.; Hao, Y. W.; Jin, Y.; Chen, Q. D.; Sun, H. B. *J. Phys. Chem. C* **2011**, *115*, 12636–12642.

(265) Li, X.; Kao, F. J.; Chung, C. C.; He, S. *Opt. Express* **2010**, *18*, 11335–11346.

(266) Zhang, J.; Fu, Y.; Chowdhury, M. H.; Lakowicz, J. R. *J. Phys. Chem. C* **2007**, *111*, 11784–11792.

(267) Lakowicz, J. R. *Anal. Biochem.* **2001**, *298*, 1–24.

(268) Wenger, J.; Aouani, H.; Gerard, D.; Blair, S.; Ebbesen, T. W.; Rigneault, H. *Proc. of SPIE* **2010**, *7577*, 75770J.

(269) Ashraf, I.; Skandary, S.; Khaywah, M. Y.; Metzger, M.; Meixner, A. J.; Adam, P. M.; Brecht, M. *Photonics* **2015**, *2*, 838–854.

(270) Foguel, D.; Chaloub, R. M.; Silva, J. L.; Crofts, A. R.; Weber, G. *Biophys. J.* **1992**, *63*, 1613–1622.

(271) Palsson, L. O.; Dekker, J. P.; Schlodder, E.; Monshouwer, R.; van Grondelle, R. *Photosyn. Res.* **1996**, *48*, 239–246.

(272) Schlodder, E.; Falkenberg, K.; Gergeleit, M.; Brettel, K. *Biochemistry* **1998**, *37*, 9466–9476.

(273) Nakamura, T.; Hayashi, S. *Jpn. J. Appl. Phys.* **2005**, *44*, 6833–6837.

(274) Pribik, R.; Aslan, K.; Zhang, Y.; Geddes, C. D. *J. Phys. Chem. C* **2008**, *112*, 17969–17973.

(275) Biswas, H. S.; Datta, J.; Chowdhury, D. P.; Reddy, A. V. R.; Ghosh, U. C.; Srivastava, A. K.; Ray, N. R. *Langmuir* **2010**, *26*, 17413–17418.

(276) Rusmini, F.; Zhong, Z.; Feijen, J. *Biomacromolecules* **2007**, *8*, 1175–1789.

(277) Zhong, M.; Fang, J.; Wei, Y. *Bioconjugate Chem.* **2010**, *21*, 1177–1182.

(278) MacDonald, C.; Morrow, R.; Weiss, A. S.; Bilek, M. M. *J. R. Soc. Interface* **2008**, *5*, 663–669.

(279) Tan, Y. H.; Pandey, B.; Sharma, A.; Bhattarai, J.; Stine, K. J. *Global J. Biochem* **2012**, *3*, 1–21.

(280) Montague, M.; Ducker, R. E.; Chong, K. S. L.; Manning, R. J.; Rutten, F. J. M.; Davies, M. C.; Leggett, G. J. *Langmuir* **2007**, *23*, 7328–7337.

(281) Mrksich, M.; Whitesides, G. M. *Annu. Rev. Biophys. Biomol. Struct.* **1996**, *25*, 55–78.

(282) Reynolds, N. P.; Janusz, S.; Escalante-Marun, M.; Timney, J.; Ducker, R. E.; Olsen, J. D.; Otto, C.; Subramaniam, V.; Leggett, G. J.; Hunter, C. N. *J. Am. Chem. Soc.* **2007**, *129*, 14625–14631.

(283) Tan, Y. H.; Lizu, M.; Nolting, B.; Go, J. G.; Gervay-Hague, J.; Liu G, Y. *ACS Nano* **2008**, *2*, 2376–2384.

(284) Ulman, A. *Chem. Rev.* **1996**, *96*, 1533–1554.

(285) Newton, L.; Slater, T.; Clark, N.; Vijayaraghavan, A. *J. Mater. Chem. C* **2013**, *1*, 376–393.

(286) Ciesielski, P. N.; Hijazi, F. M.; Scott, A. M.; Faulkner, C. J.; Beard, L.; Emmett, K.; Rosenthal, S. J.; Cliffel, D.; Jennings, G. K. *Bioresour. Technol.* **2010**, *101*, 3047–3053.

(287) Brettel, K. *Biochim. Biophys. Acta, Bioenerg.* **1997**, *1318*, 322–373.

(288) Carmeli, I.; Mangold, M.; Frolov, L.; Zebli, B.; Carmeli, C.; Richter, S. *Adv. Mater.* **2007**, *19*, 3901–3905.

(289) Kaniber, S. M.; Brandsteter, M.; Simmel, F. C.; Carmeli, I.; Holleitner, A. W. *J. Am. Chem. Soc.* **2010**, *132*, 2872–2873.

(290) Link, S.; El-Sayed, M. A. *Annu. Rev. Phys. Chem.* **2003**, *54*, 331–366.

(291) Ru, E. C. L.; Galloway, C.; Etchegoin, P. G. *Phys. Chem. Chem. Phys.* **2006**, *8*, 3083–3987.

(292) Xu, H.; Aizpurua, J.; Käll, M.; Apell, P. *Phys. Rev. E* **2000**, *62*, 4318–4324.

(293) Fulmes, J.; Jager, R.; Bräuer, A.; Schafer, A.; Jager, S.; Gollmer, D. A.; Horrer, A.; Nadler, E.; Chasse, T.; Zhang, D.; Meixner, A. J.; Kern, D. P.; Fleischer, M. *Nanoscale* **2015**, *7*, 14691–14696.

(294) Kowalska, D.; Krajnik, B.; Olejnik, M.; Twardowska, M.; Czechowski, N.; Hofmann, E.; Mackowski, S. *Scientific World J.* **2013**, *2013*, 1–12.

(295) Moskovits, M. *Nature* **2011**, *469*, 307–308.

(296) Konno, K.; Ito, E.; Noh, J.; Hara, M. *Jpn. J. Appl. Phys.* **2006**, *45*, 405–408.

(297) Love, J. C.; Estroff, L. A.; Kriebel, J. K.; Nuzzo, R. G.; White *Chem. Rev.* **2005**, *105*, 1103–1169.

(298) Nuzzo, R. G.; Fusco, F. A.; Allara, D. L. *J. Am. Chem. Soc.* **1987**, *109*, 2358–2368.

(299) Brewer, N. J.; Rawsteme, R. E.; Kothari, S.; Leggett, G. J. *J. Am. Chem. Soc.* **2001**, *123*, 4089–4090.

(300) Leggett, G. J. *Chem. Soc. Rev.* **2006**, *35*, 1150–1161.

(301) Tarlov, M. J.; Burgess, D. R. F.; Gillen, G. *J. Am. Chem. Soc.* **1993**, *115*, 5305–5306.

(302) Huang, J.; Hemmiinger, J. C. *J. Am. Chem. Soc.* **1993**, *115*, 3342–3343.

(303) Norrod, K. L.; Rowlen, K. L. *J. Am. Chem. Soc.* **1998**, *120*, 2656–2657.

(304) Zhang, Y.; Terrill, R. H.; Bohn, P. W. *Chem. Mater.* **1999**, *11*, 2191–2198.

(305) Herrwerth, S.; Rosendahl, T.; Feng, C.; Fick, J.; Eck, W.; Dahint, H. R.; Grunze, M. *Langmuir* **2003**, *19*, 1880–1887.

(306) Lahiri, J.; Isaacs, L.; Tien, J.; Whitesides, G. M. *Anal. Chem.* **1999**, *71*, 777–790.

(307) Patel, N.; Davies, M. C.; Hartshorne, M.; Heaton, R. J.; Roberts, C. J.; Tendler, S. J. B.; Williams, P. M. *Langmuir* **1997**, *13*, 6485–6490.

(308) Marun, M. E. Nanofabrication of Bioninspired Architectures with Light Harvesting Proteins., Ph.D. Thesis, University of Twente, Netherlands., 2009.

(309) *Surface Design: Applications in Bioscience and Nanotechnology*; Foerch, R., Schoenherr, H., Jenkins, T. A., Eds.; John Wiley and Sons: 2009.

(310) Niu, H.; Wang, S.; Zhou, Z.; Ma, Y.; Ma, X.; Cai, Y. *Anal. Chem.* **2014**, *86*, 4170–4177.

(311) Wang, Q.; Wang, J.-. F.; Geil, P. H.; Padua, G. W. *Biomacromolecules* **2004**, *5*, 1356–1361.

(312) Gillen, G.; Bennett, J.; Tarlov, M. J.; Burgess, D. R. F. *Anal. Chem.* **1994**, *66*, 2170–2174.

(313) Adams, J.; Tizazu, G.; Janusz, S.; Brueck, S. R. J.; Lopez, G. P.; Leggett, G. J. *Langmuir* **2010**, *26*, 13600–13606.

(314) Gouzman, I.; Dubey, M.; Carolus, M. D.; Schwartz, J.; Bernasek, S. L. *Surf. Sci.* **2006**, *600*, 773–781.

(315) Gu, J.; Yam, C. M.; Li, S.; Cai, C. *J. Am. Chem. Soc.* **2004**, *126*, 8098–8099.

(316) Ducker, R. E.; Jansusz, S.; Sun, S.; Leggett, G. J. *J. Am. Chem. Soc.* **2007**, *129*, 14842–14843.

(317) Frasconi, M.; Mazzei, F.; Ferri, T. *Anal. Bioanal. Chem.* **2010**, *398*, 1545–1564.

(318) Mrksich, M. *MRS Bulletin* **2005**, *30*, 180–184.

(319) Rechendorff, K. The Influence of Surface Roughness on Protein Adsorption., Ph.D. Thesis, University of Aarhus, Denmark., 2006.

(320) Williams, D. F.; Askill, I. N.; Smith, R. *J. Biomed. Mater. Res.* **1985**, *19*, 313–320.

(321) Harder, P.; Grunze, M.; Dahint, R. *J. Phys. Chem. B* **1998**, *102*, 426–436.

(322) Mrksich, M.; Sigal, G. B.; Whitesides, G. M. *Langmuir* **1995**, *11*, 4383–4385.

(323) Ostuni, E.; Chapman, R. G.; Holmlin, R. E.; Takayama, S.; Whitesi *Langmuir* **2001**, *17*, 5605–5620.

(324) Wang, R. L. C.; Kreuzer, H. J. *J. Phys. Chem. B* **1997**, *101*, 9767–9773.

(325) Nakanishi, K.; Sakiyama, T.; Kumada, Y.; Imamura, K.; Imanaka, H. *Curr. Proteonomics* **2008**, *5*, 161–175.

(326) Wang, J.; Shan, J.; Xu, Q.; Ruan, X.; Gong, Y.; Kuang, T.; Zhao, N. *J. Photochem. Photobiol. B. Biol.* **1999**, *50*, 189–196.